Analysis of Angle of Attack for Efficient Slope Ascent by Rovers

Hiroaki Inotsume

CMU-RI-TR-15-22

Submitted in partial fulfillment of the requirements for the degree of Masters of Science in Robotics

The Robotics Institute
Carnegie Mellon University
Pittsburgh, PA 15213

August 2015

Thesis Committee:
David Wettergreen, Chair
William ”Red” Whittaker
Dimitorios Apostolopoulos
Christopher Cunningham

Abstract

What direction should a rover drive to efficiently ascend slope of loose soil? To explore the lunar poles, rovers will need to traverse craters where high slip will hamper progress. Because of limited energy, rovers need to find efficient routes to traverse such sloped terrain. It is an open question whether efficient and successful slope-ascending is achieved in loose soil by driving directly uphill or in a diagonal cross-slope direction.

In this thesis, the influence of the rover's angle of attack on slope-ascent performance was analyzed based on a slope-ascent rover model that consists of force equilibrium conditions and terramechanics-based wheel–soil interaction. The terramechanic model was validated in single-wheel experiments. Rover slip, uphill velocity, and power efficiency were predicted and associated with the angle of attack. Analysis shows the ascent in the direct uphill direction results in most effective motion, in terms of velocity and power efficiency, on most of the slopes analyzed even if the vehicle longitudinal slip can be reduced by decreasing the angle of attack. The analysis also indicates that a rover can diagonally ascend steep slopes where it can not drive directly up if the rover can generate sufficient lateral grip against downhill slides.

Slope-ascent experiments using a rover were conducted to experimentally evaluate the effect of the angle of attack. The test results validated the model-based analysis and the usefulness of the proposed slope-ascent model.

A strategy to select slope-ascending routes is proposed based on the model and experiment based analysis. The utility of the route selection method was demonstrated in simulations on various slopes and for different rovers.

The findings in this research are useful to develop path planning strategies and also to develop locomotion configuration and controls which can have high slope-ascent capability.

Acknowledgments

First of all, I would like to thank my adviser, David Wettergreen, for his continuous support and guideline for the development of this research and throughout my student life in the Robotics Institute. He introduced me a lot of interesting research topics, provided me advice from multiple points of view, and always tried to keep my motivation high.

I would also like to thank Red Whittaker for providing me a chance to tackle the research topic in this thesis. The discussions with him and his advice greatly pushed the progress of this research. In addition, I would like to thank Dimi Apostolopoulos and Chris Cunningham for having discussions that provided me various possibilities of research directions.

I thank the members of the Wheel Testbed Project: Chuck Whittaker, Jim Teza, David Kohanbash, Joe Amato, and Molly Whittaker. With their hard work and help, I could conduct various experiments and also could have time for this research.

The discussions with Scott Moreland, Chris Skonieczny, Colin Creager, Kyle Johnson, Matt Heverly, and Patrick Degrosse helped me a lot to develop deeper understanding of terramechanics and important rover mobility issues. Also the testing of Scarab rover could not be done without Colin's great help.

Lastly I appreciate the Funai Foundation for Information Technology for their financial support that realized my study at CMU.

Contents

List of Figures

List of Tables

Chapter 1

Introduction

There exists a lot of research to navigate ground vehicles. A typical navigation problem is on flat or benign terrains where vehicle slippage is negligible or there exist routes that can just avoid high slopes and high slip situations. Most of navigation algorithms and systems are sufficiently robust and can work in most of situations including both indoor and outdoor scenarios, and they were indeed demonstrated their effectiveness in target fields.

However, sometimes we want to make robots explore challenging terrains, steep slopes of sand dunes, crests of mountains, or rims and interiors of craters where no gentle route exists and where robots need to take some risks of mobility hazard, or immobilization. Still, however, we want to find better and safer routes and make the robots overcome the challenging terrains.

This thesis addresses the problem of what routes a rover should select to safely and efficiently ascend slopes of slippery, deformable materials as illustrated in Figure1.1. This thesis answers the question whether a rover that cannot drive directly up a slope can overcome the slope diagonally, and answer the question in what direction the rover can ascend most efficiently.

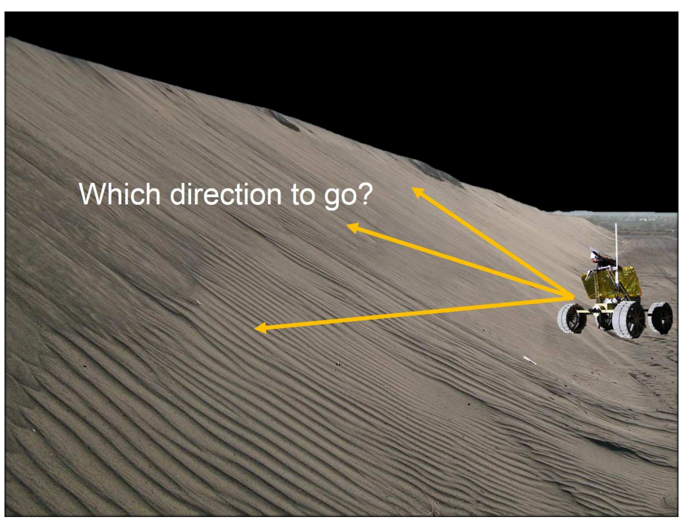

Figure 1.1: Research problem.

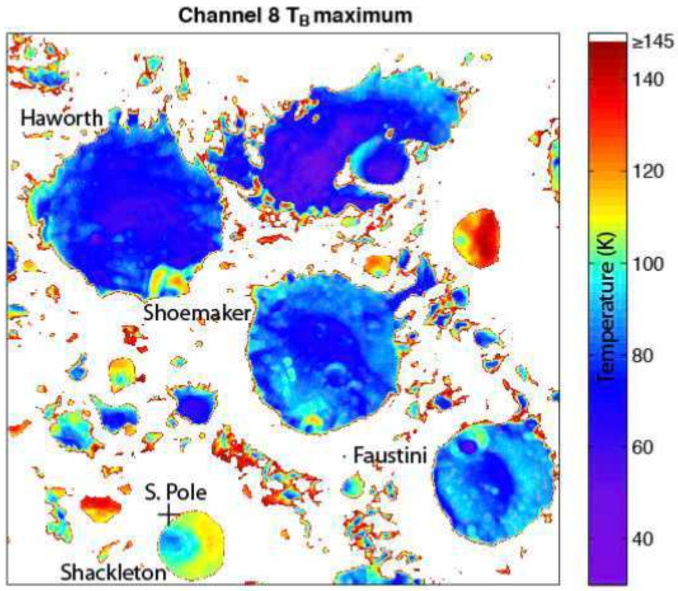

Figure 1.2: Temperature map of the craters around the lunar south pole showing the maximum temperature throughout a year [2]. Many of the maximum temperature inside the permanently shadowed craters are less than 100 K.

1.1 Motivation

Recent orbital surveys have shown the possibility of the presence of water inside permanently shadowed craters of the south pole of the Moon. Figure 1.2 shows the maximum temperature of the craters around the lunar south pole observed by NASA's Lunar Reconnaissance Orbiter [1]. The maximum temperature of most of the regions inside these craters are less than 100 K ($\approx$ -173^{o}C $\approx$ -280^{o}F). Because of the low temperature, it is possible that water, hydrogen, oxygen and other volatiles are entrapped in the subsurface of the craters, and the regions around them. These materials are essential to develop bases on/under the lunar surface for the future manned space missions and also to obtain scientific knowledge of the Moon or our universe. However, since the capabilities of orbital surveys are limited, the existence of water and the actual amount/distribution of that, if any, are still open questions. Therefore, *in situ* measurements of these areas have been demanded and planned using robotic vehicles, or rovers [3, 4].

Figure 1.3 shows Shackleton crater, one of the permanently shadowed craters on the lunar south pole, and the distribution of slopes around it. The diameter of the crater is approximately 21 km and the depth is around 4.2 km. Slopes of the inner walls varies from 20^o to 35^o, 30.5^o on average, approaching the angle of repose [5]. In addition, the crater is surrounded by many small craters which consists of slopes of 10^o–25^o. Since it is uncertain where the water ices are varied, rovers will be required to traverse a wide range of area, ascending, descending, and/or crossing slopes.

One of the biggest problems with traversing these crater walls is slippage. Because the surfaces of the Moon is covered with fine-grained sand, called regolith, wheels of rovers can easily slip in both their longitudinal and lateral directions due to the lack of traction, especially on slopes. Longitudinal slippage hampers the smooth travel of rovers and increases their energy

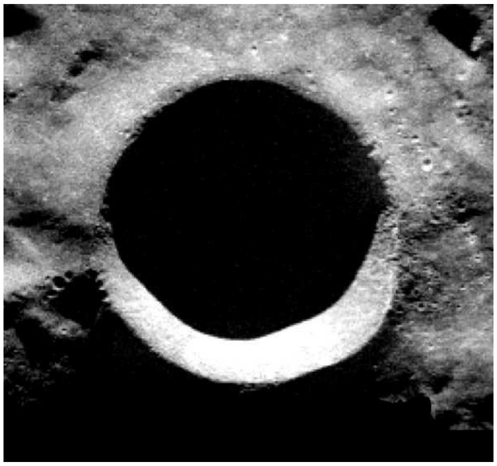

(a) Shackleton crater (Image courtesy of NASA)

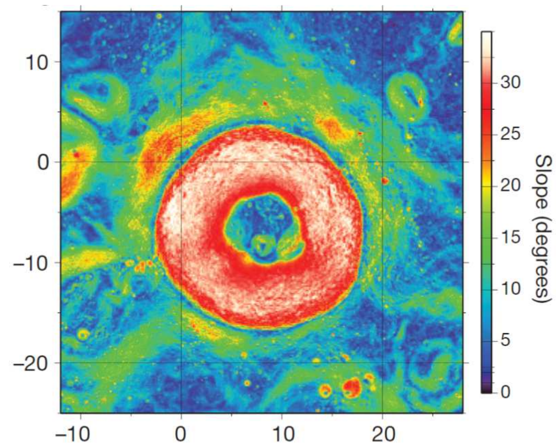

(b) Slope distribution of Shackleton crater [5]

Figure 1.3: Shackleton crater and slopes around it.

consumption. In addition, their wheels dig into the soil in association with the slip, and when the slip becomes significant, the rovers can become immobilized in the soil. On the other hand, lateral slippage makes the rovers deviate from planned paths and makes the localization and path tracking of the rovers difficult. In the worst cases, the rovers are unable to reach the target areas or may collide with hazardous rocks.

In addition to the mobility issue, there exist problems related to rover energy and temperature in the exploration of the lunar pole regions. Because of the high latitude, the areas sunlit are limited and change overtime. The duration of the continuous sunlight in the most of scientifically interesting regions in the pole last only several days. Therefore rovers, which are typically powered from solar arrays, are required to rapidly move forward to feed themselves energy and to avoid cold night, which will be tough for electronics, as much as possible while searching for the hidden resources [6, 7, 8].

Because of these reasons, exploration around the pole craters are extremely challenging, and it is essential to select routes which can maximize the possibility of a successful traverse on target slopes. That is, finding a route which achieves lower slip and higher efficiency is required.

1.2 Related work

1.2.1 Motion planning and control on slopes

There are some works on motion planning and control of rovers for traversing slopes that are covered with deformable materials and induce non-negligible slippage. For example, Helmick et al. developed a navigation system based on a mobility map which takes into account rover slip [9]. They predicted the slip from terrain appearance and previous experience on similar terrain. Their system finds a route that avoids hazardous obstacles and highly slippery terrains. Then it follows the path by minimizing slip using the slip-compensated path follower that works based on visual odometry and vehicle kinematics [10]. Karumanchi et al. developed a path planning system where a mobility map of sloped terrain is constructed from past experience of vehicle slip, and it was utilized for planning of vehicle paths and velocities on slopes [11]. Their mobility map is represented by the maximum feasible velocities for different headings on the target terrain.

As a path-following control, Ishigami et al. proposed a model-predictive feed-forward control [12]. They analyzed the mobility of a rover based on wheel–soil interaction and utilized the model to provide steering motions of the rover for traversing side-slopes. Kren et al. developed a model-predictive traction and steering control system, which is based on wheel–soil interaction modeling, and tested it on an inclined terrain of loose soil [13]. The test results showed the model-predictive control achieved a better path-following ability than a feedback-based approach.

Daniel et al. on the other hand, developed a slip control system for a rover that is equipped with a plow [14]. They showed that the vehicle slip can be controlled and regulated by adjusting the depth of the plow into the soil while the rover descends steep slopes.

1.2.2 Rover slope testing

It has been believed by many researchers that diagonally driving up a slope is better than directly ascending up the same slope to reduce wheel slippage. However, this is still an open question.

It was reported that on Mars, during the Mars Exploration Rover (MER) Opportunity tried to egress from craters, the rover experienced high slippage when it went directly up slope, reaching 100% slip. The rover could get out of the craters by cross-slope driving with the heading approximately 45^o off from the directly uphill direction [15, 16], as shown in Figure 1.4.

Some mobility test results of rovers on a tilt table of soft soil were reported in [17, 18]. They measured slip and slide of the rover at 90^o, 45^o, and 0^o angle of attack for slope ascent, descent, and cross-slope scenarios. The results indicate that the longitudinal slip reduces when the diagonal slope-ascent is made compared to the direct slope ascent. However, this does not necessarily indicate that the diagonal slope-ascent is always better than the direct slope ascent since the vehicle downhill slide increases at shallower angles of attack and the actual travel velocity in the uphill direction, which is important for slope-ascent, is determined from the both longitudinal and lateral slip.

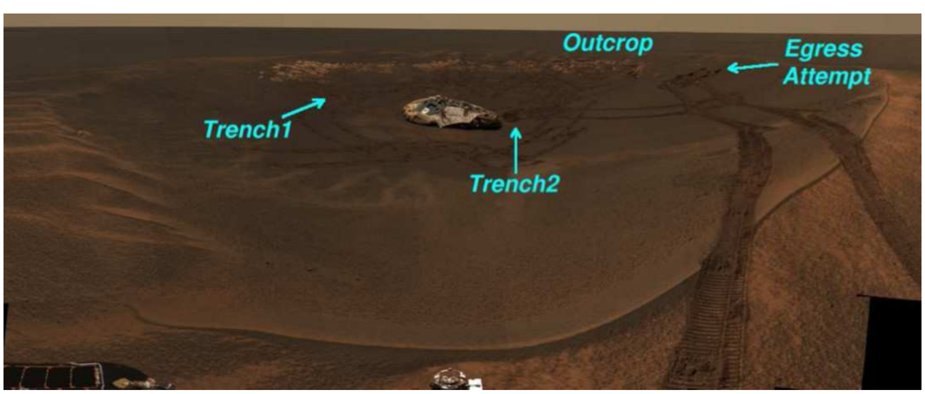

Figure 1.4: Tracks of Opportunity rover in the Eagle crater [15].

(a) (b)

Figure 1.5: Scarab rover with active suspension. (a) The overview of the rover. (b) Scarab diagonally ascending a slope with leaned posture.

Another experiment showed that diagonal uphill driving can improve slope-ascent performance when a rover posture is controlled. Scarab shown in Figure 1.5 is a rover which has such capability. The rover has actively actuated rocker arms that control the wheelbases of the left and right side wheels and thus the rover roll angle. It was experimentally showed that Scarab was able to climb up steep slopes of loose media with significantly less slippage when the ascent was made at shallow angle of attack ($\approx 25^o$) and by adjusting the rover configuration, compared with when the rover climbed directly up the slopes toward the maximum inclination angle without active posture control [19]. In addition to this, the vehicle longitudinal slip and power consumption were measured during ascending slopes for the leaned configuration at various angles of attack. The test results showed an angle of attack of 15-25^o achieved low slip and power consumption when the active posture control was engaged.

It has not been well known, however, whether rovers without active posturing capability can improve slope-ascent performance with shallower angles of attack, and how the angle of attack affects the performance. No detailed analysis of the effect of the angle of attack has been made for general rovers with nominal configurations, without active posture controls. Also, in the previous testing mentioned above, the slip only in the vehicle longitudinal direction was reported and the actual uphill progress has not been evaluated explicitly.

1.2.3 Modeling and analysis of rover mobility on loose soil

While field experiments using real rovers provide rich information to understand their performance, they are time consuming and cost a lot. Another solution to understand and evaluate rover performance on loose soil is modeling the vehicle/wheel–soil interactions and wheel slip, and analyzing the performance based on the models.

There are various ways to model wheel slip. One way is modeling slip by regressions in either parametric or non-parametric manner. Polynomial curve fitting is one of the simplest methods to model slip with approximation functions of terrain geometry, such as the pith and roll angle of the terrain. For example, the vehicle slip of the Mars rover Curiosity were studied by field trials on Earth and its slip was characterized by polynomial functions which are dependent on the terrain surface material [20]. Similarly in [21], the rover slip is modeled as functions of the terrain inclination, and are incorporated into their trajectory generator to compensate wheel slip while climbing or crossing hills. These parametric regression approaches require to carefully select functions, e.g., polynomial or exponential functions, to approximate the slip. The slip behaviors are highly nonlinear due to the complicated wheel–soil interactions, especially at steep slopes, and choosing inappropriate functions results in significant prediction errors.

Another regression approach to model vehicle/wheel slip is a non-parametric learning method. Unlike the parametric regressions, non-parametric methods require no explicit assumptions in the model shape, and they can possibly provide better accuracy than parametric methods. However the computational cost of non-parametric approaches for training and prediction are typically more expensive than parametric ones, and the cost grows as the training data increases. In addition, the model accuracy depends on the utilized learning algorithms. Examples of non-parametric regressions include Neural Networks, k-Nearest Neighbor, Support Vector regression, and Gaussian Process regressions, and some of them were implemented on robotic vehicles to model the relationship between vehicle slip and terrain geometry [11, 22, 23].

One of the benefits of regression approaches is that they do not require to understand details of underlying physical phenomenon or to obtain unknown vehicle–soil interaction parameters. However, one drawback of these approaches is that predictions in the domain with sparse or no training data tend to result in significantly large errors or unrealistic behaviors. Wheel slip can be modeled in more sophisticated fashion by taking into account the underlying physical effects of the wheel–soil interaction. For example Cameron et al. developed a rover dynamic model that incorporates the wheel–soil interaction forces as simple mass-dumper systems and predicted the vehicle slip on slopes of soft soil and bedrocks [18]. Their model was capable of predicting rover behaviors on shallow slopes; however the prediction on steep slopes was less accurate.

Terramechanics is another dynamic modeling approach that relates wheel slip and interaction forces based on soil mechanics and vehicle dynamics. Terramechanic theory was originally developed and organized by Bekker [24] and Wong [25] during 1950s–1960s mainly for large and heavy off-road vehicles, such as vehicles for military, agricultural, mining and construction purposes. It models the interactions between soils and wheels/tracks/tools via semi-empirical formulations of soil bearing and shearing capacities. While Terramechanic theory requires a number of soil-specific parameters in its computation, because of its computational efficiency and good prediction capability, Terramecahnics has been applied to the analysis of planetary rovers in recent years for design, planning and control purposes [26, 27, 28, 29, 30]. For instance, Apostolopoulos used Terramechanic theory to analyze the locomotion configuration of rovers for various types of soils and terrains, including slopes [26]. Based on the Terramechanics-based vehicle model, he developed formulas to design vehicle configurations for various operation scenarios. Iagnnema developed a motion control algorithm based on Terramechanics for rough terrain traverse [27], and he also proposed an online soil parameter identification method that can be used for predicting mobility of a rover from experience. Ishigami et al., on the other hand, extended conventional Terramechanics, which had been basically restricted to the longitudinal motion analysis, and developed a comprehensive lateral force model to analyze steering maneuvers [28]. The model was further applied to a steering motion control for lateral traversing of slopes [12], and to a path planning strategy which takes into account wheel slippage [31].

While there exists research on model-based characterization and analysis of rover performance on slippery terrain, however, none of those research in literature, to the best of my knowledge, has explicitly analyzed performance of rovers in cross-slope ascent scenarios in details.

1.3 Objective and approach

The objective of this research is to find a route to increase the efficiency and possibility of successfull slope-ascent for a rover, given its configuration, terrain geometry, and soil properties. To this end, the influence of the angle of attack on slope-ascent performance of rovers is analyzed, and a strategy to select the angle of attack is proposed. Here the term angle of attack to a slope is defined as an angle of the heading of a rover with respect to the transverse direction of the slope. Angle of attack is 90^o when a rover is oriented to the uphill direction, and 0^o when in the lateral direction of the slope.

The scope of this research is linear trajectory motions to ascend slopes of deformable, slip-inducing soil. The research does not involve any steering maneuvers or curvilinear trajectories. In addition, while the slope-ascent performance can be greatly improved with active posture controls as shown in [19], this research focuses on conventional rovers that do not have such capability. However, the basic ideas of this research can be applicable to those outside of the scope.

The analysis is made by a slope-ascent model of a rover which consists of force equilibrium conditions on slope and a terramechanics-based wheel–soil interaction. The terramechanic model is validated through a single-wheel experiments. From the proposed model, rover slip is predicted, and rover trajectories for various angles of attack are analyzed. Furthermore, the influence of the angle of attack is evaluated also based on the power efficiency of the uphill motion. Slope-ascent experiments are carried out using the four-wheeled rover Scarab to experimentally evaluate the influence of the angle of attack and also to assess the validity of the model-based analysis.

Moreover, a strategy for selecting an efficient and successful slope-ascent route is proposed based on the model-based analysis. The usefulness of the proposed strategy is demonstrated through a series of slope-ascent simulations.

1.4 Overview

This thesis is organized as follows. In Chapter 2, the slope-ascent capability of a rover and influence of the angle of attack are analyzed based on a slope-ascent model. The slope-ascent experimentation using an actual rover and its result are described in Chapter 3. The validation of the model-based analysis of the slope-ascent performance is also discussed in this chapter. Then a route selection strategy to ascend slippery slopes is introduced and evaluated in Chapter 4. Finally, Chapter 5 concludes this thesis summarizing the results and contributions of this research. Several possible directions of future research are also provided in this chapter.

Chapter 2

Model-Based Analysis of Slope-Ascent Performance

In this chapter, slope-ascent performance of a rover with various angles of attack is analyzed based on an analytical quasi-static slope-ascent model and a terramechanics-based wheel–soil interaction model. To simplify the problem and to reduce the computational complexity, a rover motion is represented by a single-wheel under several assumptions.

First assumption is that the orientation of the rover/wheel are fixed and the rover/wheel moves linearly. This assumption is valid if the rover is commanded a linear motion, and the orientation error is kept minimal. To evaluate the effect of the angle of attack, simple linear trajectories suffice to be considered. More justification for the linear motion assumption comes from the fact that on sloped terrain, curvature motions which involves drastic steering maneuvers are not preferable since they tend to induce a significant level of downhill skid. In terms of the orientation error, on sloped terrain, the larger portion of rover weight is distributed on wheels on the downhill side, and therefore the traction forces generated on the downhill wheels differ from those on the uphill wheels. This force unbalance can cause some level of rotational moment around the center of gravity (CG) of the rover, resulting in possible orientation changes. This research assumes that the orientation change is negligibly small or can be reduced by an appropriate orientation control.

Second, the rover/wheel is assumed to be ascending a slope of a smooth surface and homogeneous soil condition at a quasi-static, steady state. While actual terrains are bumpy with local variations of inclinations, the smooth surface representation can be considered as an approximation of terrains by a combination of bets-fitted planes to the local terrains.

Under these simplifications and assumptions, the influence of the angle of attack is analyzed in the following sections. The validity and limitation of the single-wheel model is discussed in Appendix A. The slope-ascent wheel model is introduced in Section 2.1 in which the conditions of forces for a steady state traverse is described. The relationship between wheel slip and wheel–soil interaction forces is then briefly described in Section 2.2. Some parameters in the wheel force model are tuned based on single-wheel experiments. In Section 2.3, the behavior of the rover/wheel at various angles of attack on various angles of slope is analyzed and evaluated based on wheel slip and the efficiency of the motion which are predicted based on the proposed slope-ascent model.

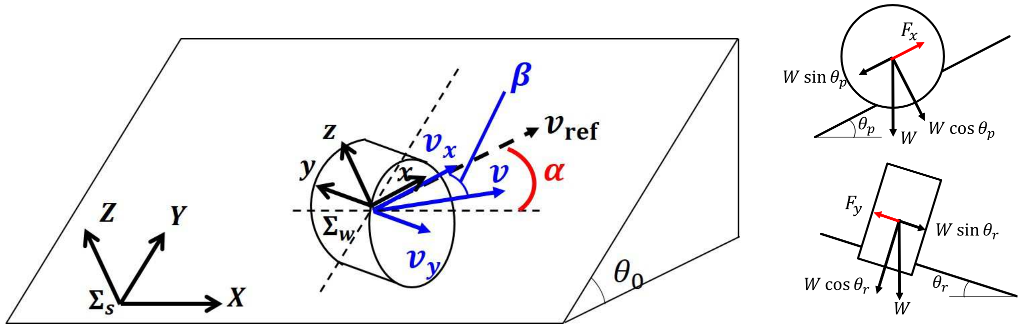

Figure 2.1: Slope ascent with an angle of attack. The wheel is ascending a slope of an angle θ_0 with an angle of attack α. The wheel needs to generate the longitudinal and lateral forces against the gravity resistance of the pitch and roll directions to keep a steady state ascent.

2.1 Slope-ascent model

Here assume that a wheel is driving uphill a slope of inclination angle θ_0 with an angle of attack α as shown in Figure 2.1. The angle of attack α is defined as the angle between the direction of the rover heading and the transverse direction of the slope: α is $\alpha = 90^o$ when the rover directly climbs up the slope in the maximum inclination direction, and $\alpha = 0^o$ when the rover heads the cross-slope direction.

Let us define the coordinate system on the slope surface Σ_s such that $Y^{(s)}$ denotes the uphill direction, $Z^{(s)}$ denotes the vertically upward direction against the slope surface, and $X^{(s)}$ denotes the transverse direction of the slope which makes a right-hand coordinate system. The wheel is heading at an angle of α from the $X^{(s)}$ direction of the slope as mentioned above. The wheel coordinate system, Σ_w, is thus obtained through a rotation of Σ_s about the $Z^{(s)}$ axis with α in the uphill direction.

The wheel is driven with a reference velocity v_{ref} in the $x^{(w)}$ direction and experiences the slip in the longitudinal and lateral directions resulting in the actual velocity v.

Assuming that the all the forces acting on the wheel in the $x^{(w)}$, $y^{(w)}$, and $z^{(w)}$ directions – drawbar pull F_x, lateral force F_y, and vertical force F_z, respectively–are in equilibrium with the gravitational force, and the wheel is in a steady state, then the following relationships hold:

$$F_x = W \sin\theta_p \tag{2.1}$$

$$F_y = W \sin\theta_r \tag{2.2}$$

$$F_z = W \cos\theta_0 \tag{2.3}$$

where W is the weight on the wheel, and θ_p and θ_r are the pitch and roll angles about the $y^{(w)}$ and $x^{(w)}$ axes of the wheel, respectively.

The pitch θ_p and roll θ_r of the wheel are determined geometrically from the slope angle θ_0 and the angle of attack α of the wheel as

$$\sin\theta_p = \sin\theta_0 \sin\alpha \tag{2.4}$$

$$\sin\theta_r = \sin\theta_0 \cos\alpha \tag{2.5}$$

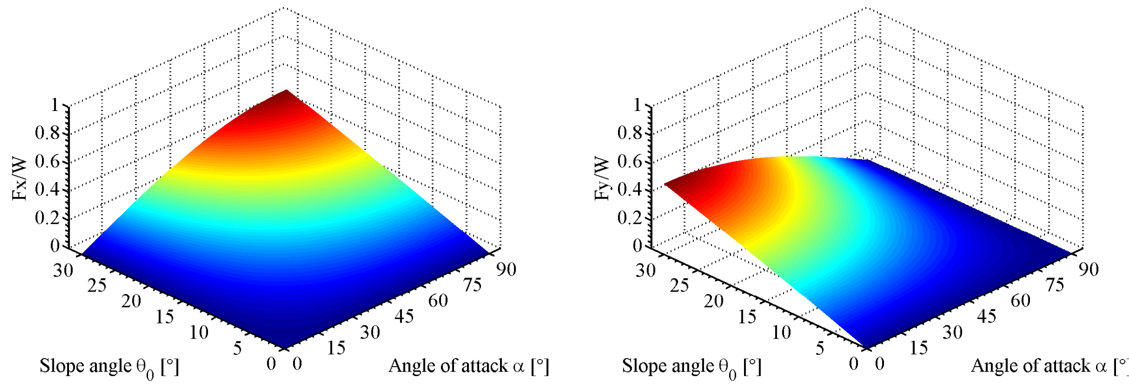

(a) Required drawbar pull F_x

(b) Required lateral force F_y

Figure 2.2: Drawbar pull and lateral force required to ascend slopes with various angles of attack. The forces were normalized to the rover weight W.

Figure 2.2 shows how much forces are required to keep a steady state slope-ascent against the gravitational resistance. As seen in the Figure 2.2 (a), the required drawbar pull F_x increases along with the increase of the angle of attack, and it becomes the maximum at $\alpha = 90°$ for each slope. On the other hand, the lateral force F_y, which is needed to grip the wheel against the sideslip, becomes the highest at $\alpha = 0°$ and it decreases as the angle of attack increases. The wheel is required to obtain the corresponding forces to ascend a slope at an angle of attack.

2.2 Terramechanics-based wheel–soil interaction model

The abovementioned forces, drawbar pull F_x, lateral force F_y, and vertical force F_z, are generated from the interactions between wheels and the soil. Here, the interaction forces are modeled based on terramechanics developed by Wong and Reece [32].

2.2.1 Model description

Let us assume that a rigid wheel traversing loose soil experiences slip in the longitudinal and lateral directions, resulting in the longitudinal velocity v_x, lateral slip velocity v_y, and the traveling velocity v, as shown in Figure 2.3. The longitudinal slippage is measured by the slip ratio of the wheel, s, which is defined as a proportion of the desired and actual longitudinal traveling velocities as [25]

$$s = \begin{cases} 1 - \frac{v_x}{v_{ref}} & (\text{if} \quad v_x \leq v_{ref}, \quad \text{driving}) \\ \frac{v_{ref}}{v_x} - 1 & (\text{if} \quad v_x > v_{ref}, \quad \text{breaking}) \end{cases} \tag{2.6}$$

where v_{ref} is the desired reference velocities and it equals to the wheel tangential velocity $v_{ref} = r\omega$ where r and ω denote the radius and angular velocity of the wheel, respectively. The range of the slip ratio value is $-1 \leq s \leq 1$; the slip ratio is positive when the longitudinal velocity is

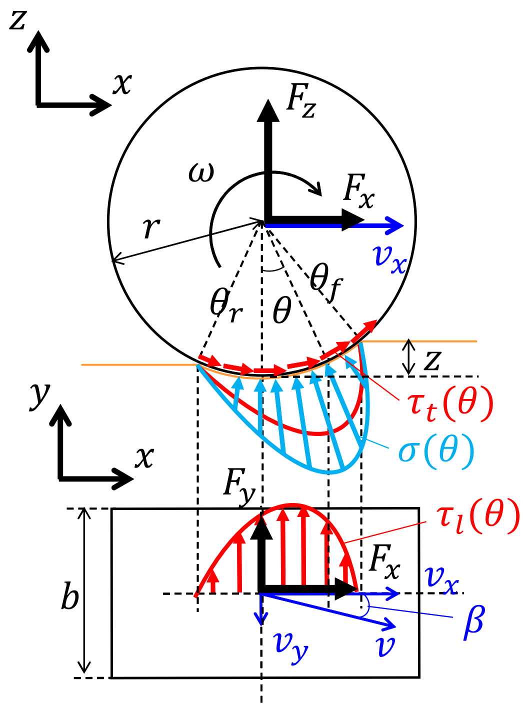

Figure 2.3: Wheel–soil interaction model. In deformable soil, stresses act on the contact patch in the normal, tangential, and lateral directions.

smaller than the reference velocity, and it becomes negative when the rover/wheel travels faster than the reference velocity.

On the other hand, the lateral slippage is expressed using the slip angle, β. The slip angle is defined as the angle between the heading velocity, v_x, and the wheel traveling velocity, v:

$$\beta = \tan^{-1}\left(\frac{v_y}{v_x}\right) \tag{2.7}$$

Under these conditions the normal stress, σ, and tangential and lateral shear stresses, τ_t and τ_l, are distributed on the cylindrical surface of the wheel, as shown in Figure 2.3. The magnitude of these stresses are dependent on the angular location on the wheel surface, θ. θ_f and θ_r depicted in Figure 2.3 denote the entry and exit angles of the wheel in the soil, respectively.

The resultant x, y, and z directional component of forces can be derived by integrating the stresses along the wheel circumference as follows [28, 32]:

$$F_x = rb\int_{\theta_r}^{\theta_f}\{\tau_t(\theta)\cos\theta - \sigma(\theta)\sin\theta\}d\theta \tag{2.8}$$

$$F_y = rb\int_{\theta_r}^{\theta_f}\tau_l(\theta)d\theta, \tag{2.9}$$

$$F_z = rb\int_{\theta_r}^{\theta_f}\{\tau_t(\theta)\sin\theta + \sigma(\theta)\cos\theta\}d\theta \tag{2.10}$$

where r denotes the wheel radius, and b denotes the wheel width. Note that the drawbar pull in this research means the net traction force which the wheel can obtain from the soil. That is, the drawbar pull F_x equals to the longitudinal thrust force H, which is developed by the shear stress τ_t, subtracted by the motion resistance R, which is resulted by the normal stress σ against the soil compaction and bulldozing. Therefore Eq. (2.8) can be rewritten as follows:

$$F_x = H - R \tag{2.11}$$

$$H = rb \int_{\theta_r}^{\theta_f} \tau_t(\theta) \cos\theta d\theta \tag{2.12}$$

$$R = rb \int_{\theta_r}^{\theta_f} \sigma(\theta) \cos\theta d\theta \tag{2.13}$$

$$\tag{2.14}$$

In addition to the forces, the torque necessary to drive the wheel, T_R, is given as follows:

$$T_R = r^2 b \int_{\theta_r}^{\theta_f} \tau_t(\theta) d\theta \tag{2.15}$$

These forces and torque are determined by the distributions of the normal and shear stresses.

Normal stress distribution

The normal stress distribution $\sigma(\theta)$ can be modeled based on the relationship between the pressure that acts on the wheel from the soil and the wheel sinkage. The basic pressure–sinkage relationship developed by Terzaghi is provided as follows [33]:

$$p = kz^n \tag{2.16}$$

where p denotes the pressure that acts on an object penetrated in soils, and z denotes the penetration depth. k and n, called pressure–sinkage modulus and sinkage exponent, respectively, are constant parameters which represent the bearing capability of the soil. As shown in Figure 2.4, the pressure exponentially increases as the depth increases and its shape is determined by the parameter n. The pressure–sinkage modulus k determines the magnitude of the pressure.

Terzaghi's pressure–sinkage relationship was improved later by Reece to take into account the effect of the dimension of the penetrated object as follows [34]:

$$p = k_\sigma \left(\frac{r}{b_w} \right)^n \tag{2.17}$$

$$k_\sigma = ck_c + \rho g b_w k_\phi \tag{2.18}$$

where b_w represents the smaller of the two dimensions of the contact patch for rectangular objects, or the radius for circular objects. c denotes the soil cohesion; k_c and k_ϕ denote the pressure–sinkage moduli; ρ denotes the soil bulk density; and g denotes gravitational acceleration.

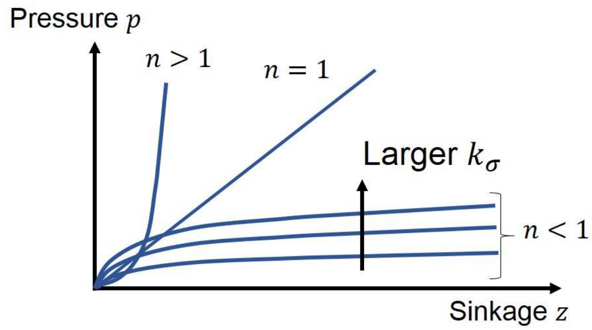

Figure 2.4: Typical pressure–sinkage curves. The basic shape of the curves is determined by the sinkage exponent parameter n while the magnitude is dependent on the pressure–sinkage modulus k_σ.

The normal stress distribution beneath a wheel can be obtained by applying the Reece's pressure–sinkage relationship to the cylindrical contact surface. Here the sinkage z at the angle θ of the wheel can be geometrically calculated as

$$z(\theta) = r(\cos\theta - \cos\theta_f) \tag{2.19}$$

By substituting Eq. (2.19) into Eq. (2.17) and making some modification, the following normal stress distribution model can be derived [32]:

$$\sigma(\theta) = k_\sigma \left(\frac{r}{b_w}\right)^n (\cos\theta^* - \cos\theta_f)^n \tag{2.20}$$

$$\theta^* = \begin{cases} \theta & (\theta_m \le \theta \le \theta_f) \\ \theta_f - \frac{(\theta-\theta_r)(\theta_f-\theta_m)}{\theta_m-\theta_r} & (\theta_r \le \theta < \theta_m) \end{cases} \tag{2.21}$$

where θ_m is the wheel angle at which the normal stress becomes the maximum. It is experimentally known that this maximum stress angle shifts forward when the longitudinal wheel slip increases, and the angle θ_m is expressed by an empirical formula as a function of wheel slip [32].

Shear stress distribution

The shear stress distribution is modeled based on the Mohr-Coulomb's failure criterion:

$$\tau_{\max} = c + \sigma \tan\phi \tag{2.22}$$

where $\tau_{\max}$ is the maximum shear stress which the soil can be tolerant before it fails under the normal stress of the sheared surface σ. The maximum stress, also called shear strength, depends on the soil cohesion c and the friction angle of the soil ϕ.

When a wheel drives in the soil, the soil particles around the contact area are sheared by the rotational and sideslip motions of the wheel, and the shear stress develops based on the

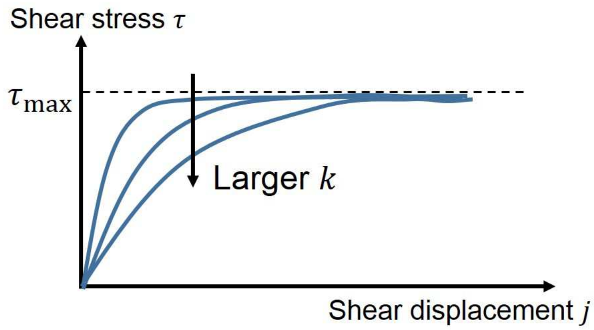

Figure 2.5: Typical shear stress–shear displacement curves of loose, granular soils. The shear deformation modulus k determines how rapidly the stress increases.

displacement of the soil as depicted in Figure 2.5. The shear stress increases with the increase of the shear displacement, and in the case of loose, granular soils, the stress plateaus at the maximum shear stress $\tau_{\max}$. This relationship between the total shear stress τ and the shear displacement j is formulated by Janosh and Hanamoto as follows [35]:

$$\tau = \tau_{\max} \{1 - \exp(-j/k)\} \tag{2.23}$$

where k is a constant parameter called shear deformation modulus. This parameter k represents how rapidly the shear stress develops and decides the shape of the shear stress–shear displacement curves as shown in Figure 2.5. By substituting Eq. (2.22) into Eq. (2.23), the total shear stress distribution at the angle θ is obtained as follows:

$$\tau(\theta) = (c + \sigma(\theta) \tan\phi) \{1 - \exp(-j(\theta)/k)\} \tag{2.24}$$

where $j(\theta)$ is the total shear displacement of the soil at the angle θ. $j(\theta)$ is determined by the displacement in the wheel tangential and lateral directions, $j_t(\theta)$ and $j_l(\theta)$ respectively, as follows:

$$j(\theta) = \sqrt{j_t^2(\theta) + j_l^2(\theta)} \tag{2.25}$$

The displacements are mathematically calculated from the tangential and lateral slip velocities of the soil, v_{jt} and v_{jl}, respectively. These slip velocities are generated by the rotation and sideslip of the wheel, and in the case of positive slip, they are given by the following equations as functions of slip ratio s and slip angle β [28, 32]:

$$v_{jt}(\theta) = r\omega - v_x \cos\theta = r\omega \{1 - (1 - s)\cos\theta\} \tag{2.26}$$

$$v_{jl}(\theta) = -v_y = -r\omega(1 - s)\tan\beta \tag{2.27}$$

The soil displacements in the tangential and lateral directions at the angle θ are obtained by integrating the slip velocities, v_{jt} and v_{jl}, from the entry angle θ_f to θ along the wheel circumference and are given as follows:

$$j_t(\theta) = \int_{\theta}^{\theta_f} v_{jt} \frac{d\theta}{\omega} = r\{(\theta_f - \theta) - (1 - s)(\sin\theta_f - \sin\theta)\} \tag{2.28}$$

$$j_l(\theta) = \int_{\theta}^{\theta_f} v_{jl} \frac{d\theta}{\omega} = -r(1 - s)(\theta_f - \theta)\tan\beta \tag{2.29}$$

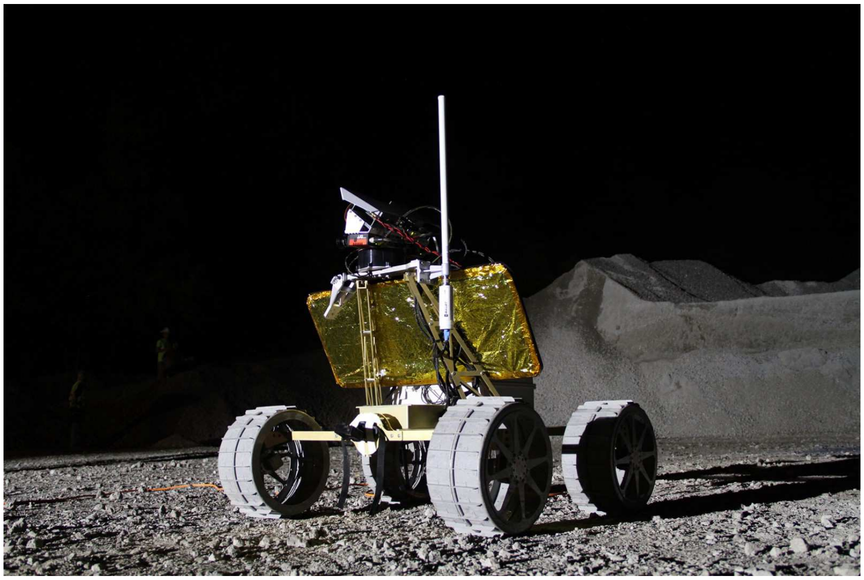

Figure 2.6: Andy 2 rover used in the model-based slope-ascent performance analysis.

Finally, the tangential and lateral shear stresses, τ_t and τ_l, respectively, are determined based on the total shear stress and the slip velocities of the soil, and expressed as follows [36]:

$$\tau_t(\theta) = \frac{v_{jt}(\theta)}{\sqrt{{v_{jt}}^2(\theta) + {v_{jl}}^2(\theta)}} \cdot \tau(\theta) \tag{2.30}$$

$$\tau_l(\theta) = \frac{v_{jl}(\theta)}{\sqrt{{v_{jt}}^2(\theta) + {v_{jl}}^2(\theta)}} \cdot \tau(\theta) \tag{2.31}$$

2.2.2 Tuning of model parameters

The soil parameters described in the previous section are typically treated as soil-specific constants identified from soil testing [25]. However, many studies have found out that using constant parameters results in inaccurate predictions, especially for light-weight and small-sized wheels and at high slip conditions [37, 38, 39]. This is mainly because 1) the terramechanic models were originally developed for heavy and large sized vehicles; 2) the pressure–sinkage formula Eq. (2.20) does not take into account the wheel sinkage induced by the wheel slip, called slip–sinkage or dynamic sinkage; and 3) the effect of grousers is not explicitly considered. Therefore, in this research, two soil parameters, pressure–sinkage modulus k_σ in Eq. (2.20) and the shear deformation modulus k in Eq. (2.23) are treated as variables which depend on the wheel slip. The parameter k_σ basically controls the sinkage value whereas k affects the drawbar pull and lateral force. These parameters were identified as functions of the wheel slip based on single-wheel experiments such that the difference between the model predicted and the experimentally measured forces and sinkage were minimized.

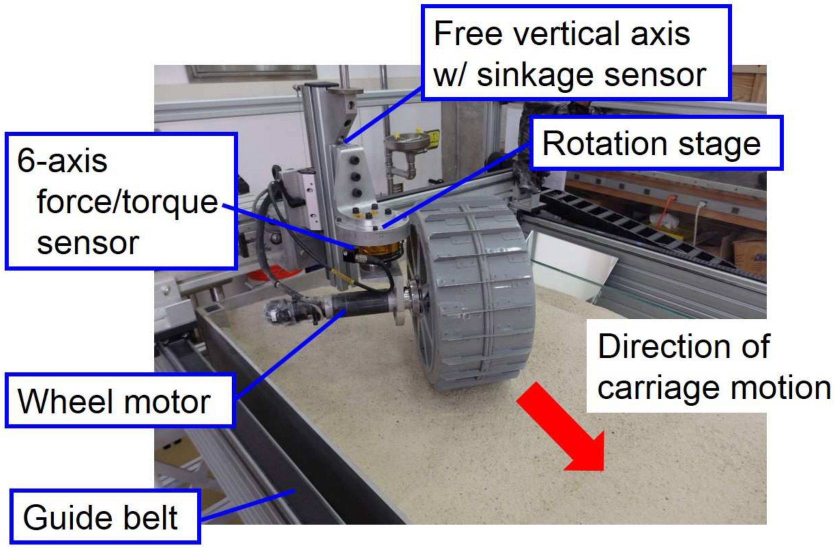

Figure 2.7: Single wheel test rig.

Experiment setup and procedures

Andy 2 rover, shown in Figure 2.6, is selected as the rover for the analysis. Andy 2 is a small, four-wheeled skid-steered rover developed for lunar surface exploration. The rover was designed to have a large track width to wheelbase ratio and low CG height to improve tipover stability and skid-steering capability. Its large and wide wheels respect to its body and tall grousers provide the rover a high slope-ascent capability. The rover is capable of ascending 15^o slope of loose soil with 20–30% slip, and it can ascend slopes up to around 30^o when directly driving uphill.

Single-wheel experiments were conducted to tune the parameters for the Andy 2 rover and GRC-1 lunar regolith simulant. Single-wheel experimentation is a widely used method to characterize tractive performance of vehicles by assessing the relationship between the slip and wheel–soil interaction forces in a single wheel-level [24, 25]. The validity of the inferences of full-vehicle mobility from single wheel experiments have been verified for the longitudinal linear travel cases [40, 41] as long as for steering scenarios [28, 42].

The experimental apparatus used for the parameter tuning tests is shown in Figure 2.7. This single wheel test rig consists of a wheel with a driving motor and an actuated longitudinal axis carriage. The longitudinal motion of the wheel is controlled by the carriage velocity and the wheel angular velocity. The orientation of the wheel can be adjusted by changing the angle of the rotation stage such that an artificial/forced sideslip motion can be generated. In addition, the wheel can move freely in the vertical direction allowing natural wheel sinkage. The sinkage is measured by a string potentiometer attached to the vertical free axis, and the forces on the wheel are measured by a six-axis force/torque sensor. One of the wheels of the Andy 2 rover was mounted on the test rig. The dimension of the wheel is a radius of 150 mm and a width of 150 mm, and the wheel is equipped with 10 mm-high grousers on its smooth surface. The mass of the wheel was set to 6.8 kg which is approximately one quarter of the rover weight.

In this experiment, the soil bin was filled with GRC-1 lunar regolith simulant [43] with 1.2 m long by 0.7 m wide by 0.23 m deep. The mechanical properties of GRC-1 is listed in Table 2.1.

The orientation, or slip angle β, of the wheel was varied from 0 to 30 degrees with an interval of 7.5 degrees. For each slip angle condition, the wheel slip ratio s was set to 0.05, 0.1, 0.2, 0.4, and 0.6. During the tests, the wheel was controlled to rotate with constant tangential velocity of 2.0 cm/s while the speed of the carriage was controlled depending on the slip ratio and slip angle conditions. The wheel drawbar pull, lateral force, and sinkage were measured at the sampling rate of 10 Hz. Tests were conducted at least twice for each condition.

Results of experiment and parameter tuning

Experiment results Figure 2.8 shows the drawbar pull, lateral force and sinkage measured in the single-wheel experiments. The markers represent the average values at each test condition measured during the two tests, and the error bars indicate the 1-standard deviations. Basically, the drawbar pull F_x increases along with the longitudinal slip ratio s and it decreases when the slip angle β increases as shown in Figure 2.8 (a). On the other hand, as we can see in Figure 2.8 (b), the lateral force F_y becomes larger when the slip angle β gets higher since F_y acts as the resistive force against the sideslip. The lateral force reduces as the longitudinal slip s increases. The reason why the F_x and F_y develop inversely is that the total shear force which the soil can generate is limited. The increase of the longitudinal slip enhances longitudinal shear force while limiting the shear force in the other direction, and vice varsa. Figure 2.8 (c) shows the wheel sinkage. The sinkage is dominantly governed by the longitudinal slip and no clear influence of the lateral slip was observed.

Parameter tuning results As mentioned, the two parameters, pressure–sinkage modulus k_σ and shear deformation modulus k, were tuned as functions of the wheel slip s so that the errors between the model curves and the experimentally measured forces and sinkage were minimized by the following two steps. First, for each tested slip condition, the best fit parameter values were identified from the model and the experiment result. Then the approximation functions which is fit to all of the identified values were derived. The obtained functions for the two parameters are as follows:

$$k_\sigma(s) = 2.35e^{-2.65s} \times 10^5 \tag{2.32}$$

$$k(s) = -0.034s^2 + 0.107s + 0.019 \tag{2.33}$$

Table 2.2 lists the parameters used for the computation of the model including the tuned k_σ and k. Figure 2.9 shows the relationship between the parameters and the slip ratio. Note that the types of these functions are chosen based on the observation of the identified parameters at each slip, and there is no theoretical or physical reasoning for the representations.

Table 2.1: Basic mechanical properties of GRC-1 (loosened) [43].

Particle size	0.05–2 mm
Bulk density	1630 kg/m^3
Friction angle	33.7 deg
Cohesion	$<$ 1 kPa

Table 2.2: Parameters used in the analytical model. Soil parameters were adopted from [43].

Parameter	Description	Value	Unit
W	Wheel weight	66.2	N
r	Wheel radius	0.16	m
b	Wheel width	0.15	m
c	Soil cohesion	500	Pa
ϕ	Internal friction angle	33.7	deg
n	Sinkage exponent	1.23	-
k_σ	pressure–sinkage modulus (fixed)	4.20×10^5	N/m^2
k_σ	pressure–sinkage modulus (tuned)	$2.35e^{-2.65s} \times 10^5$	N/m^2
k	Shear deformation modulus (fixed)	0.024	m
k	Shear deformation modulus (tuned)	$-0.034s^2 + 0.107s + 0.019$	m

Table 2.3: RMS errors of the model predictions.

	F_x [N]	F_y [N]	z [mm]
Fixed parameters	15.15	9.46	19.50
Tuned parameters	2.54	3.30	5.22

Comparison of the experiment results and the model curves The solid curves in Figure 2.8 represent the model curves with the k_σ and k treated as functions of the wheel slip whereas the dashed curves are the model which uses fixed k_σ and k identified from the soil testing reported in [43]. (The original pressure–sinkage moduli k_c and k_ϕ reported in [43] were coupled together into k_σ which was computed for the dimension of the Andy 2 wheel.) In addition, the root-mean-square (RMS) errors of the predicted F_x, F_y, and z are calculated for both the tuned and fixed soil parameters, and listed in Table 2.3. The model curves using both the tuned and original parameters capture the similar trends observed experimentally; however the curves with tuned parameters achieve better accuracies. One notable thing observed from Figure 2.8 (c) is that the sinkage prediction with the fixed parameters does not show any clear change along with the increase of the slip. This indicates the limitation of the conventional terramechanic theory which cannot express the slip–sinkage phenomenon. On the other hand, the sinkage predicted with tuned parameters successfully follows the slip–sinkage trend observed in the experiments.

From Figure 2.8 and Table 2.3, it can be said that the model using the tuned k_σ and k provides sufficiently accurate predictions of the slip–force relationships for simulations. Figure 2.10 shows the 3-dimensional view of the drawbar pull and lateral force as functions of the longitudinal and lateral slip computed based on the wheel–soil interaction model.

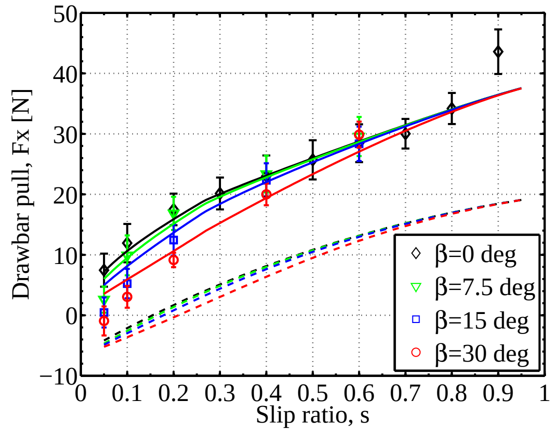

(a) Drawbar pull F_x

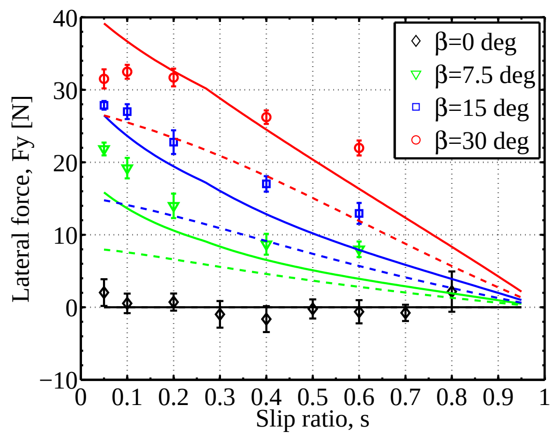

(b) Lateral force F_y

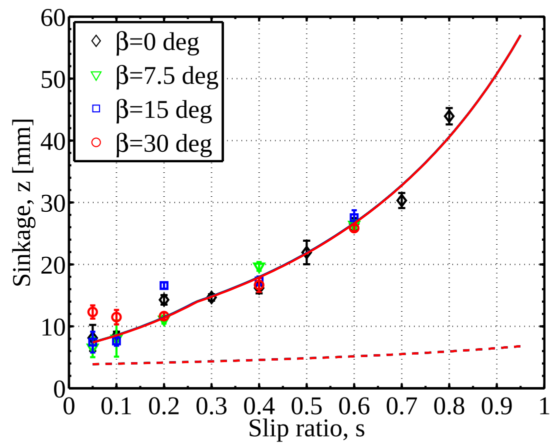

(c) Sinkage z

Figure 2.8: Model predictive forces and sinkage plotted with experimental results. Markers and error bars represent the average and 1-standard deviation values of the measured forces from the experiment. The solid curves show the analytical model with tuned parameters whereas the dashed curves indicate the model with the original fixed soil parameters.

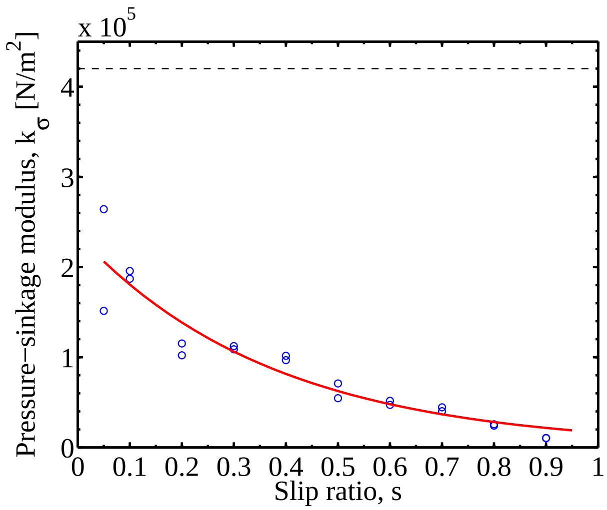

(a) Pressure–sinkage modulus k_σ

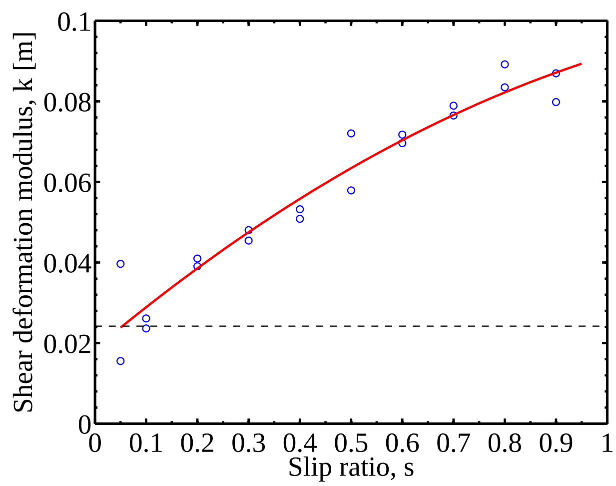

(b) Shear deformation modulus k

Figure 2.9: Result of the parameter tuning of k_σ and k. The markers represent the points best fitted for the corresponding slip conditions. The red curves show the approximate functions whereas the black dashed lines are the fixed values measured from soil tests.

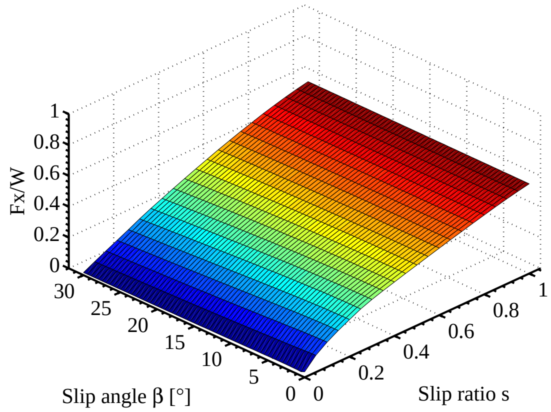

(a) Drawbar pull F_x

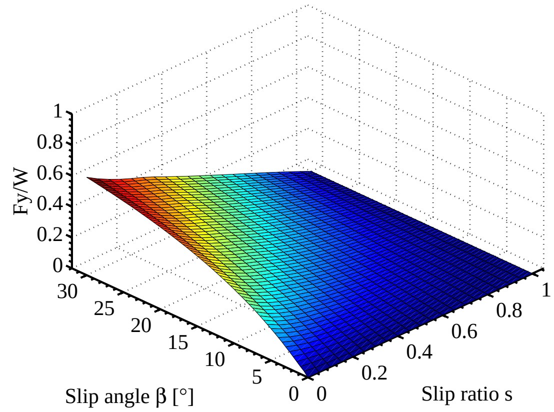

(b) Lateral force F_y

Figure 2.10: Relationship between slip and forces. The forces were normalized to the weight W.

2.3 Slope-ascent performance analysis

In this section, the slope-ascent performance of the Andy 2 rover is analyzed based on numerical simulations using the slope-ascent and wheel–soil interaction models described above. Assuming that the change in the mechanical properties of the soil on sloped terrain, if any, is negligible, the wheel forces generated from the wheel–soil interaction can be determined from Eqs. (2.8)-(2.10) given the slip ratio s and slip angle β as shown in Figure 2.10. Furthermore, the forces necessary for the rover to steadily climb up a slope are provided in Eqs (2.1)-(2.5) and in Figure 2.2. Hence, the mapping between the slope & angle of attack and wheel slip can be obtained from these relationships.

2.3.1 Simulation procedures

In the simulation, the rover longitudinal slip ratio s and lateral slip angle β are predicted for the given slope angle θ_0 and angle of attack α. In this simulation, the slope angle θ_0 was varied from 10^o to 30^o, and the angle of attack of the rover α was varied from 10^o to 90^o.

The simulation flow to predict the rover slip is summarized as follows:

1. Provide initial guesses of the slip ratio s, slip angle β, and sinkage z.
2. Calculate F_x, F_y and F_z for the s, β, and z based on Eqs (2.8), (2.9), and (2.10).
3. Check if Eqs. (2.1), (2.2) and (2.3) are satisfied.
4. If not, update s, β and/or z and return to 2.

The same model parameters used in the previous section (Table 2.2) were used for the computation of the forces F_x, F_y and F_z. In the update phase (4), Newton method was utilized to find the wheel slip and sinkage values, s, β and z, that minimize the errors between the model-predicted

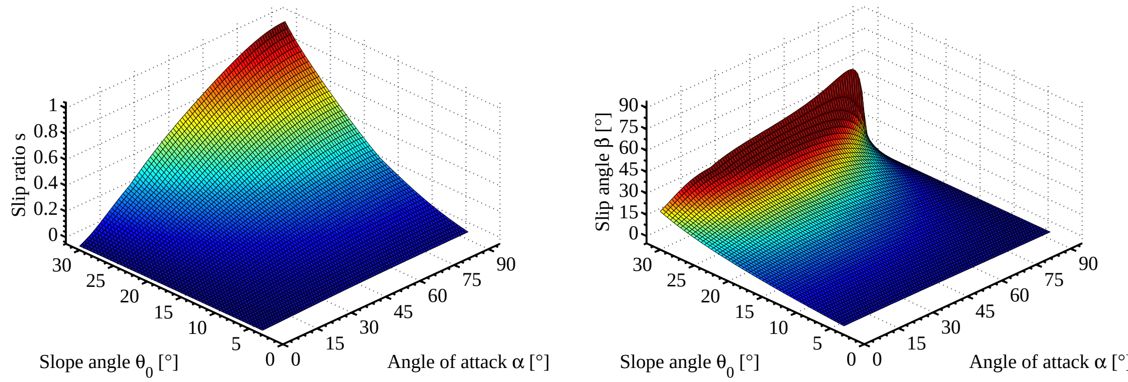

(a) Slip ratio s (b) Slip angle β

Figure 2.11: Predicted longitudinal and lateral slip of Andy 2 for various slopes and angles of attack.

forces and the theoretical ones given in Eqs. (2.1), (2.2) and (2.3):

$$\begin{bmatrix} s^* \\ \beta^* \\ z^* \end{bmatrix} = \arg\min_{s,\beta,z} \sum_{i=x,y,z} \left(F_i - F_{im}(s, \beta\, z)\right)^2 \tag{2.34}$$

where F_i $(i = x, y, z)$ are forces required for the steady state slope-ascent while F_{im} are computed forces from the predicted s, β, and z.

2.3.2 Predicted wheel slip

The predicted slip ratio s and slip angle β for various combinations of slopes and angles of attack is shown in Figure 2.11. Figures 2.12 and 2.13 show the more detailed look of the relationship between the angle of attack and predicted slip. These figures also show the slip curves predicted based on a full-vehicle model which takes into account the weight distribution on slopes. From these figures, the single-wheel representation of a rover provides sufficiently close prediction results to the slip computed based on the full-vehicle model in the case of the steady state linear slope-ascent. Therefore, the slope-ascent model based on the single-wheel representation are utilized for the rest of the analysis. More detailed description of the full-vehicle model is introduced in Appendix A and the validity of the single-wheel representation is discussed there.

As seen in the Figures, both the longitudinal and lateral slip increase when the slope becomes higher. When the angle of attack becomes smaller than 90^o, the slip ratio monotonically reduces as shown in Figure 2.12. This trend agrees with the evidences reported in literature. The reduction of the longitudinal slip along with the angle of attack is attributed to the decrease of the longitudinal gravitational resistance when the rover heading changes from the uphill direction to the side-slope direction as seen in Figure 2.2 (a).

On the other hand, the slip angle behaves in a slightly complicated way as seen in Figure 2.13 because of the complex wheel–soil interaction where the all forces and slip in the longitudinal and lateral directions are coupled each other. When the angle of attack is 90^o, no sideslip is

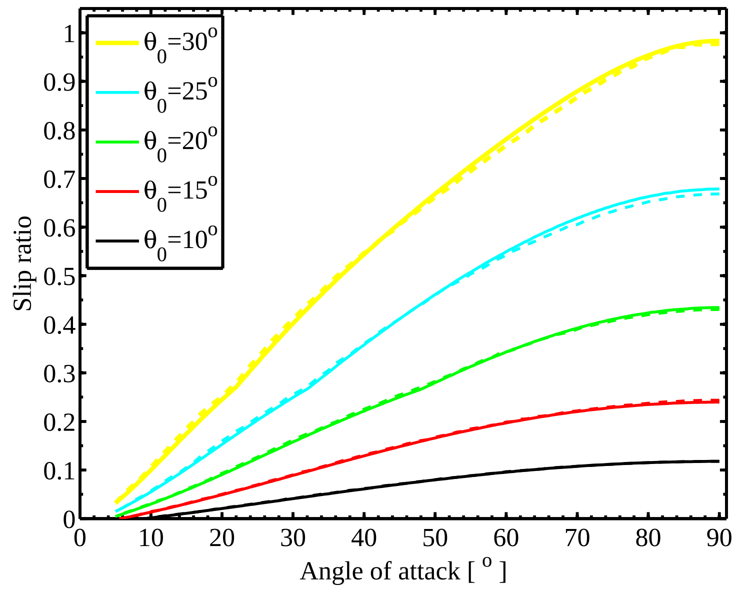

Figure 2.12: Predicted slip ratio of Andy 2 rover from the single-wheel model (solid curves) and full-vehicle model (dashed curves) for various angles of attack α and slopes θ_0.

induced since any external force in the lateral directional acts on the rover. The sideslip starts to increase when the angle of attack gets smaller than 90^o since the lateral gravitational resistance increases along with the reduction of the angle of attack as shown in Figure 2.2 (b). At the angle of attack close to 90^o, the slip angle increases rapidly. This is because the longitudinal slip becomes relatively high around 90^o angle of attack as seen in Figure 2.12. The high longitudinal slip results in the greater soil shearing in the wheel tangential direction, and the increase of the tangential soil shearing limits the capability of the soil to generate the lateral shear resistance against the sideslip. Therefore, the wheel is subjected to experience relatively large sideslip around 90^o angle of attack to generate a sufficient level of the lateral force. This causes the rapid increase of the side slip angle at the angle of attack close to 90^o. As the longitudinal slip and tangential shear stress reduces when the angle of attack further decreases, the capacity of the soil to generate lateral shear resistance increases, and the required lateral force can be obtained with smaller slip angles. This is why the slip angle reduces when the angle of attack becomes smaller than the angle that corresponds to the peak slip angle as shown in Figure 2.12.

The diagonal black dashed line depicted in Figure 2.13 represents the boundary states at which the slip angle β becomes equal to the angle of attack α. On this boundary, the rover traverses purely laterally along the transverse direction of slopes without any uphill progress. When the slip angle goes above the boundary, the rover starts to slide downhill.

2.3.3 Trajectory analysis

Based on the predicted rover slip, trajectories of the rover at several angles of attack were computed assuming a quasi-static steady state condition. In this simulation, the rover was commanded to drive toward the target line located 3 m uphill from a start location at angles of attack

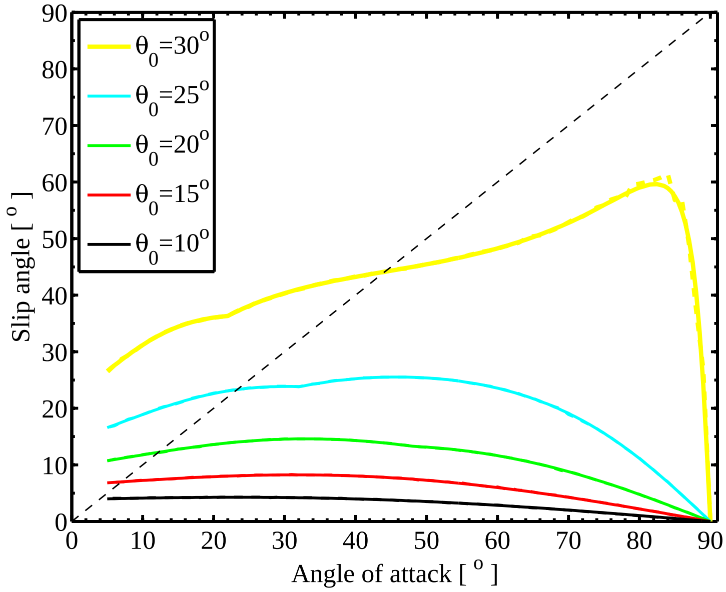

Figure 2.13: Slip angle of Andy 2 predicted based on the single-wheel model (solid curves) and full-vehicle model (dashed curves) for various angles of attack α and slopes θ_0. The diagonal black dashed line represents the slip angle which equals to the angle of attack. The rover can never ascend the slopes with the angles of attack above this line.

of 15^o, 30^o, 45^o, 60^o, 75^o, and 90^o. The commanded longitudinal velocity was set to 5 cm/s.

Figures 2.14–2.16 show example rover trajectories on the slopes of 20^o, 25^o, and 30^o, respectively. On the 20^o slope all of the commanded angles of attack could ascend the slope as shown in Figure 2.14 although the shallower angles of attack required longer travel distances. In addition, due to the downhill sideslip, the resultant trajectory of the 15^o angle of attack became almost parallel to the sideslope. The 90^o angle of attack reached the goal line first in this case. The required travel time, travel distance, and the corresponding slip ratio and slip angle for each angle of attack are listed in Table 2.4. The best performance values are highlighted in red.

The table also lists the average power and total energy consumed during the slope-ascent. The power P and energy consumption E were estimated based on the following equations:

$$P = \frac{1}{\eta_A} T_R \omega \tag{2.35}$$

$$E = P \cdot t \tag{2.36}$$

where η_a denotes the power efficiency of the driving actuator. T_R is the driving torque of the wheel estimated based on Eq. (2.15), and ω is the commanded angular velocity of the wheel. At last, t is the travel time required to reach the goal line. As seen in the table, the average power consumption reduces as the angle of attack gets smaller, and it becomes the minimum at 15^o angle of attack among the commanded angles in the simulation. This is because the resistive force tangential to the wheel circumference declines with the reduction of the longitudinal gravitational resistance. On the other hand, 15^o angle of attack could not achieve the minimum total energy consumption. Rather the energy consumed with the angle of attack became significantly higher than the other angles of attack due to the longest travel time despite of the smallest power consumption. The lowest energy consumption among tested angles of attack was accomplished by the path of 45^o angle of attack. On this route, the rover can ascend the slope with 8.1% lower energy consumption compared to the 90^o direct ascent.

In Figure 2.15, trajectories on the 25^o slope are shown. In this case, all of the angles of attack could ascend the slope, except for 15^o. At 15^{o}angle of attack, the slip angle became 21.0^o exceeding the angle of attack. Thereby the rover could not make any uphill progress and slid downhill. Again, the rover reached the goal line fastest with the 90^o angle of attack route on this slope. The results of the 25^o slope-ascent are summarized in Table 2.5. The total energy consumption was lowest with the 60^o angle of attack route: 11.8% less energy was consumed with respect to the 90^o angle of attack.

The results of the 30^o slope case are shown in Figure 2.16 and summarized in Table 2.6. In this figure, only the trajectories of the angles of attack of 45^o or larger are shown since the rover could not ascend the slope with the other two routes of smaller angles of attack. The slip ratio at 90^o angle of attack became $s = 0.983$, and the rover could barely make an uphill progress although it finally reached the goal line with an hour-long travel. The 60^o angle of attack arrived on the goal line first with the lowest energy consumption; its required time and energy were 75.2% and 81.6% smaller, respectively, with respect to the 90^o angle route.

From these observations, it can be said that the 90^o angle of attack is the most effective route among others because of the shortest travel time and distance, and the moderate energy consumption unless the longitudinal slip becomes extremely high. In such extreme case, some routes with shallower angles of attack become beneficial to ascend the slope.

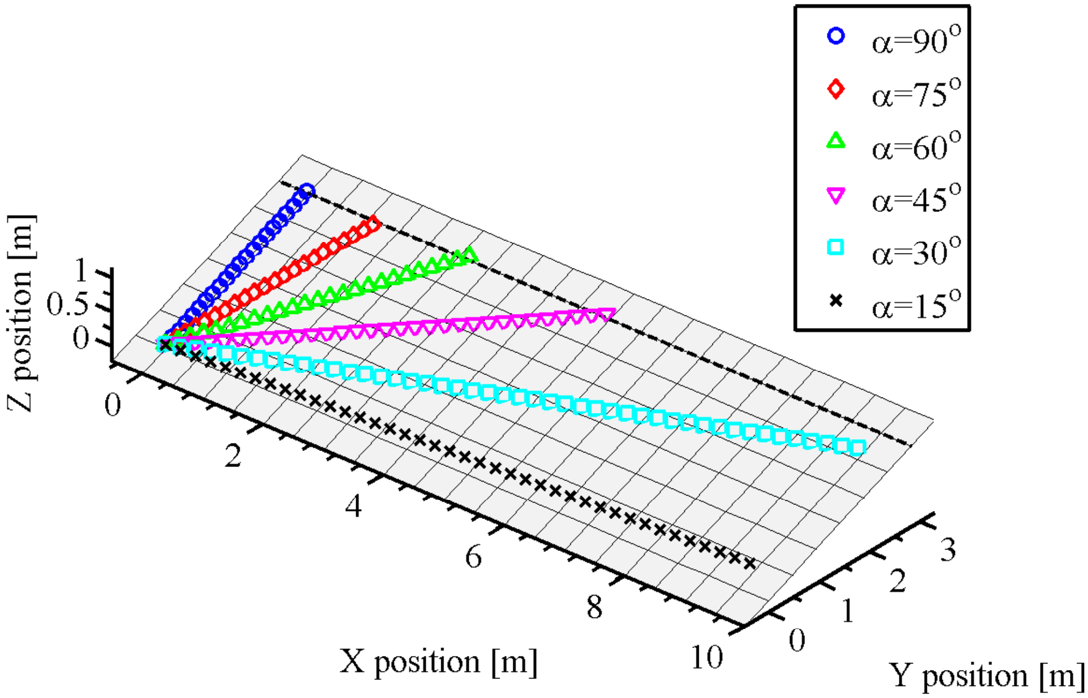

Figure 2.14: Predicted trajectories on 20^o slope. The black dashed line represents the goal line. The locations of the rover center are plotted with an interval of 5 sec.

Table 2.4: Slope-ascent simulation results on 20° slope. For each angle of attack (α), the following evaluation criteria are listed: elapsed time (t), travel distance (d), slip ratio (s), slip angle (β), power consumption (P), total energy consumption (E), uphill velocity (v_Y), and climbing efficiency (η_Y). The best performance values are highlighted in red.

α [°]	t [s]	d [m]	s	β [°]	P [W]	E [kJ]	v_Y [cm/s]	η_Y
90	106.1	3.0	0.434	0.0	7.01	0.74	2.83	0.365
75	108.8	3.2	0.410	6.9	6.69	0.73	2.76	0.373
60	119.7	4.0	0.343	11.6	5.83	0.70	2.51	0.390
45	149.8	5.8	0.250	13.8	4.56	0.68	2.00	0.398
30	258.9	11.3	0.158	14.6	3.07	0.80	1.16	0.341
15	1591.8	76.8	0.059	12.8	1.46	2.33	0.19	0.117

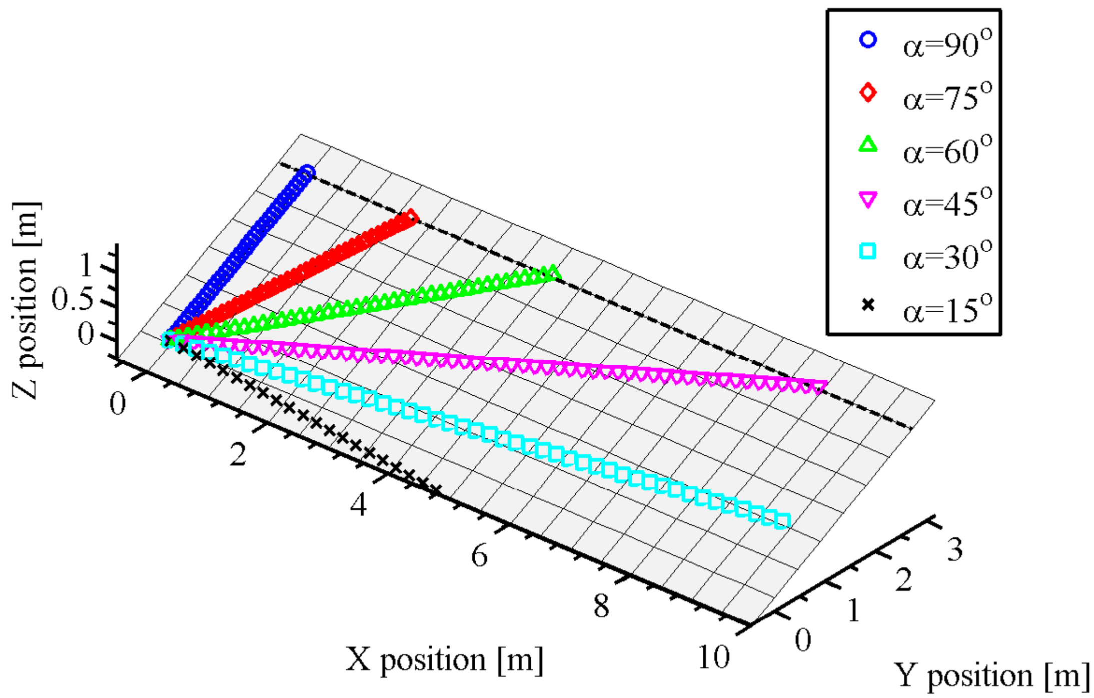

Figure 2.15: Predicted trajectories on 25^o slope. The black dashed line represents the goal line. The locations of the rover center are plotted with an interval of 5 sec.

Table 2.5: Slope-ascent simulation results on 25° slope. The denotations are described in Table 2.4.

α [°]	t [s]	d [m]	s	β [°]	P [W]	E [kJ]	v_Y [cm/s]	η_Y
90	186.6	3.0	0.678	0.0	9.74	1.82	1.61	0.185
75	188.5	3.5	0.644	15.6	9.22	1.74	1.59	0.193
60	205.4	5.1	0.549	23.6	7.87	1.61	1.46	0.208
45	275.7	9.0	0.411	25.5	6.02	1.66	1.09	0.202
30	684.5	28.1	0.249	23.9	3.96	2.71	0.44	0.124
15	—	—	0.102	21.0	1.88	—	-0.50	—

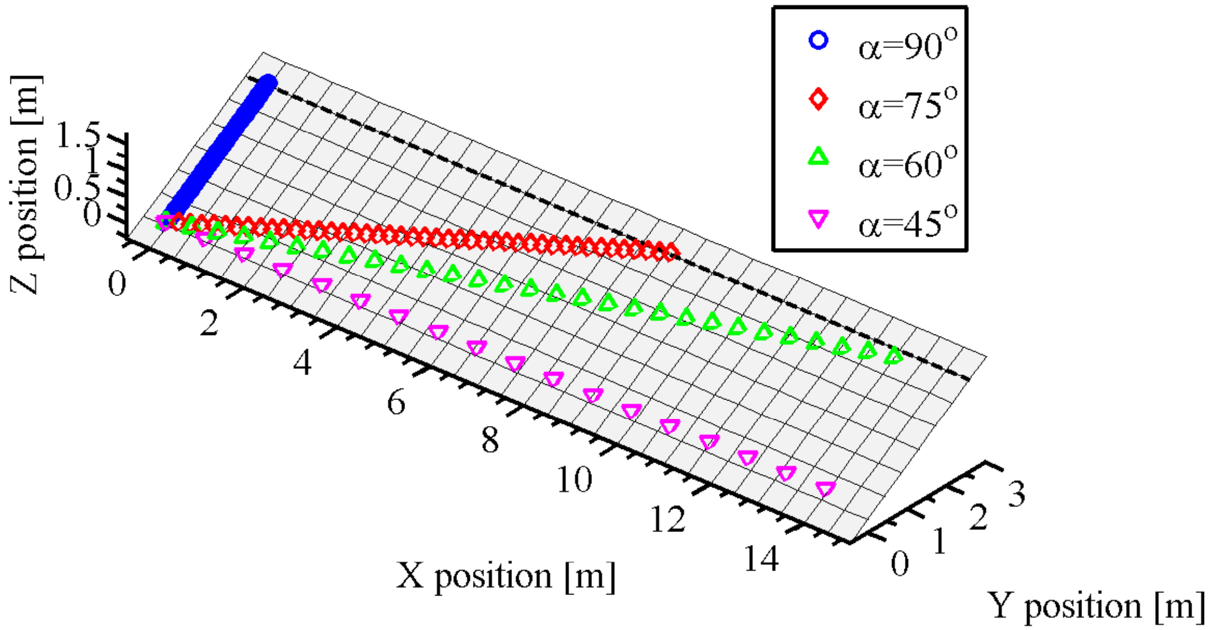

Figure 2.16: Predicted trajectories on 30^o slope. The black dashed line represents the goal line. The locations of the rover center are plotted with an interval of 30 sec. The trajectories of $\alpha = 15°$ and $\alpha = 30°$ are not shown since these angles of attack could not make uphill progresses.

Table 2.6: Slope-ascent simulation results on 30° slope. The denotations are described in Table 2.4.

α [°]	t [s]	d [m]	s	β [°]	P [W]	E [kJ]	v_Y [cm/s]	η_Y
90	3607.3	3.0	0.983	0.0	14.230	51.33	0.08	0.008
75	1296.9	9.2	0.921	55.9	13.016	16.88	0.23	0.024
60	896.4	14.8	0.781	48.3	10.539	9.45	0.33	0.042
45	9416.4	258.2	0.608	44.3	7.778	73.24	0.03	0.005
30	—	—	0.402	40.4	4.992	—	-0.71	—
15	—	—	0.175	34.4	2.316	—	-1.66	—

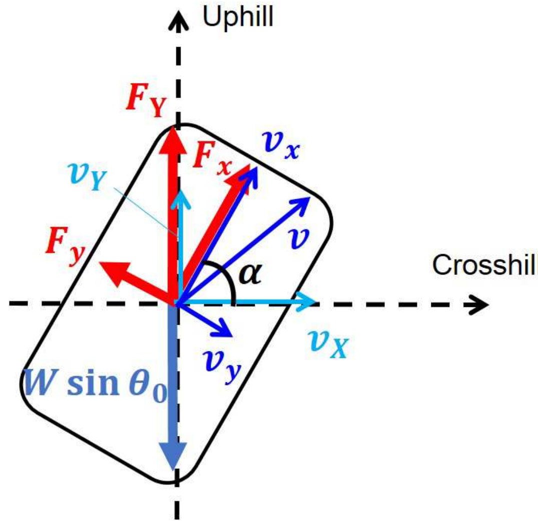

Figure 2.17: Definitions of the uphill velocity v_Y and the uphill force F_Y. The rover/wheel is ascending a slope of an angle θ_0 with an angle of attack α.

2.3.4 Uphill velocity and climbing efficiency

To evaluate the effectiveness of each angle of attack for slope-ascent, two additional metrics are introduced in this section: the uphill velocity and climbing efficiency.

As shown in Figure 2.17, the uphill velocity v_Y is the velocity component in the uphill direction, and it is given in the following equation:

$$v_Y = v_x \sin\alpha - v_y \cos\alpha = r\omega(1-s)(\sin\alpha - \tan\beta\cos\alpha) \tag{2.37}$$

where v_x and v_y are the rover velocity in the vehicle longitudinal and lateral directions respectively. r denotes the wheel radius and ω denotes the wheel angular velocity. s and β are the longitudinal slip ratio and lateral slip angle respectively, and α is the angle of attack. v_Y indicates how fast the rover can drive uphill.

The other metric, the climbing efficiency η_Y, indicates how efficiently the rover can drive up a slope, and it is defined as the ratio of the output power to the input power during the ascent:

$$\eta_Y = \frac{\text{Output power}}{\text{Input power}} = \frac{F_Y v_Y}{T_R\omega/\eta_a} \tag{2.38}$$

where F_Y denotes the uphill directional force extracted by the rover through the terrain as depicted in Figure 2.17. T_R denotes the wheel drive torque estimated from Eq (2.15). η_a is the power efficiency of the actuator. If the rover/wheel is ascending the slope at a steady, constant speed, then the uphill force equals to the downhill gravitational resistance:

$$F_Y = F_x \sin\alpha + F_y \cos\alpha = W \sin\theta_0 \tag{2.39}$$

By substituting Eqs (2.37) and (2.39) into Eq. (2.38), the climbing efficiency can be re-expressed as follows:

$$\eta_Y = \eta_a \frac{W \sin\theta_0 \cdot r(1-s)(\sin\alpha - \tan\beta\cos\alpha)}{T_R} \tag{2.40}$$

Higher the η_Y is, the more efficient the rover motion is.

Figures 2.18 and 2.19 show the estimated uphill velocity and climbing efficiency, respectively, for various angles of attack and various slope angles. In addition, the uphill velocity and climbing efficiency in the simulations in Section 2.3.3 are listed in Tables 2.4–2.6.

In Figure 2.18, the uphill velocity v_Y relative to the commanded velocity is plotted. Negative uphill velocity indicates that the rover cannot ascend the slope with the corresponding angle of attack. As shown in the figure, v_Y becomes its maximum at 90^o angle of attack for the slopes of 10^o–25^o, and it monotonically declines with the reduction of the angle of attack. However the maximum velocity for 30^o slope is located at the smaller angle of attack than 90^o—around 62.5^o. This is because on the slope, the longitudinal slip becomes almost 100% at 90^o angle of attack as shown in Figure 2.12.

The climbing efficiency η_Y, on the other hand, is almost constant on 10^o and 15^o slopes even if the angle of attack is reduced from 90^o until a certain angle as seen in Figure 2.19. The efficiency suddenly drops at angles of attack smaller than that and eventually becomes below zero due to the increase of the slip angle. On slopes steeper than or equal to 20^o, a peak in the efficiency begins to appear at a certain angle of attack. The difference between the maximum efficiency and that of 90^o become more significant as the slope becomes steeper.

These trends coincide with the simulation results described in Section 2.3.3. Notice that the highest climbing efficiency and the lowest energy consumption are achieved by the same angles of attack for each slope as seen in Tables 2.4–2.6. This is because the climbing efficiency η_Y and the energy consumption E are in an inverse relationship each other:

$$\eta_Y = \frac{F_Y v_Y}{P} = \frac{F_Y d_Y/t}{P} = \frac{F_Y d_Y}{Pt} = \frac{F_Y d_Y}{E} \propto \frac{1}{E} \tag{2.41}$$

where $d_Y = v_Y \cdot t$ is the travel distance in the uphill direction which is a constant in the simulations. Therefore, the lower climbing efficiency indicates the lower total energy consumption. Consequently the climbing efficiency can be considered as a criteria for both the efficiency of the output power and the required total energy.

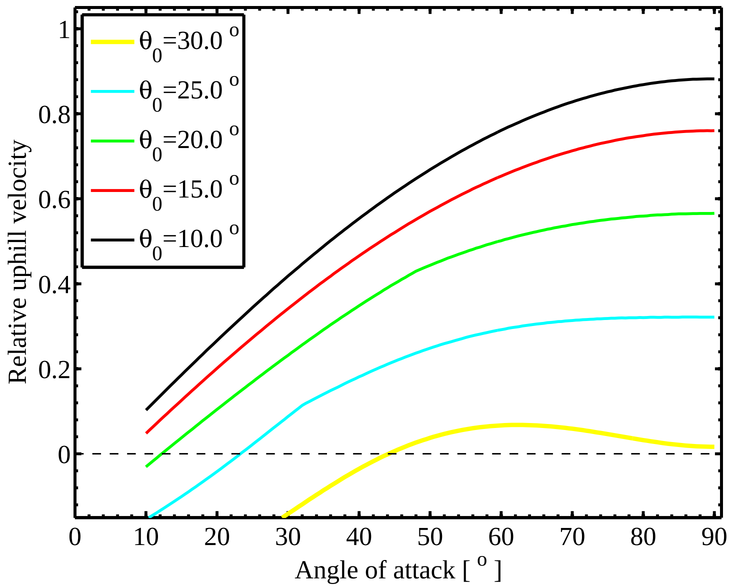

Figure 2.18: Estimated uphill velocity of Andy 2 rover for various angles of attack and slopes. The relative uphill velocity means the uphill velocity v_Y normalized to the commanded velocity $r\omega$.

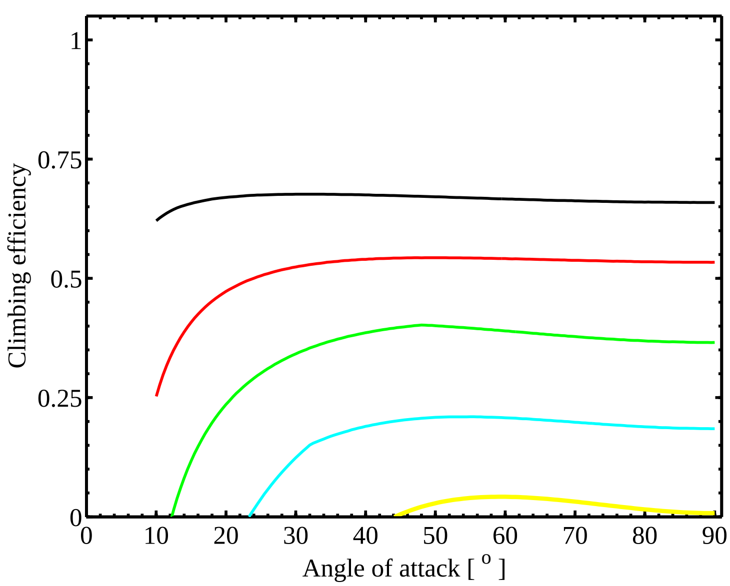

Figure 2.19: Estimated climbing efficiency of Andy 2 rover for various angles of attack and slopes.

2.4 Summary

In this chapter, a slope-ascent rover model was introduced to analyze the effect of the angle of attack on slope-ascent performance of a rover. The model consists of a steady state slope-ascent conditions and terramechanics-based wheel–soil interaction. The terramechanic model was tuned such that the model implicitly incorporate the effects of the small-sized, light-weighted wheel, slip–sinkage phenomena at high slip conditions, and the surface profile of a wheel.

The followings are the key findings from the analysis based on the single-wheel slope-ascent model for the Andy2 rover:

1. On higher slopes, both the longitudinal and lateral rover slip become larger.
2. The longitudinal slip reduces when the angle of attack gets smaller than 90^o.
3. The lateral slip rapidly increases when the angle of attack becomes smaller than 90^o, and it plateaus or decreases when the angle of attack decreases more.
4. The uphill velocity decreases with the reduction of the angle of attack on small and medium slopes. However it has a peak at an angle of attack smaller than 90^o on extremely steep slopes.
5. The climbing efficiency does not significantly change with the reduction of the angle of attack until certain angles of attack on shallow slopes, but a peak appears at an angle of attack smaller than 90^o on extremely steep slopes.

From these observations, for most of slopes 90^o angle direct ascent can be said the most effective angle because of the shortest travel time and distance, and also because of its moderate energy consumption. However, on extreme slopes, the longitudinal slip becomes around 100% when the rover directly ascends. In this extreme case, some routes with shallower angles of attack can still ascend the slope with higher power efficiency.

Chapter 3

Slope-Ascent Experiments

This chapter experimentally assesses the effect of the angle of attack on slope-ascent capability of a rover and discusses the validity of the slope-ascent model introduced in Chapter 2. Section 3.1 describes the rover and test field utilized in the test campaign. Section 3.2 reviews the evaluation criteria to compare the slope-ascent performance of a rover with various angles of attack. In Section 3.3, the test procedures are described. The results of the experiments are shown in Section 3.4. The validity of the model-based analysis is also discussed in this section.

3.1 Test rover and field

In this set of experiments, the Scarab rover shown in Figure 3.1 was used as a rover testbed. The mass of the rover was set to 400 kg and the four rigid wheels of 71 cm (diameter) by 18 cm (width) were mounted. The cylindrical surface of the wheels are covered with sandpaper and has no grouser on it. The rover has active suspension which controls the angles of left and right side rocker arms and the rover roll angle; however in this study, the suspension was inactivated to assess the performance of a general type of rovers that do not have such capability. The rocker angles of the both side were set such that the wheelbase and CG height became the nominal values. Specifications of the rover in the experiments are listed in Table 3.1.

Table 3.1: Specifications of Scarab rover in the experiments. CG X and Y locations indicate the planar position of the CG in the longitudinal and lateral directions, respectively, with respect to the geometrical center of the rover.

Mass	400 kg
Wheel diameter	71 cm
Wheel width	18 cm
Track width	140 cm
Wheelbase	120 cm
CG X location	4 cm
CG Y location	0 cm
CG height	64 cm

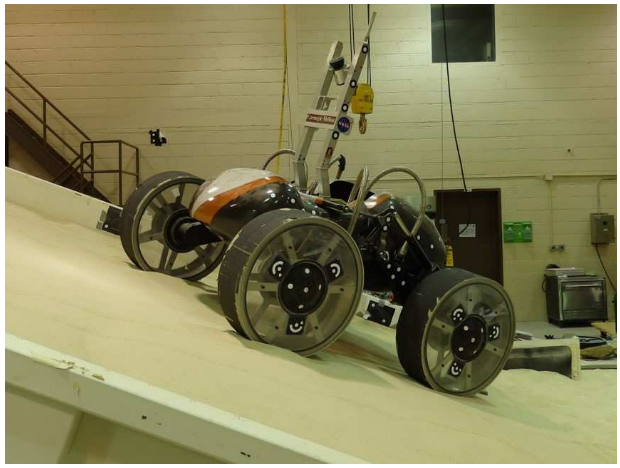

Figure 3.1: Scarab rover used for the slope-ascent experiments.

Figure 3.2: SLOPE Laboratory at NASA Glenn Research Center.

Tests were conducted using an adjustable tilt bed in the Simulated Lunar Operations (SLOPE) laboratory of the NASA Glenn Research Center (Figure 3.2). The size of the tilt bed is the length of 6 m by the width of 4.5 m and it is filled with 0.23 m deep of GRC-1 lunar regolith simulant which was also used in the single-wheel experiment in the previous chapter.

3.2 Evaluation criteria

In the experiments, the following evaluation criteria which were introduced in the previous chapter are used again to evaluate the slope-ascent performance of the rover: slip ratio, slip angle, uphill velocity, and climbing efficiency. The definitions of these parameters are reviewed bellow.

Slip ratio: The slip ratio represents the longitudinal slip of a rover. The slip ratio s is defined as the ratio of the actual travel velocity of the rover v_x to the commanded reference velocity v_{ref}:

$$s = \begin{cases} 1 - \frac{v_x}{v_{ref}} & (\text{if} \quad v_x \leq v_{ref}, \quad \text{driving}) \\ \frac{v_{ref}}{v_x} - 1 & (\text{if} \quad v_x > v_{ref}, \quad \text{breaking}) \end{cases} \tag{3.1}$$

The lower the absolute value of the slip ratio is, the better tractive capability the rover has on the terrain.

Slip angle: The sideslip or skid in the transverse direction of the vehicle is measured by the slip angle β:

$$\beta = \tan^{-1}\left(\frac{v_y}{v_x}\right) \tag{3.2}$$

where v_y is the rover lateral velocity caused by the sideslip.

Uphill velocity: The uphill velocity v_Y is the uphill component of the rover velocity, and its relationship to the velocities in the rover coordinates frame v_x and v_y is given as

$$v_Y = v_x \sin\alpha - v_y \cos\alpha \tag{3.3}$$

where α is the angle of attack.

Climbing efficiency The climbing efficiency η_Y measures the power efficiently of the robot motion in the uphill direction, and it is given by

$$\eta_Y = \frac{\text{Output power}}{\text{Input power}} = \frac{F_Y v_Y}{P} \tag{3.4}$$

where F_Y denotes the uphill direction force generated by the rover through the terrain and it becomes $F_Y = W\sin\theta_0$ at a steady state. P denotes the electrical power input to the rover actuators during the slope-ascent. Higher η_Y indicates more efficient motion the rover can achieve on the terrain.

3.3 Experiment procedures

In the experiments, the tested slope angle was varied from 10 degrees to 25 degrees with an interval of 2.5 degrees. The angle of attack of the rover was varied from 30 degrees to 90 degrees.

At the beginning of each test, the soil was well loosened and leveled. Then the angle of the tilt table was set to the desired slope angle. The actual terrain inclination was estimated by projecting dot patterns onto the terrain surface and obtaining a fitted plane based on the point could data of the terrain surface which was captured by using a stereo camera. The rover was then placed using a crane such that the slope surface was not disturbed and no significant initial wheel sinkage was induced. The orientation of the rover was set to the desired angle of attack (Figure 3.3 (a)) using a reference laser maker. Small amount of drifting occurred during the placement and slight deviation of the actual initial angle of attack from the target angle happened. Table 3.2 lists the target slope angle and angle of attack along with the corresponding actual angles in each test.

After the placement, the rover was commanded to drive straightly up a slope at the angle of attack for 30 seconds. All of the wheels were driven equally at the rotational speed of 1.24 rpm

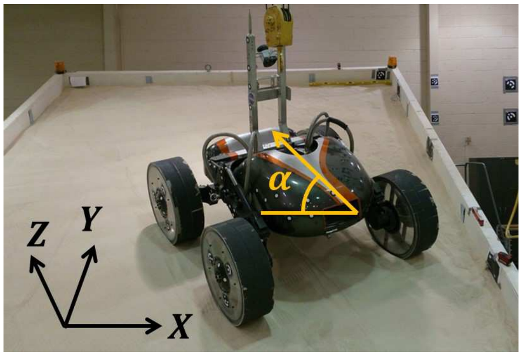

(a)

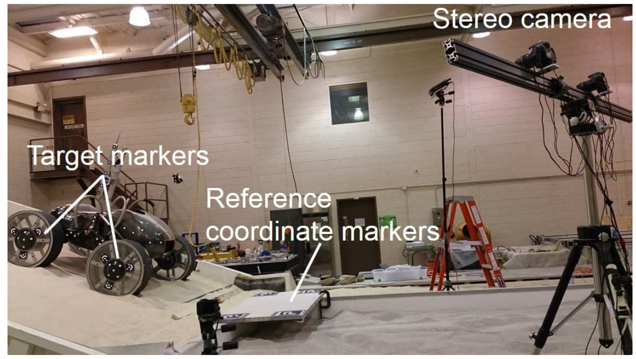

(b)

Figure 3.3: Setup of the slope-ascent experiments. (a) The rover was placed on the slope at an angle of attack α by using a crane. (b) The stereo camera captures the target markers on the wheels and a software compute their positions with respect to the reference coordinate markers.

which corresponds to the linear speed of 4.5 cm/s. During each test, the motion of the rover was tracked using a stereo camera shown in Figure 3.3 (b). The pair of cameras captured stereo images of the target markers on the left front and rear wheels of the rover every 2 seconds. The three-dimensional positions of the wheels at each time frame were computed offline with respect to the fixed reference coordinate markers by using a software developed by GOM [44]. From the trajectory extracted, the average rover velocities were then calculated, and the average values of the evaluation metrics described in Section 3.2 were estimated.

3.4 Experiment results

3.4.1 Rover trajectory

Some of the rover trajectories measured in the experiments are shown in Figures 3.4–3.7. In these figures, the dashed lines indicate the commanded trajectories while the markers represent the actual rover trajectories plotted at an interval of 2 sec.

As seen in these figure2, the longitudinal progresses of the rover were shorter than the length of the commanded trajectories due to the longitudinal slip, and the rover trajectories deviated from the commanded lines toward the downhill direction due to the lateral slip. It can be also seen that the shallower angles of attack could travel longer distance because of lower slip ratio.

On the slope of 20^o, the angles of attack of 90^o and 75^o could barely make an uphill progress while 60^o angle of attack slid downhill as shown in Figure 3.6. The longitudinal slip exceeded 90% in these cases. On the 25^o slope, none of the angles of attack tested could make uphill progresses as seen in Figure 3.7; the rover downslid at 75^o and 60^o angles of attack, and the longitudinal slip reached 100% at 90^o angle of attack.

In addition to the experiments, numerical simulations of the rover motions were conducted based on the slope-ascent model for Scarab rover. For the model computation, the wheel–soil contact parameters listed in Table 2.2 were used along with the weight and wheel size of the

Table 3.2: Slope-ascent test matrix. Target and actual slope angles and angles of attack are listed.

Target slope	Target angle of attack	Actual slope	Actual angle of attack
10°	30°	10.7°	29.3°
	45°	10.7°	52.5°
	60°	10,8°	53.5°
	75°	10.8°	71.6°
	90°	Data collection failure	
12.5°	30°	13.3°	28.4°
	45°	13.2°	50.4°
	60°	13.4°	56.3°
	75°	13.3°	73.0°
	90°	13.1°	90.7°
15°	30°	15.5°	32.3°
	45°	15.9°	46.9°
	60°	15.0°	55.4°
	75°	15.6°	72.2°
	90°	15.5°	90.9°
17.5°	60°	18.5°	59.1°
	75°	17.9°	76.3°
	90°	Test failure	
20°	60°	20.7°	55.9°
	75°	20.6°	73.8°
	90°	20.8°	89.0°
25°	60°	25.3°	59.4°
	75°	26.2°	73.7°
	90°	25.3°	89.3°

Scarab rover. The parameters k_σ and k for Scarab were identified from the slope-ascent experiment results.

Sample model-predicted rover trajectories are shown in Figure 3.8 with the trajectories observed in the experiments. While some level of errors exist, the predicted trajectories are close to the ones observed in the experiments. One of the sources of the errors lies in the steady state assumption for estimating the trajectories. The actual wheel slippage and sinkage develop over time and approach their steady state conditions. That is, the actual wheel slip was lower than the predicted steady state values at the initial stage of the motion, resulting in the gaps between the two corresponding trajectories.

The prediction errors in the final rover position are computed for each case, and the averages over the same slopes are listed in Table 3.3. One noticeable thing is that the errors are larger in the Y direction than in the X direction over all slopes. This can be also seen in Figure 3.8. Moreover, the predicted trajectories are all on the downhill side compared to the corresponding trajectories in the experiments. That is, the predictions are conservative and lie on the safe side. This is preferable to avoid risks of selecting wrong, non-ascendable vehicle headings.

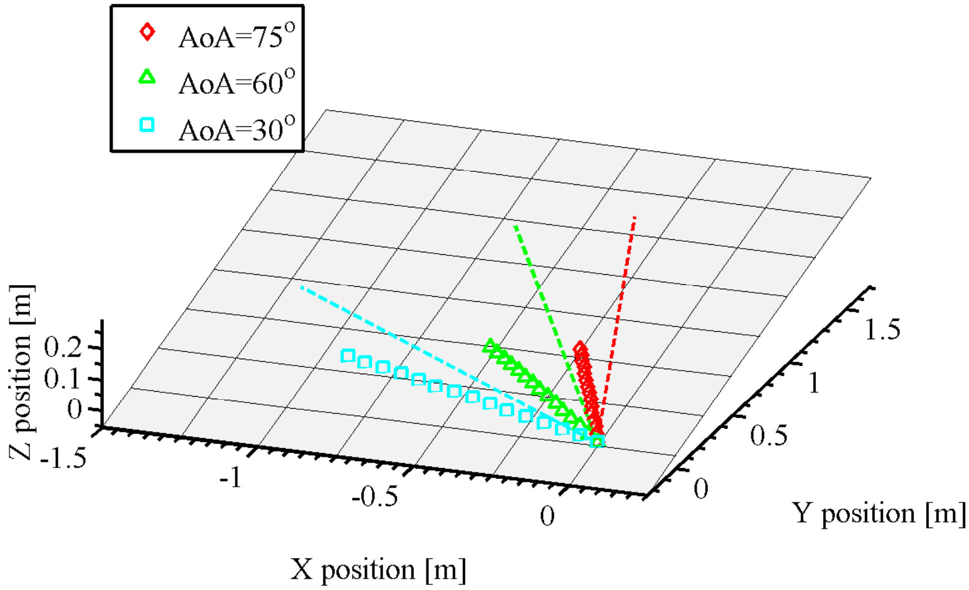

Figure 3.4: Rover trajectories on $\theta_0 = 10^o$ slope. The dashed lines represent the commanded trajectories and the markers show the actual trajectories during the experiments. The rover positions are plotted with an interval of 2 sec.

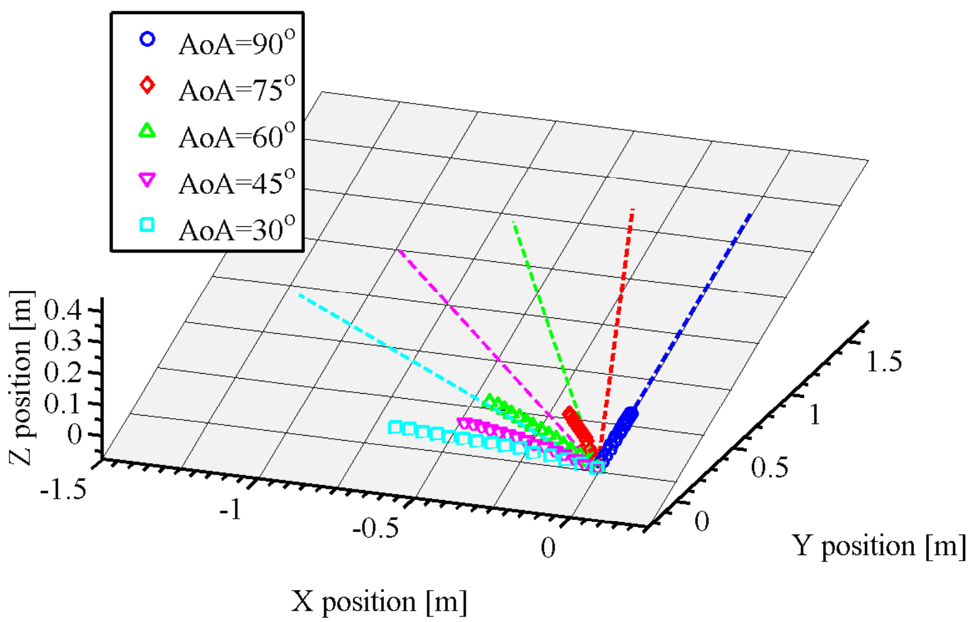

Figure 3.5: Rover trajectories on $\theta_0 = 15^o$ slope. The dashed lines represent the commanded trajectories and the markers show the actual trajectories during the experiments. The rover positions are plotted with an interval of 2 sec.

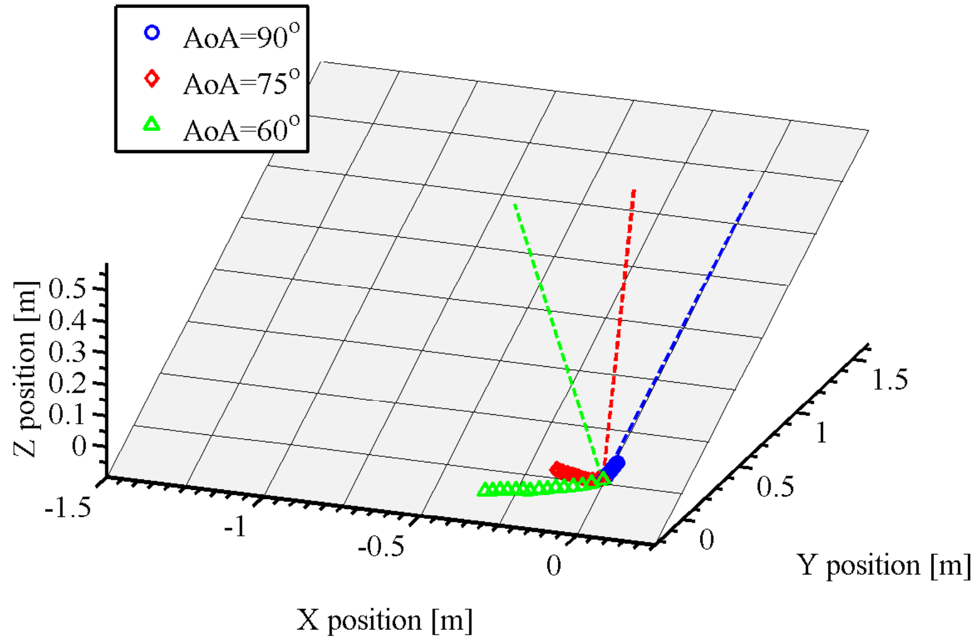

Figure 3.6: Rover trajectories on $\theta_0 = 20^o$ slope. The dashed lines represent the commanded trajectories and the markers show the actual trajectories during the experiments. The rover positions are plotted with an interval of 2 sec.

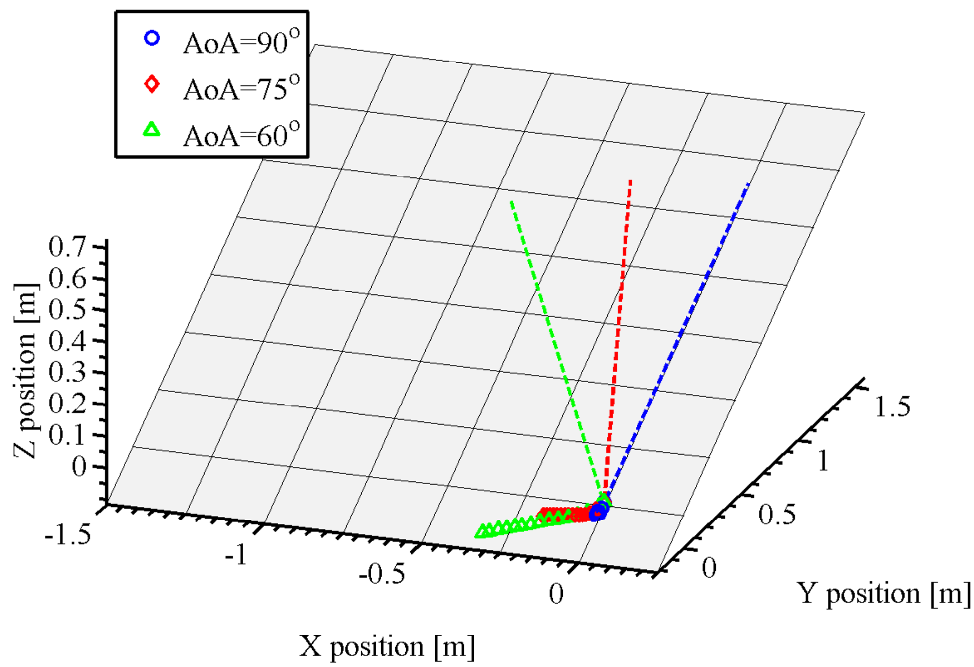

Figure 3.7: Rover trajectories on $\theta_0 = 25^o$ slope. The dashed lines represent the commanded trajectories and the markers show the actual trajectories during the experiments. The rover positions are plotted with an interval of 2 sec.

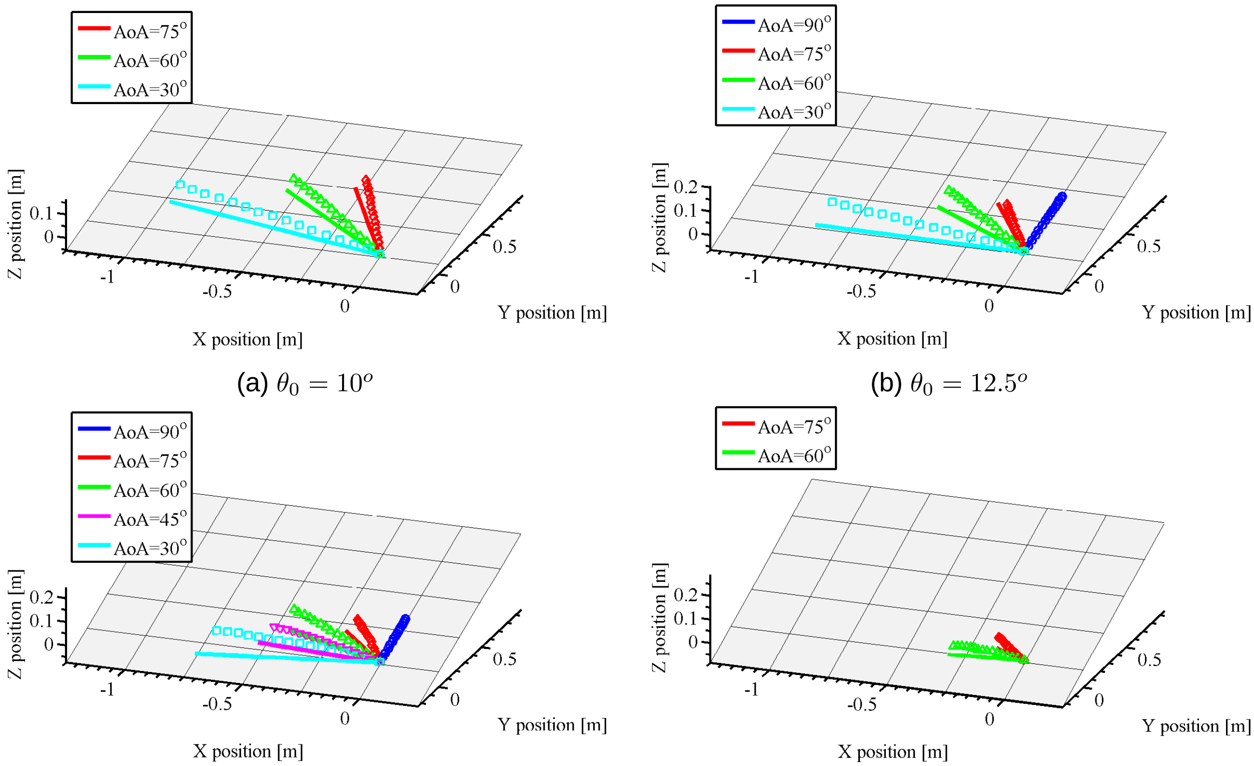

(a) $\theta_0 = 10^o$ (b) $\theta_0 = 12.5^o$

(c) $\theta_0 = 15^o$ (d) $\theta_0 = 17.5^o$

Figure 3.8: Comparisons of the rover trajectories from the simulations and experiments. The solid lines and markers represent the simulation and experiment trajectories, respectively.

Table 3.3: Average of the final position errors in the simulations.

Position error	Slope			
	10.0°	12.5°	15.0°	17.5°
X [m]	0.018	0.021	0.032	0.013
Y [m]	0.109	0.105	0.119	0.061
Total [m]	0.111	0.113	0.124	0.062

3.4.2 Rover slippage, uphill velocity, and efficiency

The slip ratio, slip angle, uphill velocity, and climb efficiency estimated from the experiments are plotted in Figures 3.9–3.12 together with those predicted based on the analytical model. As shown in Figure 3.9, the measured slip ratio basically decreases with the reduction of the angle of attack. The model-predictive curves of the slip ratio show a good agreement with this experimental trend.

The slip angle predicted from the model also captures the tendencies observed in the experiments as seen in Figure 3.10. When the angle of attack decreases from 90^o, the slip angle drastically increases and it turns to gradual reductions as the angle of attack further decreases. Notice that the predicted slip angle is tend to be larger than that observed in the experiments. This resulted in the larger position errors in the trajectory predictions mentioned in the previous section. Again, the overestimate of the slip means the prediction is on the safe side, and the rover actually could generate the lateral force larger than predicted. In addition, while some large deviations from the experiment values exist at around 75^o angle of attack on 20^o slope, this prediction error is not necessarily critical. This is because the predicted slip angel reached 90^o indicating that the rover cannot ascend the slope at the angle of attack. In fact, that slope is around the mobility limit for the configuration of the Scarab used in the experiment, and the slip ratio of the rover reached close to 1.0 as shown in Figure 3.9.

The predicted curves of the uphill velocity and climbing efficiency also agrees with the trends seen in the experiments as shown in Figures 3.11 and 3.12. Most of the trends of these mobility curves of the tested rover are similar to those of the Andy 2 described in Section 2.3. One of the major differences is that the Scarab's velocity and efficiency curves show no clear peak at angles smaller than 90^o. This indicates that direct slope ascent is the most preferable option for the tested configuration to ascent slopes, in terms of the velocity and power efficiency. This mobility difference between the two rovers is further discussed in the next section.

Overall, the model-based predictions agree with the experimental results. Also, while there exist gaps between the predicted and experimentally observed slip angle, the prediction is on safe side. This fact validates the utility of the slope-ascent model.

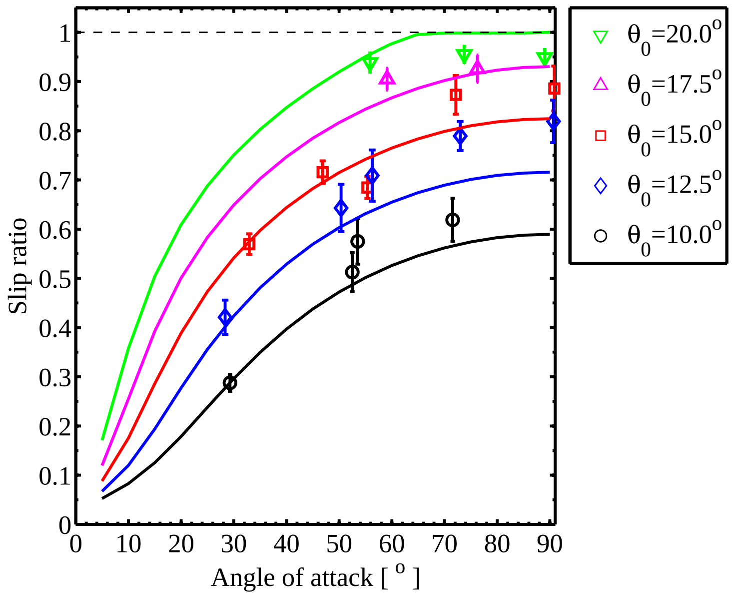

Figure 3.9: Slip ratio vs angle of attack relationship of the Scarab for different slopes θ_0. The markers represent the average slip ratio measured during the experiments whereas the error bars represent the 1-standard deviations. The model predictions are plotted with the solid curves.

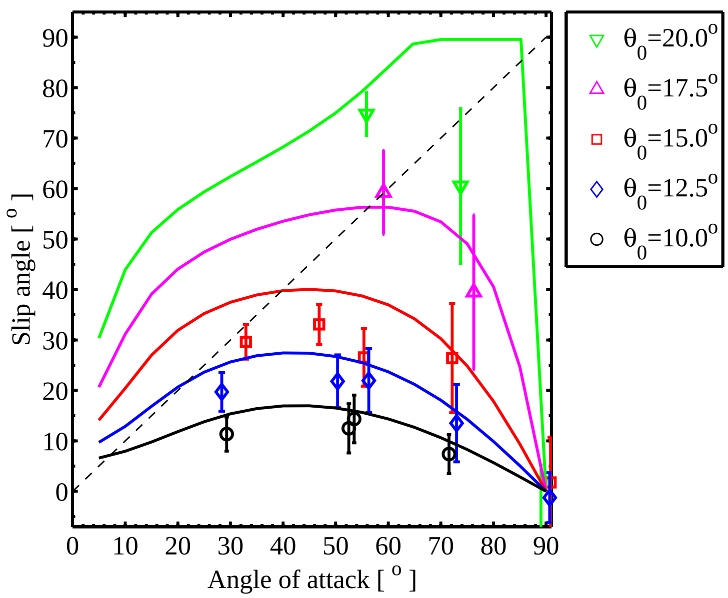

Figure 3.10: Slip angle vs angle of attack relationship of the Scarab for different slopes θ_0. The markers represent the averages measured during the experiments whereas the error bars represent the 1-standard deviations. The model predictions are plotted with the solid curves.

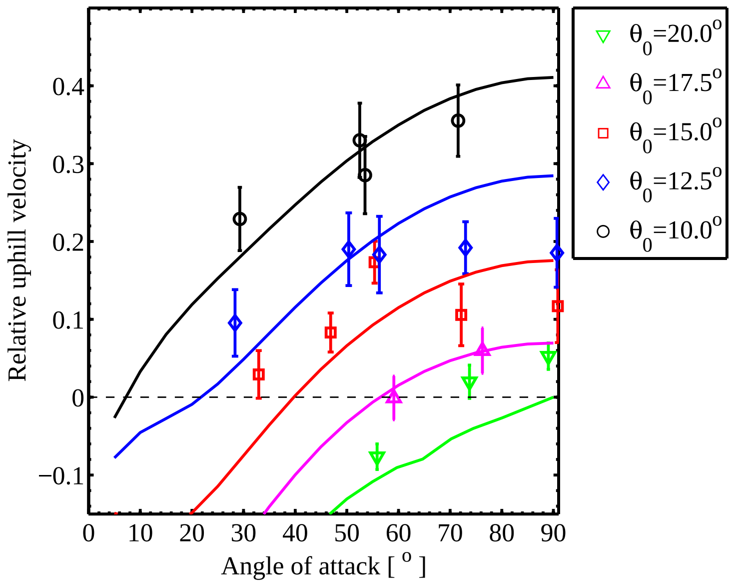

Figure 3.11: Uphill velocity vs angle of attack relationship of the Scarab for different slopes θ_0. The markers represent the average velocity during the experiments whereas the error bars represent the 1-standard deviations. The model predictions are plotted with the solid curves.

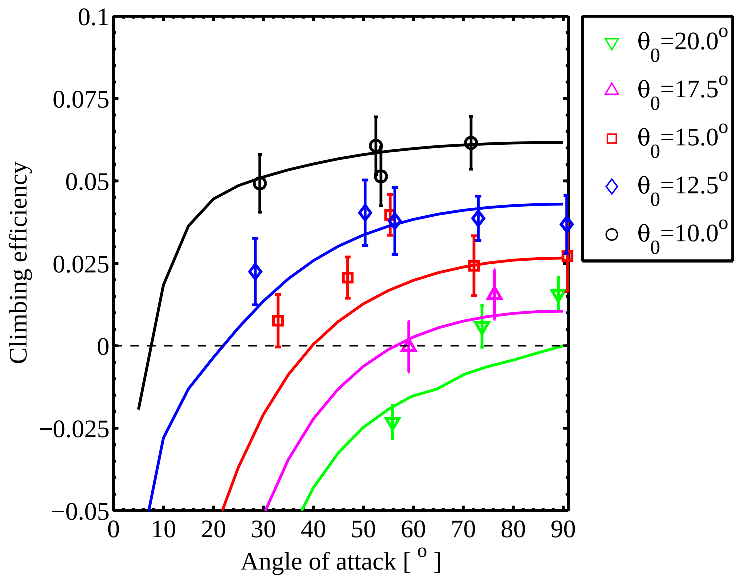

Figure 3.12: Climbing efficiency vs angle of attack relationship of the Scarab for different slopes θ_0. The markers represent the average efficiency during the experiments whereas the error bars represent the 1-standard deviations. The model predictions are plotted with the solid curves.

3.4.3 Comparison of slope-ascent performance of Andy 2 and Scarab

Figure 3.13 compares the four mobility criteria of Andy 2 and Scarab. As mentioned in the previous section, Scarab rover does not clearly show peaks of the uphill velocity and climbing efficiency at any angle of attack smaller than 90^o unlike Andy 2 does. The velocity and efficiency is determined by the balance of the longitudinal and lateral slip. By comparisons of slip angle curves of Andy 2, it can be seen how rapidly the lateral slip of the Scarab rover increases when the angle of attack is changed from 90^o. Because of this rapid increase of the lateral slip, diagonal ascent is less effective, for Scarab in the tested configuration, compared to direct ascent when ascending steep slopes.

From these observations, it can be concluded that whether diagonal slope-ascent provides an advantage over direct ascent is dependent on the mobility of a rover. Especially, the level of the lateral slip significantly affects the diagonal-ascent performance of the rover. Moreover, the reduction of the lateral slip is an important factor for shallower angles of attack to be beneficial to ascend steep slopes. Although the target of this research is limited to the nominal rover configuration, this is the reason why the active posture controls show great slope-ascent capability with small angles of attack [19]; A rover can significantly reduce the lateral slip on slopes when its body and wheels are leaned to the slope. The active posturing can reduce downhill sideslip because it can modify the wheel–soil contact condition and reduce the lateral gravitational resistance, which is the main cause of the sideslip on slope [45].

Another possible approach to reduce the downhill sideslip is to mount tall grousers on wheels. Taller grousers can interact with deeper portions of soil where soil show stronger bearing and shearing capability. This is why some angles of attack smaller than 90^o have possible advantage for the Andy 2 rover to ascend steep slopes unlike the tested Scarab configuration which has no grouser on its wheels. Appendix B discusses the importance of wheel grousers to reduce sideslip.

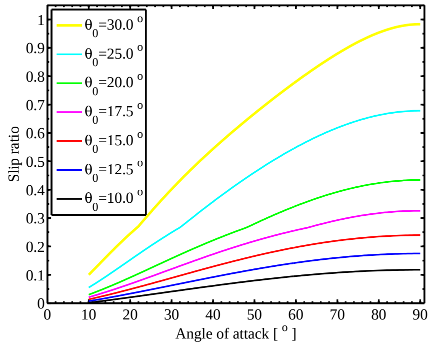

(a) Slip ratio (Andy 2)

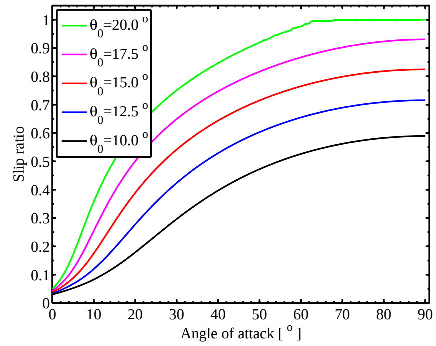

(b) Slip ratio (Scarab)

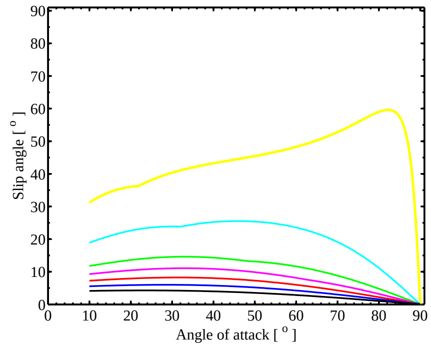

(c) Slip angle (Andy 2)

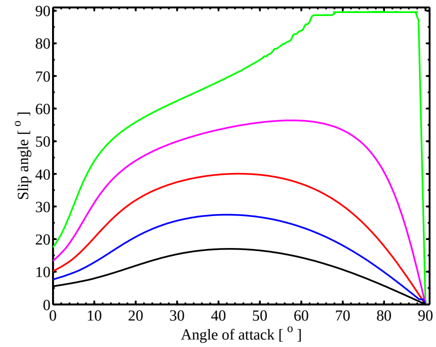

(d) Slip angle (Scarab)

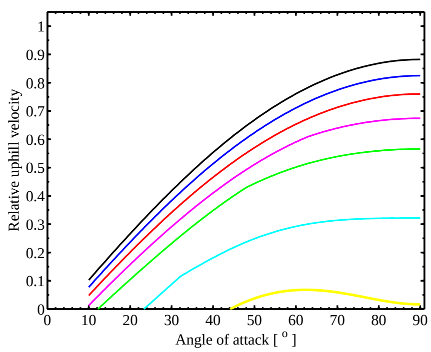

(e) Velocity (Andy 2)

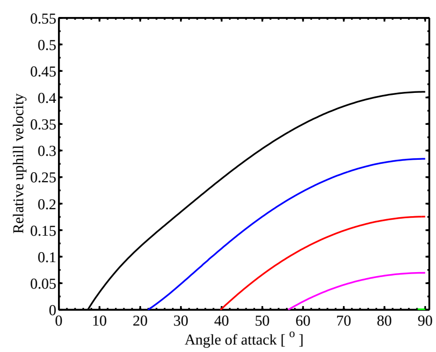

(f) Velocity (Scarab)

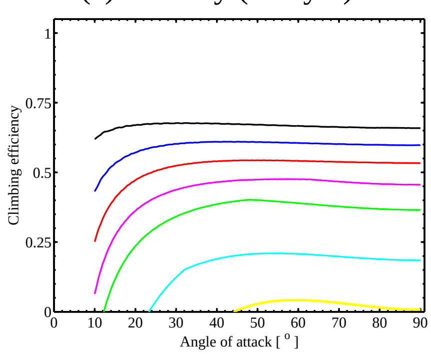

(g) Efficiency (Andy 2)

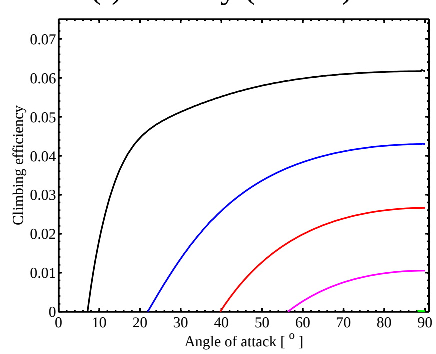

(h) Efficiency (Scarab)

Figure 3.13: Comparisons of the slope-ascent performances of Andy 2 and Scarab rovers.

3.5 Summary

Slope-ascent experiments were conducted using a four-wheeled rover, Scarab, on various angles of slope and at various angles of attack. The experiment results showed a good agreement with the qualitative trends shown in numerical simulations of the same rover. Quantitatively, there exist gaps between the predicted slip and that observed in the experiments; however, the predicted rover motions are conservative compared to the actual rover motion. That is, the model can avoid erroneously selecting routes that are actually not capable of ascending slope. These facts support the validity of the model-based analysis of the influence of the angle of attack and the utility of the model for the application to motion planning.

Besides, based on the comparison of the slope-ascent capability of Andy 2 and Scarab rovers, it can conclude that whether diagonal ascent can provide better slope-ascent performance than direct ascent is highly depending on the mobility of the rover itself. The diagonal ascent performance can be improved by increasing the lateral force, or grip, of the rover against sideslip. That can be accomplished by employing appropriate locomotion design or by providing additional degrees of freedom for reposturing the vehicle.

Chapter 4

Selection of Safe and Efficient Routes

This chapter presents a strategy to select a route for efficiently ascending slope. The strategy is introduced and described in Section 4.1. Then the slope trafficability characteristics of rovers is assessed in Section 4.2 to implement the strategy. In Section 4.3 the utility of the proposed strategy is demonstrated by simulations.

4.1 Route selection based on slip regulation and efficiency maximization

According to the analysis in the previous chapters, a large angle of attack, such as 90^o, may be an effective option to ascend slopes because of their shortest travel distance, and relatively faster and higher efficient motion. However large angles of attack have inherent higher longitudinal slip and thus higher risks of immobilization. In a slope-ascent case, even if a rover slippage reaches 100% and the rover has no uphill progress, it can escape from the high slip situation by just driving backward downhill. However it requires substantial recovery effort and an additional operation time and energy. Hence it is preferable to avoid that situation in advance by carefully selecting routes. Shallower angles of attack, on the other hand, can achieve lower wheel slip and power at expense of speed and gross energy. Though, larger downhill skid possibly causes huge localization errors and potential collisions with obstacles. Therefore everything is trade-off among safety, distance, time, and power efficiency.

One common solution is creating a cost function as a weighted sum of these metrics and derive a route that minimizes the total required cost [46]. These weighting factors can be allocated to each metric depending on the user's preferences or the mission scenarios. The resulting paths depends on how the weights are assigned to each metric. For example, providing a larger weight on safety can result in a safer but longer, energy-inefficient path. Preferable paths can be generated by defining the weights depending on what they care about. However, it is not easy to reasonably decide the weights, and the difficulty increases as the number of the incorporated evaluation criteria increases. A best weight combination may be able to find by varying the all weights and by comparing the resultant paths [47].

In this research, rather than using a cost function of various metrics, a route selection strategy is proposed, in which a slip threshold is utilized to regulate the vehicle longitudinal slip, and a route, or angle of attack to slope, is decided by maximizing the climbing efficiency under the slip regulation. The route selecting is expressed as a simple constrained optimization problem as follows:

$$\begin{aligned} \alpha^* = \arg\max_{\alpha} \eta_Y(\alpha, s) \\ \text{subject to} \quad s \leq s_{th} \end{aligned} \tag{4.1}$$

where α^* denotes the selected angle of attack, s is the slip ratio, s_{th} is the threshold slip, and η_Y is the climbing efficiency estimated from Eq. (2.38) or (2.40).

The climbing efficiency is selected for the single metric cost function since the parameter can represent and include the all aspects of travel time, distance, and total energy consumption as discussed in Section 2.3.4, i.e. higher climbing efficiency means relatively shorter travel time, shorter distance, and lower energy consumption. This kind of energy-related metric is preferable since it can also reflect the roughness of the terrain (more energy required for traveling rocky or bumpy terrains) in addition to the path length [9, 31] although this research assumes terrains of smooth surfaces.

The idea of the slip threshold is introduced because it enables users to directly and more effectively limit the level of the vehicle slippage than implicitly regulating the slip by incorporating it into a cost function and minimizing it. The threshold level can be chosen depending on the mission scenario and situation. For example, 20% slip is considered as one of the effective threshold levels. Typically, vehicle slip develops gently at slip lower than 20–30%. However, it rises rapidly over the slip level. In another perspective, wheels can achieve highest tractive efficiency, which is defined as the power efficiency in the vehicle's longitudinal direction, at around 10–30% slip. Therefore 20% slip can be thought as a safe and efficient travel condition. Another threshold level to take may be 60% slip at which the drivers need to care about the vehicle slip. Over 80% can be considered as a dangerous slip level, and 95% slip is the slip level where the longitudinal progress of the motion is almost zero and at the highest risk of immobilization.

4.2 Assessment of slope trafficability characteristics

Before implement the proposed strategy, slope trafficability of rovers are assessed in this section to understand the overall characteristics of the metrics involved in the problem.

4.2.1 Slope trafficability diagram

Figure 4.1 shows the trafficability characteristics of Andy 2 and Scarab over various slopes. The term trafficability refers to a capability of a vehicle to climb or traverse a specific type of terrain without losing its traction [26]. In the slope trafficability diagram, contours of slip ratio (Eq. (2.6)) and climbing efficiency (Eq. (2.38)) are mapped into the θ_0–α space. The solid black curves represent the boundary for the angle of attack whether the slope is ascendable or not. The angles of attack outside of this boundary indicates that the rover cannot ascend the slope either due to large longitudinal or lateral slip. Notice that the maximum angle of attack is clipped to 90^o as the angle between $0^o \leq \alpha \leq 90^o$ results in the same performance as the angle $180^o - \alpha$.

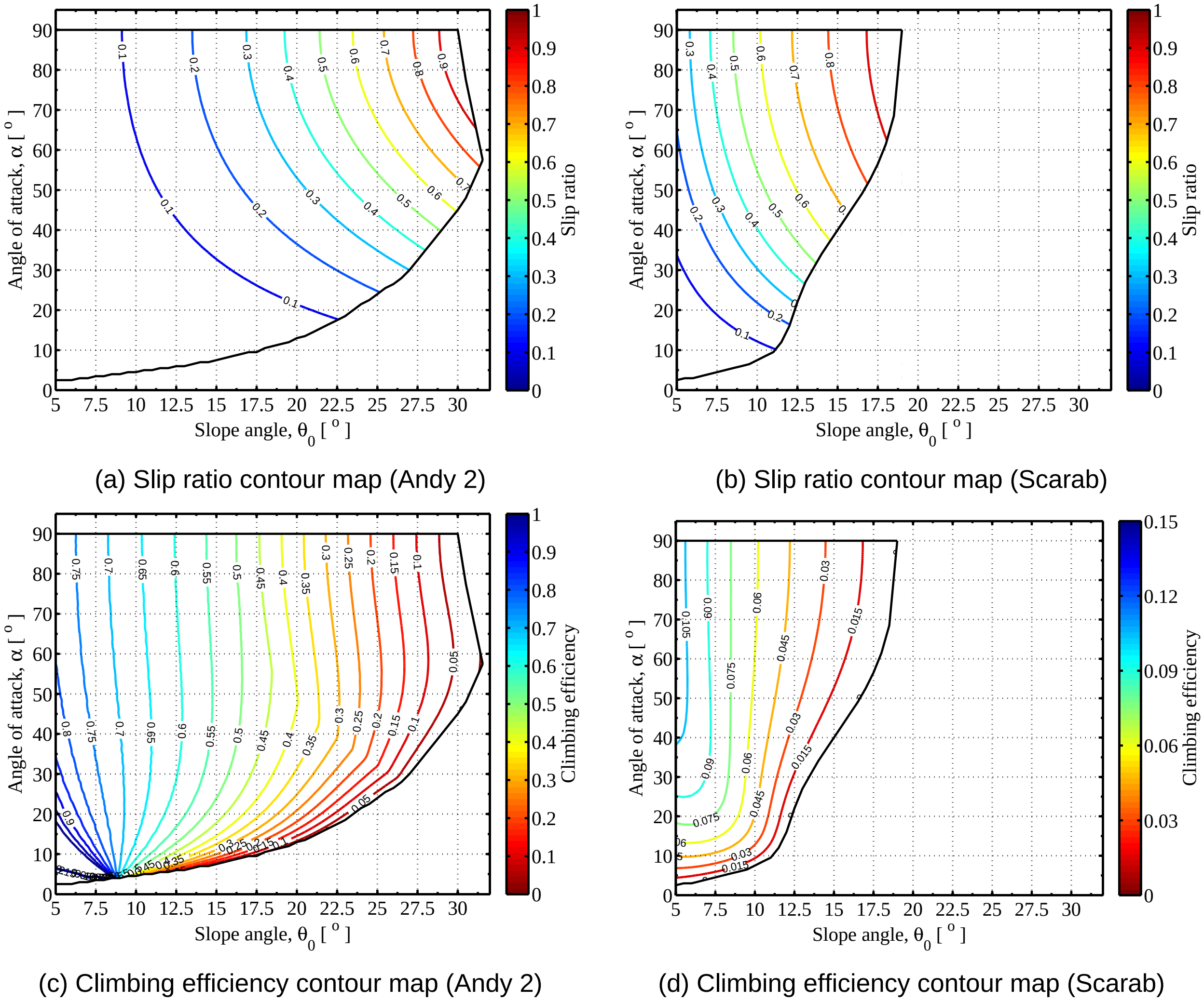

(a) Slip ratio contour map (Andy 2)

(b) Slip ratio contour map (Scarab)

(c) Climbing efficiency contour map (Andy 2)

(d) Climbing efficiency contour map (Scarab)

Figure 4.1: Slope trafficability diagram of Andy 2 and Scarab rovers. Contours of the slip ratio and climbing efficiency are projected into the θ_0–α space. The solid black curves represent the boundary of the slope-ascendable angle of attack. The angle of attack outside this boundary cannot ascend the corresponding slope.

The trafficability diagrams indicate how Andy 2 and Scarab perform differently on a same slope and at a same angle of attack. The area of the accessible/assendable slopes is smaller for Scarab (with the tested configuration) compared to Andy 2. The steepest slope ascendable with 90^o angle of attack is around 30^o for Andy 2 whereas it is around 18^o for Scarab. The diagram also insists that Andy 2 cannot ascend slopes over 30^o with the 90^o angle direct ascent. However the rover can diagonally ascent slopes up to around 31.5^o with some range of angles of attack. On the other hand, Scarab cannot diagonally climb up the slopes where the 90^o angle of attack fails.

The slip ratio contours shown in Figure 4.1 (a) and (b) represent the threshold slip levels for Andy 2 and Scarab, respectively. From the slip ratio contours, the slopes ascendable with each threshold slip can be looked up along with the corresponding angle of attack to achieve that ascent motion. For example, Andy 2 can ascend slopes up to about 25^o with slip ratio of 0.2 or lower by appropriately selecting the angle of attack whereas the steepest slope ascendable with the same slip regulation is about 12^o for Scarab rover.

Figure 4.1 (c) and (d) shows the climbing efficiency contours for Andy 2 and Scarab, respectively. The contour maps show how the power efficiency for the slope-ascent varies when the angle of attack changes. As depicted in the figures, the change in the climbing efficiency is more sensitive in the change in the slope angle than the angle of attack, especially at large angle of attack. The efficiency contours also become denser as the angle of attack gets smaller than about 30–40^o, indicating rapid drop off of the efficiency. The efficiency contour map is informative to comprehend the efficiency variation when selecting the angle of attack with the slip ratio contour map.

4.2.2 Climbing efficiency diagram

While the trafficability diagram is informative to understand the slope-ascent performance of a rover in the entire $\theta_0 - \alpha$ space, the trafficability characteristics can be more intuitively understood if the rover trafficability is visualized for a target slope. From this motivation, another type of chart, namely Climbing Efficiency Diagram (CED) is proposed here. An example CED for Andy 2 rover is shown in Figure 4.2. The CED is basically twofold: (1) the angle of attack–climbing efficiency characteristic curve and (2) the superimposed slip ratio thresholds for the given slope. The diagram indicates comprehensive trafficability of the rover at various angles of attack over the corresponding terrain, showing the climbing efficiency, slope ascendability, and slip ratio.

First, the diagram provides the information of how the efficiency changes along with the angle of attack. As shown in Figure 4.2 the climbing efficiency gently increases when the angle of attack reduces from 90^o, it reaches the highest value and then it drops down as the angle of attack gets further smaller.

Secondly, the diagram indicates the minimum feasible angle of attack to ascend the slope. According to Figure 4.2, the angle of attack smaller than 12.5° cannot climb up the slope since the climbing efficiency becomes negative.

At last, the CED also shows the variations of the slip ratio for different angles of attack. More specifically, it can be noticed from the diagram that the slip ratio is $0.1 \leq s$ at the angle of attack between $0^\circ \leq \alpha \leq 21.4^\circ$, and the slip is $0.1 < s \leq 0.2$ at $21.4^\circ < \alpha \leq 36.5^\circ$, and so force. The

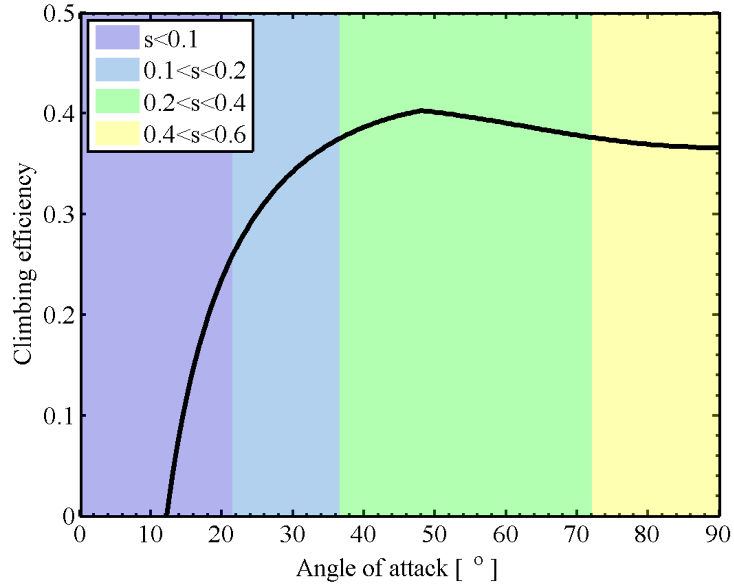

Figure 4.2: Climbing efficiency diagram of Andy 2 for 20^o slope. Multi-levels of slip threshold are rendered with different colors. The diagram indicates climbing efficiency, slope-ascendability, and slip levels for various angles of attack.

width of the slip ratio band to show can be arbitrarily set depending on how much details of the slip variation needs to be known.

From these three features, a preferable rover heading can be found by setting an appropriate slip threshold level and then by maximizing the climbing efficiency of the motion under the regulation.

4.3 Simulation of route selection

In this section, the strategy to select a route using the Climbing Efficiency Diagram is demonstrated through a series of slope-ascent simulations. Routes for Andy 2 and Scarab are derived for different terrain situations.

Andy 2 over 20^o slope

Figure 4.3 (a) shows the CED for Andy 2 on 20^o slope. Here two slip threshold levels, $s_{th} = 0.2$ and $s_{th} = 0.6$, were set. Then, the angles of attack that maximize the climbing efficiency under these constraints were found: 36.5^o and 48.0^o, respectively. The corresponding trajectories with these headings are visualized in Figure 4.3 (b) with the magenta and red markers, respectively. Similar to the simulation in Section 2.3.3, the goal was set to the line 3 m uphill, and the rover reference velocity was set to 5 cm/s. In the figure, the motion with the 90^o angle of attack is also depicted with the blue markers as a reference. Table 4.1 summarizes the results of the simulation. Under the threshold of $s_{th} = 0.2$, the rover achieved -24.8% lower slip ratio compared to the route of $s_{th} = 0.6$ while it took +38.8% longer time and consumed 7.4% more energy totally. On the other hand, the 90^o angle of attack route required 24.1% shorter time than the route of $s_{th} = 0.6$, but the rover slipped 63.2% more and consumed 10% more energy with regard to the $s_{th} = 0.6$ route.

Andy 2 over 25^o slope

The CED for 25^o slope is shown in Figure 4.4 (a). The same slip constraints, $s_{th} = 0.2$ and $s_{th} = 0.6$, were applied in the route selection stage. The corresponding routes that attain the maximum climbing efficiency under these constraints are $\alpha = 24.7^o$ and $\alpha = 55.0^o$, respectively. As seen in the simulated trajectories shown in Figure 4.4 (b), the route with $s_{th} = 0.2$ is not preferable because of the long, shallow trajectory and the substantial time required to reach the goal line. It also requires 571.9% more energy relative to the route with the threshold of $s_{th} = 0.6$ according to Table 4.2. The $\alpha = 55.0^o$ route ($s_{th} = 0.6$) could ascend the slope with 25% lower slip and 11.9% less energy with respect to the direct ascent although the travel distance was almost double.

Andy 2 over 31^o slope

This slope is around the limit of the trafficability of Andy 2 rover as seen in Figure 4.1 (a). On this slope, the rover can no longer drive directly up the slope at 90^o angle of attack, but it can ascend with some smaller angles. The slope-ascendable angle of attack is very limited and rages from about 51.5^o to about 69.5^o as depicted in Figure 4.5 (a). In addition, it can be inferred from the figure that the rover will experience very high level of slip at those angles of attack; the lowest slip is 0.73 at 51.5^o. As the target terrain is so challenging that the rover cannot ascend directly and that significantly high slip is inevitable at any angle of attack, the goal of this scenario is to derive a route which can efficiently rescue the rover from the terrain by taking the risk of high slip.

From the above observation, two slip thresholds, $s_{th} = 0.8$ and $s_{th} = 0.95$, were set. Selected angles of attack for these slip constraints were $\alpha = 57.3^o$ and $\alpha = 59.0^o$, respectively. Figure 4.5 (b) visualizes the executed motions of the rover at these angles of attack. Notice that the rover did not make any forward progress at all with $\alpha = 90^o$ as mentioned. The two routes that correspond to slip thresholds of $s_{th} = 0.8$ and $s_{th} = 0.95$ are very close to each other, but the latter route could ascend the slope with 9.2% shorter time and 6.2% less energy consumption compared to the former by increasing the slip ratio by 2.0%. The simulation results are summarized in Table 4.3.

Although the rover can still ascend the slope diagonally, it requires very long transverse distance to reach the goal line due to the large lateral slip. The actual angles of motion are just approximately 3^o off from the base of the slope. Therefore, the benefit of the diagonal slope-ascent will be only available in the case where that long cross-slope exists such as craters of large diameter. One might think the rover can climb up the slope with shorter transverse width by selecting a switchback path in which the rover repeats ascending the slope at an angle and point-turning after traveling some distance. This approach is not always feasible since steering or point-turning on steep slopes cause a substantial amount of downhill skid. That is, the rover will highly possibly make no gross uphill progress in loose media due to large downhill skid during point-turning.

Scarab over 15^o slope

15^o slope is a difficult terrain for Scarab rover as it is relatively close to the trafficability limit of the rover as seen in Figure 4.1. Figure 4.6 (a) shows the CED for Scarab on the slope. Unlike Andy 2, no peak efficiency exists below the 90^o angle of attack. As the slip ratio becomes more than 0.6 for the slope-ascendable angles of attack, the slip regulation is set to $s_{th} = 0.8$ and $s_{th} = 0.95$ here again. The corresponding angles of attack are $\alpha = 70.5^o$ and $\alpha = 90^o$, respectively. The simulation results of these angles are illustrated in Figure 4.6 and summarized in Table 4.4. The direct ascent route got 3.2% higher slip ratio, with respect to the route derived under the lower slip threshold, however, it can ascend with 11% shorter time, 33% shorter distance, and 6.6% less energy consumption. Therefore, for Scarab, the direct ascent is a preferable solution for this terrain.

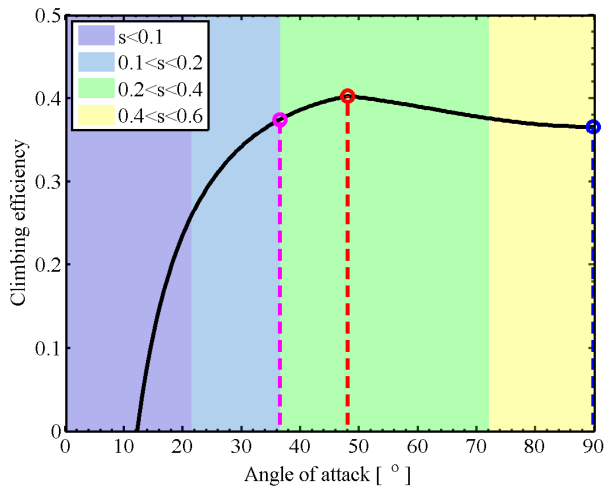

(a) Climbing efficiency diagram

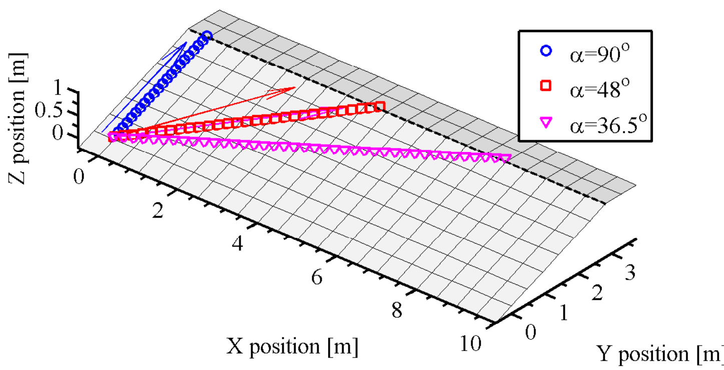

(b) Predicted trajectories. The rover positions are plotted with an interval of 5 sec.

Figure 4.3: Route selection for Andy 2 over 20^o slope. $\alpha = 36.5^o$ and $\alpha = 48.0^o$ correspond to the routes which achieve the maximum efficiency under the slip threshold of $s_{th} = 0.2$ and $s_{th} = 0.6$, respectively. The arrows in (b) represent the target headings that correspond to the selected angles of attack.

Table 4.1: Slope-ascent simulation results of Andy 2 on 20° slope. For each angle of attack (α), the corresponding travel time (t), travel distance (d), slip ratio (s), slip angle (β), uphill velocity (v_Y), climbing efficiency (η_Y), and energy consumption (E) are listed.

α [°]	t [s]	d [m]	s	β [°]	v_Y [cm/s]	η_Y	E [kJ]
90.0	106.1	3.0	0.434	0.0	2.83	0.365	0.74
48.0	139.8	5.3	0.266	13.3	2.15	0.402	0.68
36.5	194.0	8.0	0.200	14.5	1.55	0.374	0.73

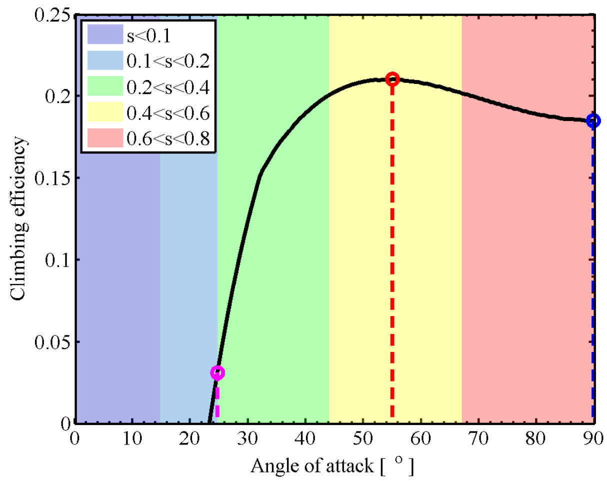

(a) Climbing efficiency diagram

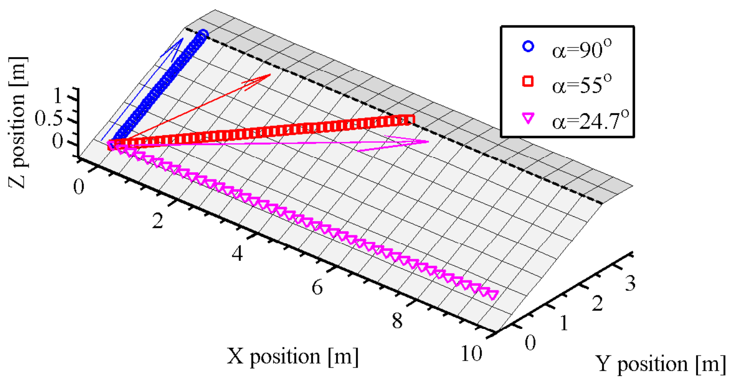

(b) Predicted trajectories. The rover positions are plotted with an interval of 5 sec.

Figure 4.4: Route selection for Andy 2 over 25^o slope. $\alpha = 24.7^o$ and $\alpha = 55.0^o$ correspond to the routes which achieve the maximum efficiency under the slip threshold of $s_{th} = 0.2$ and $s_{th} = 0.6$, respectively. The arrows in (b) represent the target headings corresponding to the selected angles of attack.

Table 4.2: Slope-ascent simulation results of Andy 2 on 25° slope.

α [°]	t [s]	d [m]	s	β [°]	v_Y [cm/s]	η_Y	E [kJ]
90.0	186.6	3.0	0.678	0.0	1.61	0.185	1.82
55.0	219.4	6.0	0.507	24.7	1.37	0.210	1.60
24.7	3331.8	145.4	0.200	23.5	0.09	0.031	10.75

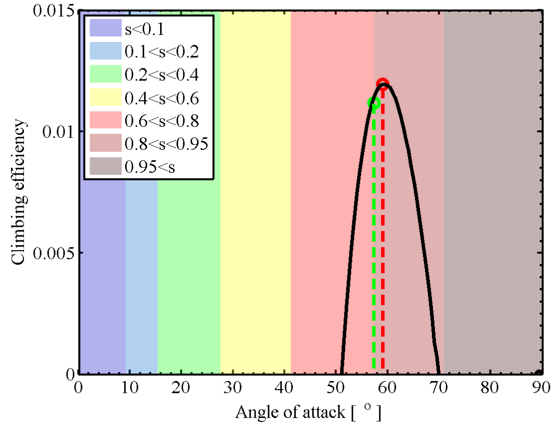

(a) Climbing efficiency diagram

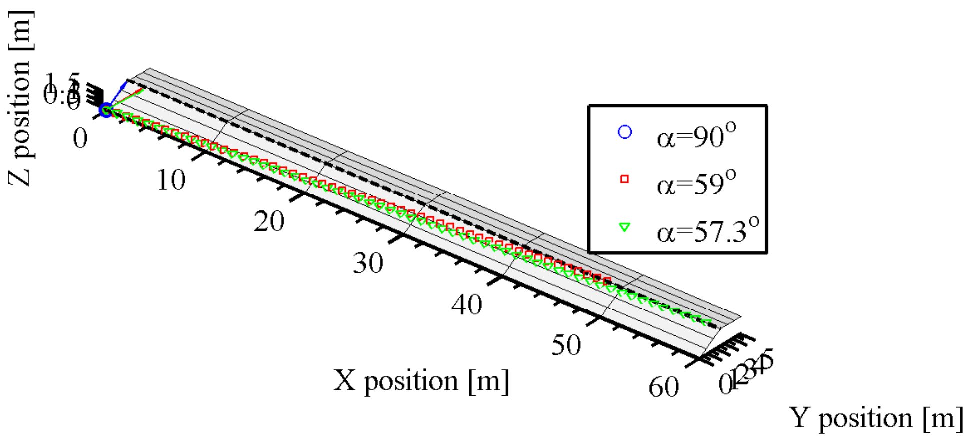

(b) Predicted trajectories plotted with an interval of 60 sec

Figure 4.5: Route selection for Andy 2 over 31^o slope where 90^o angle of attack ascent can no longer make an uphill progress. $\alpha = 59^o$ and $\alpha = 57.3^o$ correspond to the angles of attack which obtains the maximum efficiency under the constraints of $s_{th} = 0.80$ and $s_{th} = 0.95$, respectively.

Table 4.3: Slope-ascent simulation results of Andy 2 on 31° slope.

α [°]	t [s]	d [m]	s	β [°]	v_Y [cm/s]	η_Y	E [kJ]
90.0	—	—	1.000	0.0	0.0	—	—
59.0	3115.6	49.6	0.820	55.5	0.096	0.01193	34.31
57.3	3431.4	58.8	0.800	54.4	0.087	0.01117	36.61

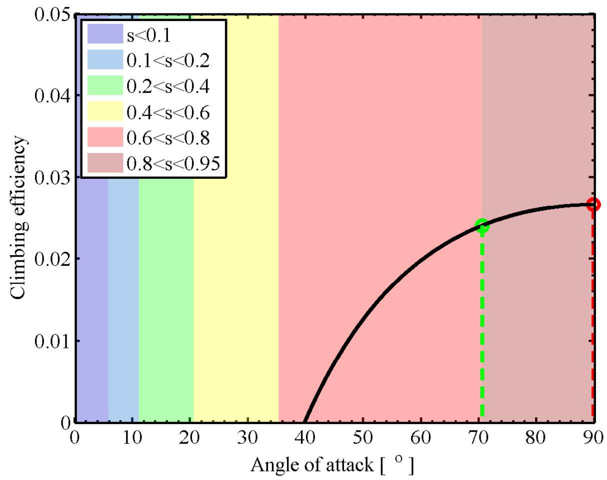

(a) Climbing efficiency diagram

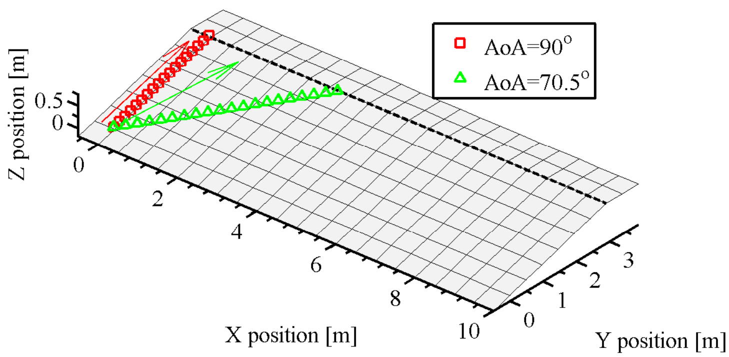

(b) Predicted trajectories. The rover positions are plotted with an interval of 10 sec.

Figure 4.6: Route selection for Scarab over 15^o slope. $\alpha = 70.5^o$ and $\alpha = 90^o$ correspond to the routes which achieve the maximum efficiency under the slip threshold of $s_{th} = 0.8$ and $s_{th} = 0.95$, respectively. The arrows in (b) represent the target headings that correspond to the selected angles of attack.

Table 4.4: Slope-ascent simulation results of Scarab on 15° slope. For each angle of attack (α), the corresponding elapsed time (t), travel distance (d), slip ratio (s), slip angle (β), uphill velocity (v_Y), climbing efficiency (η_Y), and energy consumption (E) are listed.

α [°]	t [s]	d [m]	s	β [°]	v_Y [cm/s]	η_Y	E [kJ]
90.0	342.8	3.0	0.875	0.0	0.088	0.0255	59.70
70.5	388.5	4.5	0.800	28.6	0.772	0.0238	63.90

4.4 Summary

In this chapter, a route selection strategy was proposed for an efficient and successful slope-ascent. The route selection is made by regulating the vehicle longitudinal slip with a slip threshold and by maximizing the power efficiency to ascend the slope under the slip regulation. The proposed method derives an effective slope-ascending route with a user-defined slip level and relatively short travel time, short distance, and less energy consumption.

In addition, two types of diagrams to assess the slope-trafficability of a rover were introduced: slope trafficability diagram and climbing efficiency diagram. Both of them are informative to comprehend tractive performance of a rover over sloped terrain and to derive an effective path to overcome a target slope. The climbing efficiency diagram was applied to the proposed route selection strategy, and its usefulness was shown in numerical simulations.

Moreover, the trafficability analysis showed that the the steepest slope which can be directly ascended is around 30^o for Andy 2 and around 18^o for Scarab. Andy 2 can climb slopes up to 31.5^o by a diagonal ascent with shallower angles of attack whereas Scarab cannot diagonally ascent slopes where direct ascent fails. One noticeable thing, however, is that while Andy 2 can diagonally ascend such steep slopes, it requires long transverse trails to overcome the slopes due to large downhill skid. Ascending crater walls is a possible situation in which the diagonal ascent will achieve successful slope climbing.

Chapter 5

Conclusion

5.1 Summary and conclusion

This thesis addressed the problem of finding efficient routes to ascend slopes of deformable material. To this end, the influence of the angle of attack on the slope-ascent performance of rovers was investigated. The analysis was made based on the slope-ascent model and actual rover experiments.

Slope-ascent rover model was developed based on a steady state slope-ascent condition and terramechanics-based wheel–soil interaction. Based on the model, rover longitudinal and lateral slip, uphill velocity, and climbing efficiency were predicted and associated with the angle of attack. The model-based analysis of the slope trafficability of Andy 2 rover showed the following trends: when the angle of attack is reduced from 90^o, on most of slopes

1. The longitudinal slip monotonically reduces.
2. The lateral slip rapidly rises at first and then it gently decreases or plateaus.
3. The uphill velocity decreases.
4. The energy efficiency does not significantly change until a certain angle of attack, but it rapidly drops off after that.

Direct slope ascent is an effective option to ascend slope because of its shortest travel distance, and relatively faster and higher efficient motion. However large angles of attack have inherent higher longitudinal slip and higher risk of immobilization. On the other hand, a shallower angle of attack is preferable if the longitudinal slip is a critical factor since a small angle of attack can achieve lower longitudinal slip, but it requires longer travel time, longer transverse distance, and higher energy consumption. Also, on an extremely steep slope, a rover can no longer generate sufficient traction for direct ascent. In that case, diagonal slope ascent is the only viable option to overcome the terrain.

The slope-ascent experiments using a four-wheeled rover, Scarab, showed a good agreement with the qualitative trends of numerical simulations for the same rover. While there exist prediction errors between the model-predictive slip and those observed in the experiments, the predicted rover motions are conservative and on the safe side when compared to the actual rover motion. These results supported the validity of the model-based analysis and the utility of the model for the application to motion planning.

These analyses led to propose a strategy to select an efficient and successful route to overcome slope. The proposed route selection strategy consists of the slip regulation and the climbing efficiency maximization under the slip constraints. That enables a rover to explicitly regulate its longitudinal slip within the user-defined slip threshold and accomplish relatively short travel time, short distance, and less energy consumption. The route selection method was implemented with the climbing efficiency diagram, and demonstrated its usefulness in numerical simulations for different rovers and for various slopes.

5.2 Contribution

The one of the main contributions of this thesis is the detailed investigation of the influence of the angle of attack on slope-ascent performance of rovers. In spite of the importance of the problem, it had been an open question, and no detailed analysis of the effect of the angle of attack had been made before. This research revealed for the first time the relationship between the angle of attack and slope trafficability of rovers based on physics-based analysis and experimentation. The analysis showed that preferable routes to efficiently ascend terrain depends on the slope inclination and also depends rover mobility.

This research proposed a route selection strategy for overcoming challenging slopes. While tons of path planning algorithms have been proposed, non of them explicitly addresses the problem of the slope-ascent over deformable terrains where rovers will experience high slippage. This research developed a planning algorithm to find efficient slope-ascent routes for those types of terrains.

Another contribution made from the analysis is the clarification of the key factor to improve rovers' slope-ascent performance: reduction of the wheel sideslip. The sideslip on sloped terrain is mainly induced by the lateral gravitational resistance. If the wheel does not have the capability to generate large lateral force against the gravitational force, high sideslip is induced, resulting in a large deviation of the motion from a commanded trajectory. That makes diagonal slope-ascent less useful. The sideslip can be reduced by either increasing the lateral force which the wheel can generate or by eliminating the lateral gravity resistance. The former can be accomplished by employing tall grousers or side-caps on wheels that work as stoppers against the downhill slide. The latter can be made by actively controlling the roll of the rover. By making the body and wheels level on inclined terrain, the wheel–soil contact state can be changed such that the gravity resistance in the lateral direction disappears. In either way, the rover can reduce the downhill sideslip, and improve the diagonal ascent performance and the overall slope-trafficability.

The results of this thesis contribute to develop motion planning and control strategies of rovers and also to develop locomotion configurations and controls which can have high terrain-negotiation capability that can expand the area where rovers can access and discover more scientifically important and interesting findings on other astral bodies.

5.3 Future work

There are many possible directions of work to support and extend this research.

First and foremost, an experimental validation of the proposed route selection strategy is highly important. In this thesis, the strategy was only demonstrated in numerical simulations. A validation by experiments will strengthen the argue of this research and also will provide new findings and problems that cannot be encountered in simulations and also provide a chance to eventually improve the robustness of the planning system.

Second, it is also important to improve the slope-ascent model described in this thesis. While the single-wheel model can predict simple linear motions of rovers, the accuracy of the prediction should be improved by combining the wheel–soil interaction model with vehicle dynamics which is also applicable to many other motion planning and control problems. Learning-based approach, such as parametric or non-parametric regressions, is another possible way to model rover behaviors if training data of past experience of rovers is available. Moreover, the slip model used in this research is deterministic and does not take into account the model inaccuracy or uncertainty of the model parameters. On challenging terrain, such as a steep slope, only small prediction errors can jeopardize the entire mission or conversely restrict the potential rover performance. Adopting stochastic techniques [48, 49] is one possible solution to treat the model uncertainty.

Another prospective area of future research is incorporating the ideas developed in this research into a global/local path planner. The target of this research was quite specific to the problem of slope-ascent over deformable terrain. It is important to incorporate the analysis results and proposed strategy into more general path planners. An example solution is switching the planning policies depending on the target terrain or mission scenario: using a general planner for gentle terrain and selecting the proposed scheme for steep terrain.

In addition to the route selection, another key factor to successfully reach a goal is how to control the vehicle motion to follow the planned route. The path following can be made by either an open-loop feed-forward approach based on a model-predictive motion generation or a closed-loop feedback control which utilizes sensor-feedback to remedy path-tracking errors. The former approach can provide preferable motions in advance, but the control performance is sensitive to the model accuracy. On the other hand, the latter does not require fine models, but difficult to recover to the planned path if the initial given motion is inappropriate. A good way to improve the path-following performance is to combine both approaches; A model-predictive feed-forward controller generates a good initial motion whereas a feedback controller minimizes the path-tracking errors [9, 50]. The slope-ascent model and the model-based analysis made in the research are applicable to such motion controllers.

Bibliography

[1] NASA, *Lunar Reconnaissance Orbiter*,
URL: http://www.nasa.gov/mission_pages/LRO/main/index.html, Accessed August 1, 2015.

[2] E. Sefton-Nash, M.A. Siegler, and D.A. Paige, Thermal Extremes in Permanently Shadowed Regions at the Lunar South Pole, *Proceedings of the 44th Lunar and Planetary Science Conference*, March 2013.

[3] NASA, *Resource Prospector*,
URL: https://www.nasa.gov/resource-prospector, Accessed September 23, 2015.

[4] D. Andrews, A. Colaprete, J. Quinn, D. Chavers, and M. Picard, Introducing the Resource Prospector (RP) Mission, *Proceedings of the AIAA SPACE 2014 Conference and Exposition*, August, 2014.

[5] M.T. Zuber, J.W. Head, D.E. Smith, G.A. Neumann, E. Mazarico, M.H. Torrence, O. Aharonson, A.R. Tye, C.I. Fassett, M.A. Rosenburg, and H.J. Melosh, Constraints on the Volatile Distribution within Shackleton Crater at the Lunar South Pole, *Nature*, Vol.486, pp.378–381, 2012.

[6] C. Cunningham, H.L. Johns, J. Kay, K.M. Peterson, and W.L.R. Whittacker, Time-Dependent Planning for Resource Prospecting, *Proceedings of the 12th International Symposium on Artificial Intelligence, Robotics, and Automation in Space*, June, 2014.

[7] N.D. Otten, H.L. Johns, D.S. Wettergreen, and W.L. Whittacker, Planning Routes of Continuous Illumination and Traversable Slope using Connected Component Analysis, *Proceedings of the 2015 IEEE International Conference on Robotics and Automation*, May, 2015.

[8] J.L. Heldmann, A.C. Colaprete, R.C. Elphic, B. Bussey, A. McGovern, R. Beyer, D. Lees, M.C. Deans, N. Otten, H. Jones, and D. Wettergreen, Rover Traverse Planning to Support a Lunar Polar Volatiles Mission, *Abstracts of the 2015 Annual Meeting of the Lunar Exploration Analysis Group*, October, 2015.

[9] D. Helmick, A. Angelova, and L. Matthies, Terrain Adaptive Navigation for Planetary Rovers, *Journal of Field Robotics*, Vol.26, Issue 4, pp.391–410, 2009.

[10] D.M. Helmick, S.I. Roumeliotis, Y. Cheng, D.S. Clouse, M. Bajracharya, and L.H. Matthies, Slip-Compensated Path Following for Planetary Exploration Rovers, *Advanced Robotics*, Vol.20, No.11, pp.1257–1280, 2006.

[11] S. Karumanchi, T. Allen, T. Bailey, and S. Scheding, Non-Parametric Learning to Aid Path Planning over Slopes, *The International Journal of Robotics Research*, Vol.29, No.8, pp.997–1018, 2010.

[12] G. Ishigami, K. Nagatani, and K. Yoshida, Trafficability Analysis for Lunar/Planetary Exploration Rover using Thrust-Cornering Characteristic Diagram, *Proceedings of the 2008 IEEE/RSJ International Conference on Intelligent Robot and Systems*, pp.2228–2233, September, 2008.

[13] R. Krenn, A. Gibbesch, G. Binet, and A. Bemporad, Model Predictive Traction and Steering Control of Planetary Rovers, *Proc. of the 12th Symposium on Advanced Space Technologies in Robotics and Automation*, May, 2013.

[14] D. L. de M. Lemus, D. Kohanbash, S. Moreland, and D. Wettergreen, Slope Descent using Plowing to Minimize Slip for Planetary Rovers, *Journal of Field Robotics*, Vol.26, Issue 6, pp.391–410, 2009.

[15] J.J. Biesiadecki, E.T. Baumgartner, R.G. Bonitz, B.K. Cooper, F.R. Hartman, P.C. Leger, M.W. Maimone, S. Maxwell, A. Trebi-Ollennu, E. Tunstel, and J.R. Wright, Mars Exploration Rover Surface Operations: Driving Opportunity at Meridiani Planum, *Proceedings of the 2005 IEEE International Conference on Systems, Man and Cybernetics*, pp.1823–1830, October, 2005.

[16] M. Maimone, Y. Cheng, and L. Matthies, Two Years of Visual Odometry on the Mars Exploration Rovers, *Journal of Field Robotics*, Vol.24, Issue 3, pp.169-186, 2007.

[17] R. Lindemann and C. Voorhees, Mars Exploration Rover Mobility Assembly Design, Test, and Performance, *Proceedings of the 2005 IEEE International Conference on Systems, Man, and Cybernetics*, pp. 450-455, October, 2005.

[18] J. Cameron, A. Jain, T. Huntsberger, G. Sohl, and R. Mukherjee, Vehicle-Terrain Interaction Modeling and Validation for Planetary Rovers, *JPL Publication* 10-15, 2009.

[19] D. Wettergreen, S. Moreland, K. Skonieczny, D. Jonak, D. Kohanbash, and J. Teza, Design and Field Experimentation of a Prototype Lunar Prospector, *The International Journal of Robotics Research*, Vol.29, No.12, pp.1551–1564.

[20] M. Heverly, J. Matthews, J. Lin, D. Fuller, M. Maimone, J. Biesiadecki, and J. Leichty, Traverse Performance Characterization for the Mars Science Laboratory Rover, *Journal of Field Robotics* Vol.30, Issue 6, pp.835-846, 2013.

[21] T.M. Howard and A. Kelly, Optimal Rough Terrain Trajectory Generation for Wheeled Mobile Robots, *International Journal of Robotics Research*, Vol.26, No.2, pp.141–166.

[22] A. Angelova, L. Matties, D. Helmick, and P. Perona, Learning and Prediction of Slip from Visual Information, *Journal of Field Robotics*, Vol.24, Issue 3, pp.205–231, 2007.

[23] M. Bode, Learning the Forward Predictive Model for an Off-Road Skid-Steer Vehicle, Tech. Report, CMU-RI-TR-07-32, Robotics Institute, Carnegie Mellon University, 2007.

[24] M.G. Bekker, *Introduction to Terrain-Vehicle Systems*, Ann Arbor, MI, USA, University of Michigan Press, 1969.

[25] J.Y. Wong, *Theory of Ground Vehicles*, John Wiley & Sons Inc., 1978.

[26] D. Apostolopoulos, Analytical Configuration of Wheeled Robotic Locomotion, Doctoral Dissertation, Robotics Institute, Carnegie Mellon University, April, 2001.

[27] K. Iagnemma, S. Dubowsky, *Mobile Robots in Rough Terrain: Estimation, Motion Planning, and Control with Application to Planetary Rovers*, Springer, 2004.

[28] G. Ishigami, A. Miwa, K. Nagatani, and K. Yoshida, Terramechanics-based Model for Steering Maneuver of Planetary Exploration Rovers on Loose Soil, *Journal of Field Robotics*, Vol.24, Issue 3, pp.233–250, 2007.

[29] B. Shaäfer, A. Gibbesch, R. Krenn, and B. Rebele, Planetary Rover Mobility Simulation on Soft and Uneven Terrain, *Vehicle System Dynamics*, Vol.48, No.1, pp.149–169, 2010.

[30] F. Zhou, R. E. Arvidson, K. Bennett, B. Trease, R. Lindemann, P. Bellutta, K. Iagnemma, and C. Senatore, Simulations of Mars Rover Traverses, *Journal of Field Robotics*, Vol.31, Issue 1, pp.141–160, 2014.

[31] G. Ishigami, K. Nagatani, and K. Yoshida, Path Planning and Evaluation for Planetary Rovers based on Dynamic Mobility Index, *Proceedings of the 2011 IEEE/RSJ International Conference on Intelligent Robots and Systems*, pp.601–606, September, 2011.

[32] J.Y. Wong and A.R. Reece, Prediction of Rigid Wheel Performance based on the Analysis of Soil-Wheel Stress, Part *I*, *Journal of Terramechanics*, Vol.4, No.1, pp.81–98, 1967.

[33] K. Terzaghi, *Theoretical Soil Mechanics*, John Wiley & Sons Inc., 1943.

[34] A.R. Reece, Principles of Soil-Vehicle Mechanics, *Proceedings of the Institution of Mechanical Engineers*, Vol.180, part 2A, No.2, pp.45–66, 1965-1966.

[35] Z. Janosi and B. Hanamoto, The Analytical Determination of Drawbar Pull as a Function of Slip for Tracked Vehicles in Deformable Soils, *Proceedings of the 1st International Society for Terrain-Vehicle Systems Conference*, 1961.

[36] J.Y. Wong and C.F. Chiang, A General Theory for Skid Steering of Tracked Vehicles on Firm Ground, *Proceedings of the Institution of Mechanical Engineers*, Vol.215, part D, pp.343–355, 2001.

[37] G. Meirion-Griffith, C. Nie, and M. Spenko, Development and Experimental Validation of an Improved Pressure-Sinkage Model for Small-Wheeled Vehicles on Dilative, Deformable Terrain, *Journal of Terramechanics*, Vol.51, 2014, pp.19-29.

[38] L. Ding, H. Gao, Z. Deng, Y. Li, and G. Liu, New Perspective on Characterizing Pressure-Sinkage Relationship of Terrains for Estimating Interaction Mechanics, *Journal of Terramechanics*, Vol.52, 2014, pp.57-76.

[39] C. Senatore and K. Iagnemma, Analysis of Stress Distributions under Lightweight Wheeled Vehicles, *Journal of Terramechanics*, Vol.51, 2014, pp.1-17.

[40] D.R. Freitag, A.J. Green, K.J. Melzer, and N.C. Costes, Wheels for Lunar Vehicles, *Journal of Terramechanics*, Vol.8, No.3, pp.89–105, 1972.

[41] S. Wakabayashi, H. Sato, and S. Nishida, Design and Mobility Evaluation of Tracked Lunar Vehicle, *Journal of Terramechanics*, Vol.46, pp.105–114, 2009.

[42] D.F. Flippo and D.P. Miller, Turning Efficiency Prediction for Skid Steering via Single

Wheel Testing, *Journal of Terramechanics*, Vol.52, pp.23–29, 2014.

[43] H. Oravec, V. Asnani, and X. Zeng, Design and Characterization of GRC-1: A Soil for Lunar Terramechanics Testing in Earth-ambient Conditions, *Journal of Terramechanics*, Vol.47, 2010, pp.361–377.

[44] GOM Optical Measuring Techniques, *Pontos Software*, URL: http://www.gom.com/3d-software/pontos-software.html, Accessed July 25, 2015.

[45] H. Inotsume, S. Masataku, K. Nagaoka, K. Nagatani, and K. Yoshida, Modeling, Analysis, and Control of an Actively Reconfigurable Planetary Rover for Traversing Slopes Covered with Loose Soil, *Journal of Field Robotics*, Vol.30, Issue 6, pp.875–896, 2013.

[46] S.M. LaValle, *Planning Algorithm*, Cambridge University Press, 2006.

[47] G. Ishigami, M. Otsuki, and T. Kubota, Range-dependent Terrain Mapping and Multipath Planning using Cylindrical Coordinates for Planetary Exploration Rover, *Journal of Field Robotics*, Vol.30, Issue 4, pp.536–551, 2013.

[48] L. Li, C. Sandu, J. Lee, and B. Liu, Stochastic Modeling of TireSnow Interaction Using a Polynomial Chaos Approach, *Journal of Terramechanics*, Vol.46, pp.165–188, 2009.

[49] G. Ishigami, G. Kewlani, and K. Iagnemma, Predictable Mobility: A Statistical Approach for Planetary Surface Exploration Rovers in Uncertain Terrain, *IEEE Robotics and Autonomous Magazine*, pp.61–70, 2009.

[50] G. Ishigami, K. Nagatani, and K. Yoshida, Slope Traversal Controls for Planetary Exploration Rover on Sandy Terrain, *Journal of Field Robotics*, Vol.26, Issue 3, pp.264–286, 2009.

[51] T. J. Carlone, Investigating Suspension Lift-Off of Skid-Steer Rover with Passive Differential Suspension, *Masters Thesis*, Carnegie Mellon University, December, 2013.

[52] M. Bauer, W. Leung, and T. Barfoot, Experimental and Simulation Results of Wheel-Soil Interaction for Planetary Rovers, *Proceedings of the 2005 IEEE/RSJ International Conference on Intelligent Robots and Systems*, August, 2005.

[53] M. Sutoh, J. Yusa, T. Ito, K. Nagatani, and K. Yoshida, Traveling Performance Evaluation of Planetary Rovers on Loose Soil, *Journal of Field Robotics*, Vol.29, Issue 4, 2012, pp.648–662.

[54] L. Ding, H. Gao, Z. Deng, K. Nagatani, and K. Yoshida, Experimental Study and Analysis on Driving wheel's Performance for Planetary Exploration Rovers Moving in Deformable Soil, *Journal of Terramechanics*, Vol.48, No.1, 2011, pp.27–45.

[55] S. Moreland, K. Skonieczny, H. Inotsum, and D. Wettergreen, Soil Behavior of Wheels with Grousers for Planetary Rovers, *Proceedings of the 2012 IEEE Aerospace Conference*, March, 2012.

[56] K. Skonieczny, S. J. Moreland, and D. S. Wettergreen, A Grouser Spacing Equation for Determining Appropriate Geometry of Planetary Rover Wheels, *Proceedings of the 2012 IEEE/RSJ International Conference on Intelligent Robots and Systems*, October, 2012.

Appendix A

Validity and Limitation of Single-Wheel Representation

This chapter discusses the validity and limitation of the single-wheel representation of a rover for slope-ascent performance analysis. Weight distributions of the two rovers, Andy 2 and Scarab, are first computed based on static analysis. The predicted slip from the single-wheel model are then compared to those based on a full-vehicle model.

A.1 Analysis of weight distribution

A.1.1 Weight distribution model

Based on a static analysis, the weight distributed on each wheel of a four-wheeled rover can be estimated from the geometric configuration of the rover as well as the slope and angle of attack (see Figures A.1 and A.2) as follows:

$$\left.\begin{aligned}
W_{Fl} &= W\tfrac{L_R}{L}\tfrac{D_r}{D}\left(1-\tfrac{H}{L_R}\tan\theta_p\right)\left(1-\tfrac{H}{D_r}\tan\theta_r\right)\\
W_{Fr} &= W\tfrac{L_R}{L}\tfrac{D_l}{D}\left(1-\tfrac{H}{L_R}\tan\theta_p\right)\left(1+\tfrac{H}{D_l}\tan\theta_r\right)\\
W_{Rl} &= W\tfrac{L_F}{L}\tfrac{D_r}{D}\left(1+\tfrac{H}{L_F}\tan\theta_p\right)\left(1-\tfrac{H}{D_r}\tan\theta_r\right)\\
W_{Rr} &= W\tfrac{L_F}{L}\tfrac{D_l}{D}\left(1+\tfrac{H}{L_F}\tan\theta_p\right)\left(1+\tfrac{H}{D_l}\tan\theta_r\right)
\end{aligned}\right\} \tag{A.1}$$

where the subscripts F and R represent front and rear wheels, respectively, whereas l and r represent left and right wheels, respectively. W is the total weight of the rover. θ_p and θ_r denote the pitch and roll angles of the rover, respectively, and are determined from the slope angle θ_0 and angle of attack α as in Eqs. (2.4) and (2.5). L_i denotes the longitudinal distance from the planner CG location to the wheel i while D_i denotes the lateral distance from the CG to the wheel. $L = L_F + L_R$ and $D = D_l + D_r$ are the wheelbase and track width, respectively. H is the height of the CG with respect to the ground.

Note that it is assumed here that the weight redistribution by differential suspensions is negligible in the case of simple linear motions on a slope of a flat surface, which is the target of

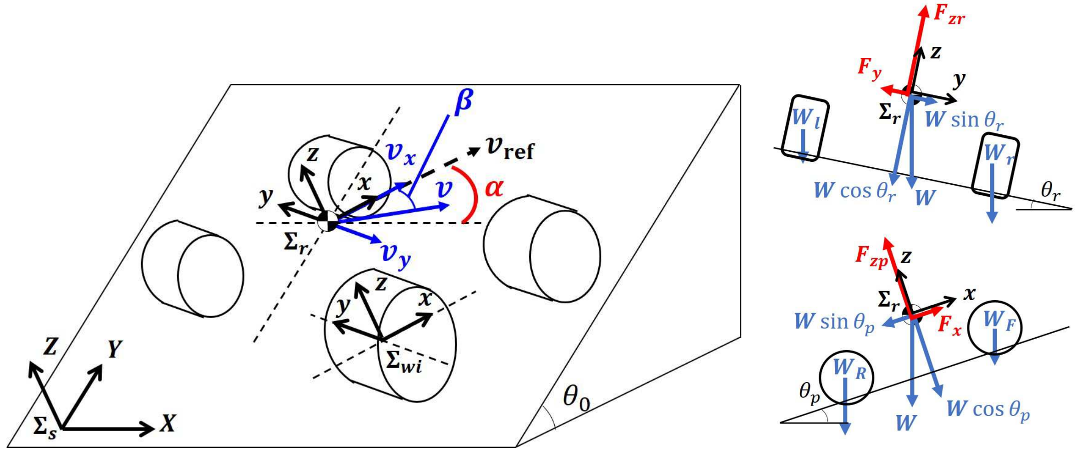

Figure A.1: Steady state slope-ascent by a four-wheeled rover. The rover is ascending a slope of angle θ_0 at an angle of attack α.

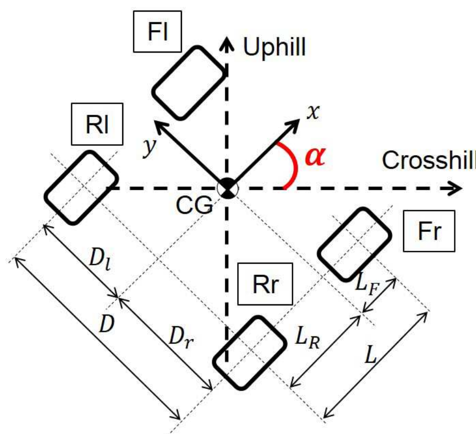

Figure A.2: Schematic view of a planar CG position of a rover projected onto the slope surface.

this thesis. This assumption is violated when a rover traverses highly rough terrain and when skid-steering with differential suspensions is engaged [51]. In these situations, the effects of the suspension should be explicitly taken into account.

A.1.2 Weight distribution of Andy 2 and Scarab

The weight distribution of Andy 2 and Scarab rovers are estimated from the above mentioned model. The dimensions and CG locations of these rovers are listed in Table A.1. Despite there exist large differences in mass and size between the two rovers, their aspect ratio (the ratio of the track width to the wheelbase) and the CG height ratios (the CG height normalized to the wheelbase or track width) are very similar.

Figure A.3 shows the variation of the weight on each wheel of Andy 2 on slopes of 10^o, 20^o, and 30^o with various angles of attack. Here the angle of attack of a rover increases positively in counterclockwise; the angle is 0^o when the front and rear left wheels are located uphill and right

Table A.1: Dimensions of Andy 2 and Scarab rovers with the configurations in the analysis. CG X and Y locations indicate the planar position of the CG in the longitudinal and lateral directions, respectively, with respect to the geometrical center of the rover.

	Andy 2	Scarab
Mass	25 kg	400 kg
Track width D	80 cm	140 cm
Wheelbase L	60 cm	120 cm
CG X location	2 cm	4 cm
CG Y location	0.3 cm	0 cm
CG height H	31 cm	64 cm
Aspect ratio D/L	1.33	1.16
CG height ratio H/L	0.52	0.53
CG height ratio H/D	0.39	0.46

wheels are downhill, and 90^o when the front wheels are uphill and rear wheels are positioned downhill.

In the figures, the weights of each wheel normalized to the total rover weight are shown. All of the normalized weights become equal to 0.25 when the rover weight is equally distributed on each wheel.

As easily expected, more weight is assigned on the downhill, right wheels than left wheels at 0^o angle of attack. Weight distribution changes as the rover orientation changes and as the rover heads to uphill. At 90^o, more weight is distributed to rear wheels compared to the front wheels. The gaps of wheel weights gets more significant when the slope becomes steeper. The weight on a downhill wheel becomes more than four times larger than that of an uphill wheel in the case of 30^o slope.

The weight distribution of Scarab rover with the tested configuration is also shown in Figure A.3. The weight distribution of Scarab on slopes does not significantly differ from that of Andy 2. This is because the similarities in the aspect ratio and the CG height ratio of the two rovers.

A.2 Comparison of single-wheel and full-vehicle slip models

Here the slip predicted based on the single-wheel model used in this thesis is compared with those from a full-vehicle model which takes into account the weight distribution of a rover.

A.2.1 Single-wheel and full-vehicle models

In the single-wheel model, as mentioned in Chapter 2, a rover is represented by a single-wheel with the weight of $W/4$ where W here denotes the total weight of the rover. The slip ratio and slip angle at a steady state of the rover are iteratively predicted such that the following steady

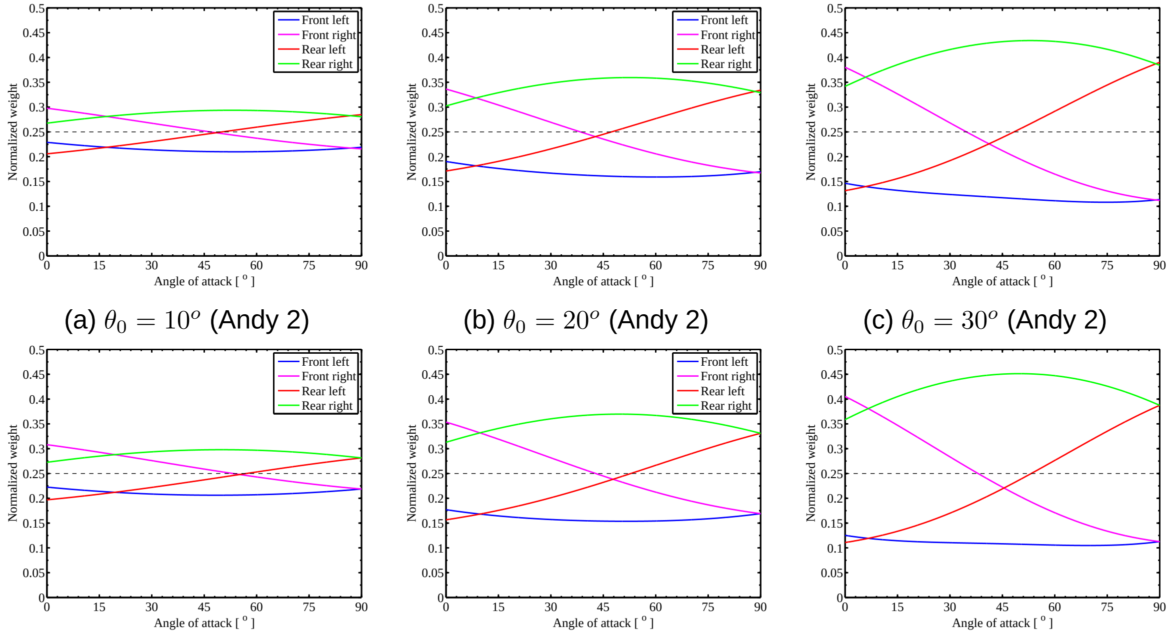

(a) $\theta_0 = 10^o$ (Andy 2) (b) $\theta_0 = 20^o$ (Andy 2) (c) $\theta_0 = 30^o$ (Andy 2)

(d) $\theta_0 = 10^o$ (Scarab) (e) $\theta_0 = 20^o$ (Scarab) (f) $\theta_0 = 30^o$ (Scarab)

Figure A.3: Weight distribution of Andy 2 and Scarab on slopes with varied angles of attack. The vertical axis represents the ratio of the weight on each wheel to the total rover weight.

state conditions on slope are satisfied:

$$\left.\begin{aligned} F_x &= \frac{W}{4}\sin\theta_p \\ F_y &= \frac{W}{4}\sin\theta_r \\ F_z &= \frac{W}{4}\cos\theta_0 \end{aligned}\right\} \tag{A.2}$$

where F_x, F_y, and F_z are the drawbar pull, lateral force, and vertical force respectively, acting on the single-wheel which represents the rover motion.

On the other hand, in the full-vehicle model, the longitudinal and lateral slip at the rover CG are predicted so that the following force balances are met:

$$\left.\begin{aligned} \Sigma F_{xi} &= W\sin\theta_p \\ \Sigma F_{yi} &= W\sin\theta_r \\ F_{zi} &= W_i\cos\theta_0 \end{aligned}\right\} \tag{A.3}$$

where the subscript i represents the wheel ID ($i = Fl, Fr, Rl, Rr$), and W_i denotes the weight distributed on the wheel i which is provided in Eq. (A.1). In this model, instead of balancing the drawbar pull F_{xi} and lateral force F_{yi} of each wheel with those of longitudinal and lateral gravitational resistances, $W_i \sin\theta_p$ and $W_i \sin\theta_r$, respectively, slip is predicted to make the sum of each wheel–soil interaction forces equal to the total gravity resistances at the rover CG. This somewhat takes into consideration the effect of interlocked wheels which is ignored in the single-wheel modeling fashion. Note that this full-vehicle model is more realistic than the single-wheel model; however it is still a simplified, quasi-static representation that does not take into account any dynamic effects of vehicle motions, and assumes any significant orientation change of the rover is not induced over time.

A.2.2 Simulation results

The slip ratio and slip angle of Andy 2 and Scarab rovers were predicted based on the single-wheel and full-vehicle models in a similar way to Section 2.3.1. The comparisons of these predictions are shown in Figure A.4 for Andy 2 and in Figure A.5 for Scarab. As seen in the figures, the slip predicted from the single-wheel model is comparable to those from the full-vehicle model especially for shallower slopes. Gaps between the two becomes larger on steeper slopes, but still the qualitative trends are the same. In addition, the predicted slip based on the single-wheel model tends to be larger than those from the full-vehicle model, meaning the single-wheel model predictions lie on the safe side.

The both models provide similar prediction results despite of the weight distribution on slopes. This is because the more loaded downhill wheels sink more and generate higher pull force and lateral force that compensate the lower tractions generated at the uphill wheels to overcome the gravity resistance as a whole. Figure A.6 shows how interaction forces and sinkage of each wheel change along with the change in the angle of attack. The forces and sinkage in the single-wheel model are also plotted in the figure. The single-wheel representation can be considered as a model with one single wheel of the average wheel weight and approximately average wheel–soil interaction forces. The predicted curves in Figures A.4 and A.5 does not perfectly match since the wheel–soil interaction forces are non-linear functions of the wheel weight.

A.3 Validity and limitation of the single-wheel model

As shown in the previous section, the single-wheel model can provide slip predictions very similar to those from the full-vehicle model for the slope-ascent scenario considered in this thesis. As the full-vehicle model is more computationally expensive than single-wheel model and as a wide range of slopes and angles of attack are required to explore, this research utilized the single-wheel model for the analysis.

However, the single-wheel model is not always valid. It was developed for the simple linear motion and for steady state analysis. The model is not applicable to more complicated scenarios such as rough terrain traverse and steering maneuver where rover orientation can dramatically change. For such cases, dynamics-based simulation is required to predict vehicle behaviors.

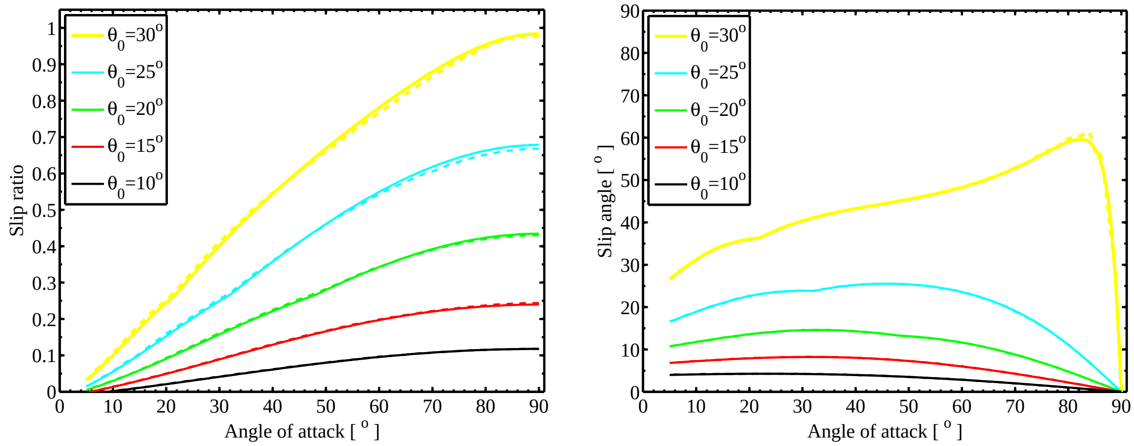

(a) Slip ratio (b) Slip angle

Figure A.4: Comparisons of slip of Andy2 predicted based on the single-wheel model and the full-vehicle model. The solid and dashed curves represent the single-wheel and full-vehicle models, respectively.

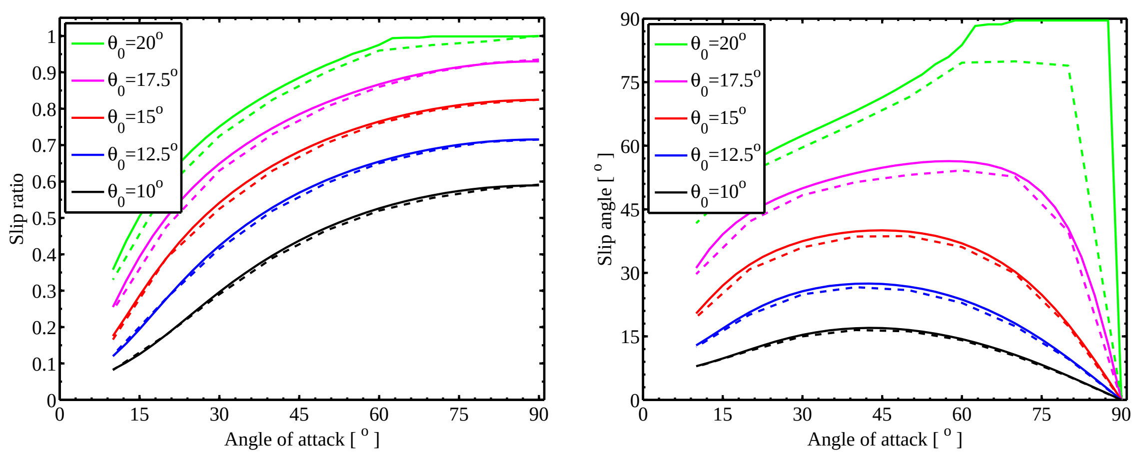

(a) Slip ratio (b) Slip angle

Figure A.5: Comparisons of slip of Scarab predicted based on the single-wheel model and the full-vehicle model. The solid and dashed curves represent the single-wheel and full-vehicle models, respectively.

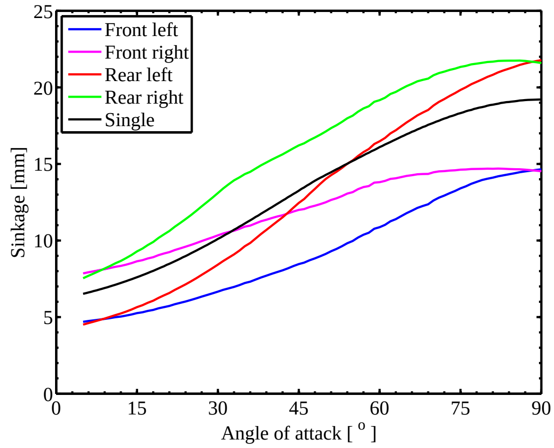

(a) Sinkage

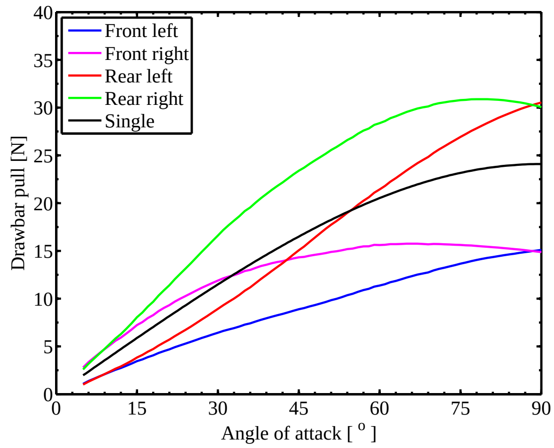

(b) Drawbar pull

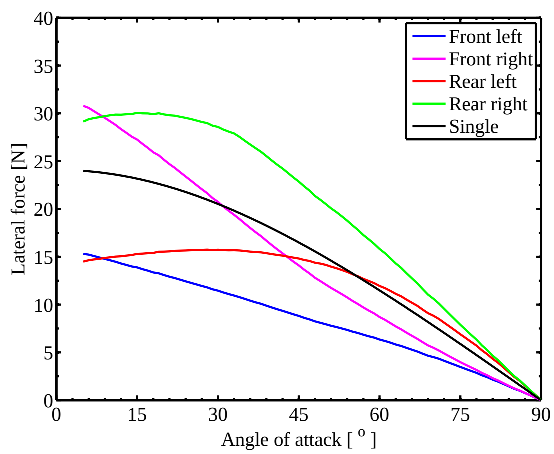

(c) Lateral force

Figure A.6: Predicted sinkage and forces of Andy 2 wheels for varied angle of attack. 20^o slope case is shown. The wheels on the downhill side sink more and generate larger forces that compensate for the lower forces on the uphill wheels. The sinkage and forces in the single-wheel model are also plotted as references.

Appendix B

Parametric Analysis of Wheel Grouser Configuration for Slope-Ascent and Traverse

Considerable research has been conducted, thus far, to study wheel designs to improve vehicles' traversing performance on granular materials, and it has been widely acknowledged that the wheel surface profiles, i.e. grousers/lugs/creates/, have an important role to improve the tractive capability of a wheel. Bauer et al., for example, reported that the increase of the grouser count makes improvement of traction [52]. Sutoh et al. also studied the influence of the number of grousers and found that the improvement of the longitudinal travel performance by the increase of the grouser count has a limitation when the spacing between grousers becomes small [53]. Ding et al. studied the grouser performance on loose soil with various grouser configurations, and reported that the height of grousers also largely influences the drawbar pull of wheels in addition to grouser count [54]. However, most research on grousers has been limited to simple longitudinal linear motions of wheel/rovers. Actual rover operations also involve lateral motions, including steering maneuver and traverse of cross slopes, causing sideslip as discussed in this thesis. No extensive study in lateral performance of grousers has been reported to the best of the author's knowledge.

The influences of wheel grouser count and height on rover performance are assessed in this chapter based on single-wheel sideslip experiments and full-rover slope-ascent/traverse experiments. In the single-wheel experiments, the tractive performance of grousered wheels is evaluated on a single-wheel test rig with various grouser configurations and with various longitudinal and lateral slip conditions. The results of the full-rover experiments are introduced to support the validity of the single-wheel sideslip experiments on leveled soil for assessing rover mobility on slopes. The full-rover experiments described in this chapter were conducted by the author at the Space Robotics Laboratory of Tohoku University in August 2012 prior to joining CMU. The results of the testing were not published.

(a) $\beta = 15^o$ (b) $\beta = 30^o$

Figure B.1: Test wheel with sideslip configurations.

B.1 Single-wheel sideslip experiments

A set of single-wheel experiments were conducted by the author at the Field Robotics Center of Carnegie Mellon University.

B.1.1 Experiment setup and procedures

The single-wheel test rig and the same sand material described in Section 2.2.2 were used in this experimentation.

A wheel with radius of 114 mm and width of 114 mm was utilized. For assessing the influence of grouser count, 0, 12, 24, or 36 grousers of 9.6 mm height were set on the wheel. On the other hand, 24 grousers with the height of 6.3 mm, 9.6 mm, and 12.7 mm were used to assess the influence of grouser height. The mass of the wheel was fixed to 10 kg for each condition.

The orientation, or slip angle, of the wheel was changed from 0^o to 30^o with an interval of 7.5^o to make a forced sideslip motion as shown in Figure B.1. For each slip angle condition, the wheel slip ratio was set to 0, 0.2, 0.4, or 0.6. During the tests, the wheel was controlled to rotate with constant tangential velocity of 10 mm/s while the speed of the carriage was controlled depending on the desired slip ratios and slip angles. Tests were conducted twice for each test condition.

B.1.2 Experiment results

Relationship between wheel slip and forces

Figure B.2 shows the experimental characteristic of the drawbar pull and lateral force, respectively, for varied slip ratios and slip angles. The markers show the average values of drawbar pull and lateral force, and the error bars corresponds to the one-standard deviations.

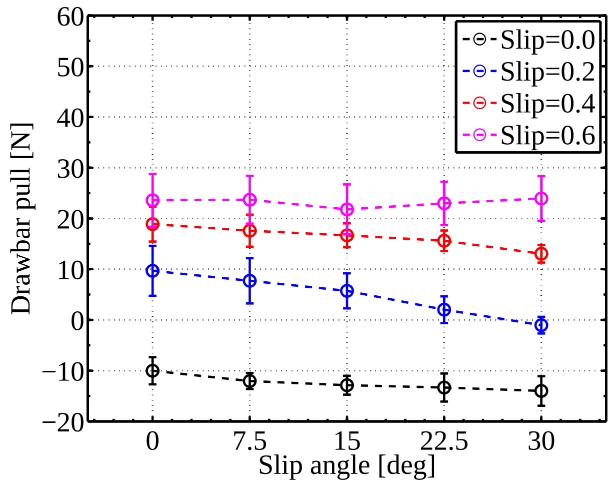

(a) Drawbar pull F_x

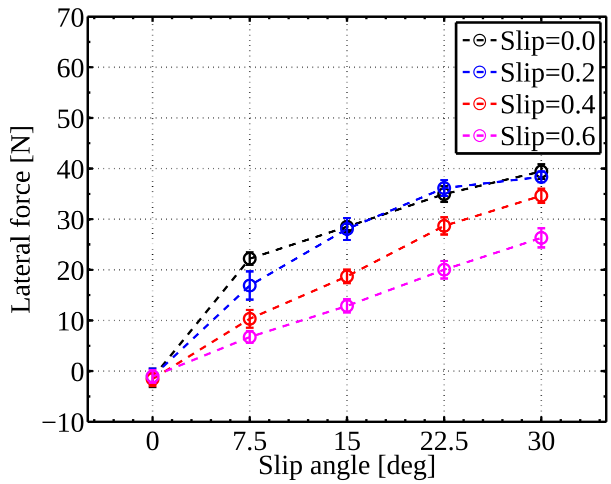

(b) Lateral force F_y

Figure B.2: Relationship between the wheel slip and wheel-soil interaction forces.

The drawbar pull F_x basically decreases when the slip angle β increases as shown in Figure B.2 (a). The trends of the drawbar pull against varied slip ratio are consistent even if the wheel experienced sideslip. On the other hand, the measured lateral force F_y decreases when the slip ratio s rises, and the force increases with the increase of the slip angle β as shown in Figure B.2 (b).

Influence of grouser count

Examples of the measured drawbar pull for different grouser counts is shown in Figure B.3. As seen in Figure B.3 (a), the drawbar pull increases along with the grouser count at the slip ratio of $s = 0.2$ regardless of the increase of the slip angle. At $s = 0.6$ in Figure B.3 (b), however, no measurable drawbar pull improvement can be observed by the increase of the grouser count. That means the amount of the drawbar pull improvement due to the increase of the grouser count reduces at high slip.

This is related to one of the effect of grousers in loose soil: the reduction of the forward soil flow in front of a wheel. As mentioned in [55], grousers contribute to reduce the forward soil flow and the motion resistance, resulting in the increase of the net traction, or drawbar pull. However, the minimum required number of grousers to reduce the forward soil flow decreases as the slip becomes higher. This is since at higher slip, the wheel rim surface makes less progress from the time when one grouser enters into the soil until the next grouser interacts with the soil surface. Therefore at higher slip, the reduction of the motion resistance in front of the wheel is fully achieved with smaller grouser count, compared to lower slip conditions [56]. That is why the improvement of drawbar pull gets less significant at higher slip.

Figure B.4 shows the lateral force for different grouser counts. When compared to the wheel without grousers, the lateral force is improved by mounting grousers. The difference in lateral force between the grouserless and grousered wheels becomes more significant at higher slip ratio and larger slip angles. One factor by which wheels with grousers reduce the lateral slippage is that a grouser can act as a ”stopper” against the lateral motion. When the rover begins to slide in lateral direction while moving forward, the grousers hit the soil at an angle. As a result, the grousers obtain resistance force in the lateral direction in a similar fashion to the longitudinal direction. Therefore, the wheels can obtain larger side force with less slip angle.

However, the increase of the lateral force is only slight even if the grouser count is increased from 12 to 24 or 36.

Influence of grouser height

The results of the sideslip tests for different grouser heights are shown in Figure B.5 and Figure B.6. Unlike the case of the grouser count, both drawbar pull and lateral force are improved by increasing the grouser height regardless of the level of the slip ratio as seen in these figures. One major reason for this is that the taller grousers can interact with deeper and stronger portion of the soil, and they can obtain higher thrust force than shorter grousers. Similarly, taller grousers can obtain higher lateral force, or lateral grip, against sideslip by interacting with stronger part of the soil.

Based on these observations, it can be said that mounting taller grousers can result in better slope-ascent and slope-traverse performances than increasing the grouser count once a wheel has a sufficient number of grousers.

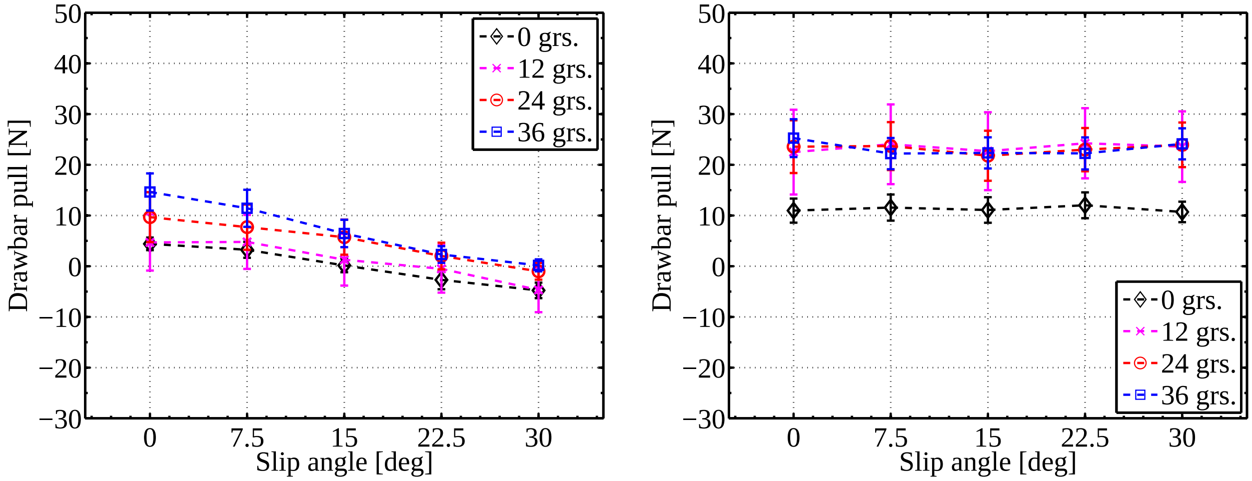

(a) Slip ratio $s = 0.2$ (b) Slip ratio $s = 0.6$

Figure B.3: Influence of grouser count on drawbar pull during sideslip.

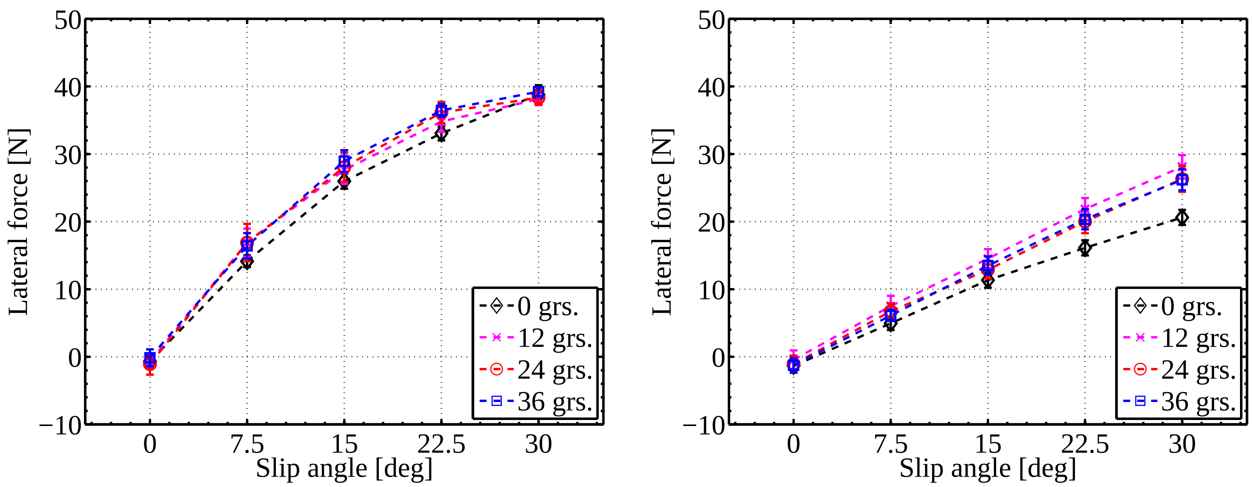

(a) Slip ratio $s = 0.2$ (b) Slip ratio $s = 0.6$

Figure B.4: Influence of grouser count on lateral force during sideslip.

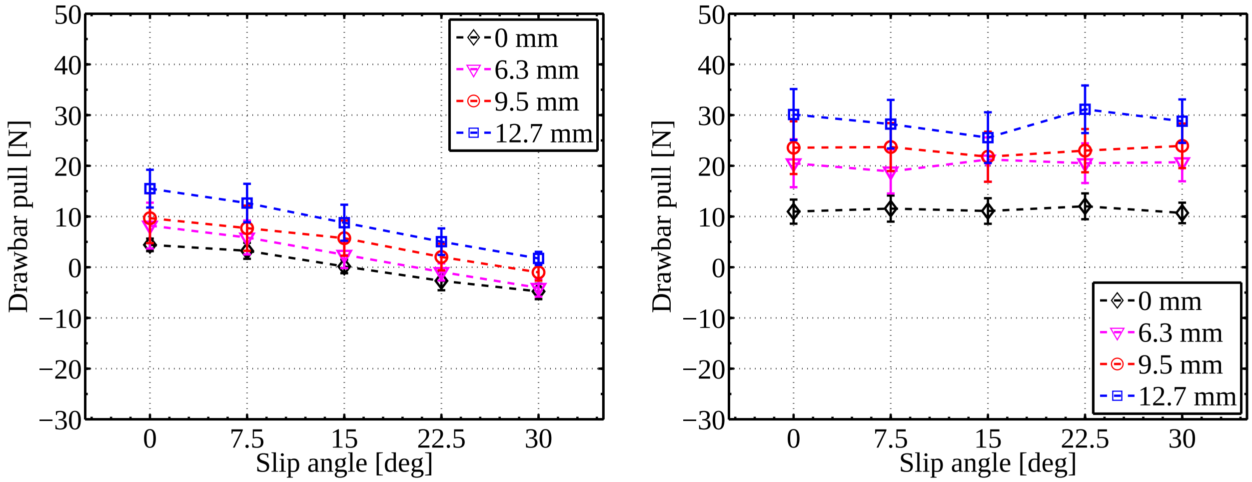

(a) Slip ratio $s = 0.2$ (b) Slip ratio $s = 0.6$

Figure B.5: Influence of grouser height on drawbar pull during sideslip.

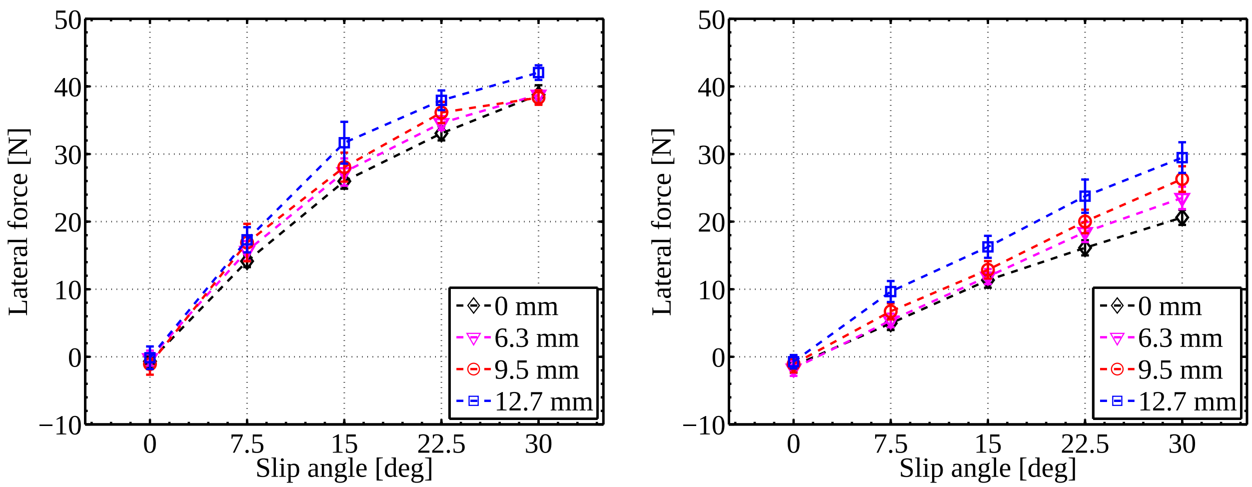

(a) Slip ratio $s = 0.2$ (b) Slip ratio $s = 0.6$

Figure B.6: Influence of grouser height on lateral force during sideslip.

B.2 Slope-ascent and traverse experiments

The influences of the grouser configuration observed in the single-wheel experiments are further discussed based on the experiment using a full rover. Slope-ascent and slope-traverse experiments were conducted by the author at the Tohoku University Space Robotics Laboratory. The outline and results of the experiment campaign are briefly described in this section.

B.2.1 Experiment setup and procedures

Figure B.7 shows the test rover, El-Dorado-Ⅱ, and the test field used in the experiments. The rover has four independently driving wheels and each wheel has a rotary encoder. It is also equipped with a steering motor on each wheel, but the steer motors were not activated and the steer angles of the wheels were fixed during the experiments. Specifications of the rover test bed are listed in Table B.1.

In addition, grousers can be attached to and removed from the surface of each wheel so that the configuration of grousers can be changed. In the experiments, different grouser configurations were used to assess the influence of grouser count and height. Figure B.8 shows the wheels used for the grouser count evaluation. The grouser count was varied from 0 to 12 and 24 while the height of the grousers was fixed to 15 mm. For the evaluation of the grouser height, the wheels shown in Figure B.9 were utilized. In this set of experiments, the grouser count was set to 24, and the grouser height was set to 0 (without grousers), 5, or 15 mm.

A sandbox of 2 m in length and 1 m in width was used. It can be jacked up manually for an inclination of up to approximately 20^o. The box was filled with Toyoura Standard Sand (dry sand). Toyoura sand is cohesionless and less compressible than natural sand which makes experiments highly repeatable.

The rover was commanded to travel directory uphill in the slope-ascent experiments (Figure B.7 (a)) or travel laterally on slopes in the slope-traversing experiments (Figure B.7 (b)). In the slope-ascent testing, the slope angle α was varied from 0^o to 16^o. On the other hand, the angle was set to 15^o in the slope-traverse tests.

The angular velocity of each wheel was set to $\omega = 1.8$ rpm. During the both experiments, the motion of the test bed was captured by using a motion capture camera. Slip ratio s and slip angle β were then calculated using the motion data and the angular velocities of each wheel obtained from the rotary encoder inside the wheel. Before conducting each experiment, the soil was loosen and uniquely leveled. Experiments were conducted three times at each condition.

Table B.1: Specifications of the rover testbed, El-Dorado-Ⅱ (nominal configuration)

Size [mm]	L800 $\times$ W650 $\times$ H750
Mass [kg]	35
Wheel size [mm]	ϕ178 $\times$ W100
Tread [mm]	550
Wheel base [mm]	600

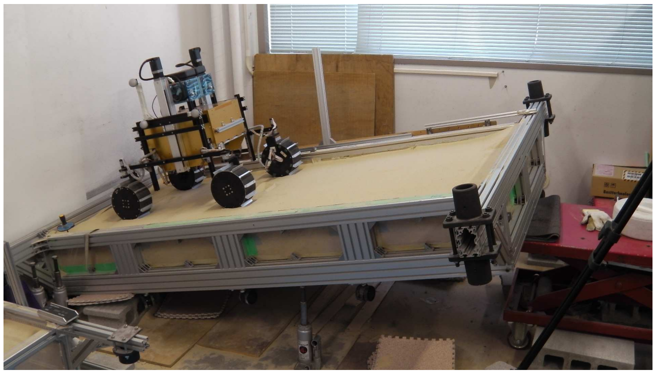

(a) Slope-ascent test

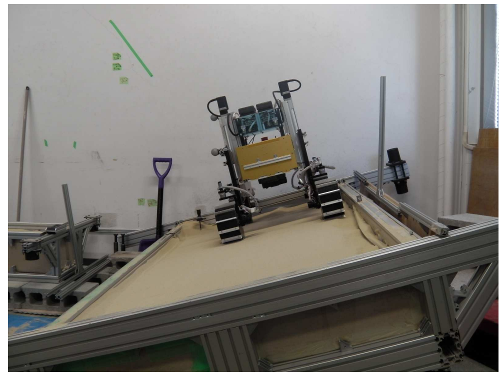

(b) Slope-traverse test

Figure B.7: Test rover and test field.

(a) No grouser

(b) 12 grousers

(c) 24 grousers

Figure B.8: Wheels used to evaluate the effect of grouser count.

(a) No grouser

(b) 5 mm grousers

(c) 15 mm grousers

Figure B.9: Wheels used to evaluate the effect of grouser height.

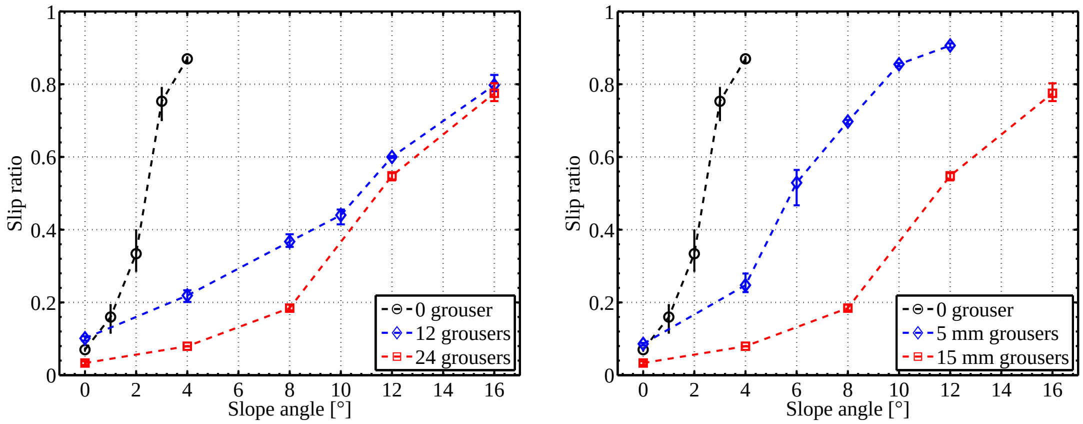

(a) Influence of grouser count on slip

(b) Influence of grouser height on slip

Figure B.10: Slope-ascent experiment results.

B.2.2 Slope-ascent experiment results

The results of the slope-ascent experiments are summarized in Figure B.10. In the figure, the measured rover slip is plotted against slope angle.

The influence of the grouser count on slope-ascent capability is shown in Figure B.10 (a). When the rover does not have any grousers on the wheels, the slip became close to 0.9, meaning that the rover did not make almost no progress, on just 4^o slope. When 12 grousers were installed, the slip on the same slope was drastically reduced to around 0.2. Additional increase of the grouser count from 12 to 24 resulted in more reduction of the slip on the same 4^o slope, and showed lower slip ratio on steeper slopes. However, the reduction of the slip on slopes steeper than 10^o was not as significant as that on shallower slopes.

Figure B.10 (b) indicates the effect of the grouser height on slope-ascent performance of the rover. Similar to increasing grouser count, the slip ratio reduced when taller grousers were used. However, unlike the grouser count case, the increasing the grouser height showed high reduction of the slip even on 12^o slope. These results indicate the importance of the grouser height to improve the tractive capability of a rover.

B.2.3 Slope-traverse experiment results

Figure B.11 shows the typical traveling trajectories measured in the slope-traversing experiments. As shown in Figure B.11 (a), the rover with more grouser count could travel with less deviation from desired straight path. The influence of the grouser height on the lateral traveling performance as seen in Figure B.11 (b) also indicates the similar tendencies to that of the grouser count.

The average slip angle and slip ratio during the experiments are showed in Figure B.12 and B.13, respectively, as the relationships with the grouse count and height. As seen in the Figs B.12 (a) and B.13 (a), the slip ratio and slip angle greatly reduced by mounting 12 grousers on the wheel. However, the reductions of both the longitudinal and lateral slip are less significant

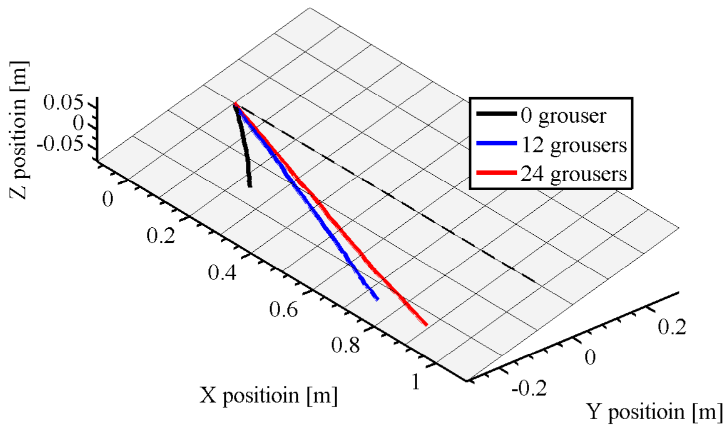

(a) Trajectories of different grouser counts

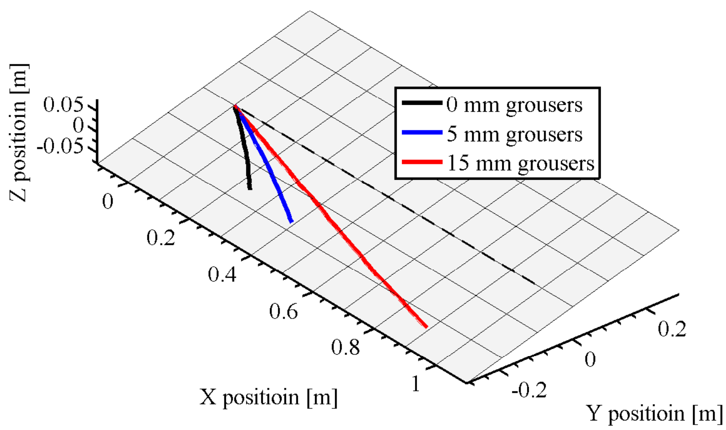

(b) Trajectories of different grouser heights

Figure B.11: Rover trajectories with different grouser configurations.

when the grouser count is increased from 12 to 24. On the other hand, when the grouser height is increased, both the slip ratio and slip angle clearly reduced as shown in the Figs B.12 (b) and B.13 (b).

These results show the same tendencies seen in the single-wheel experimentation and therefore show the validity of the single-wheel experiments to assess the slope-traverse performance of rovers.

B.3 Assessment of grouser design for slope-ascent and traverse

From the above discussions, the following conclusions can be made:

1. Grousers can reduce both the longitudinal and lateral slip.

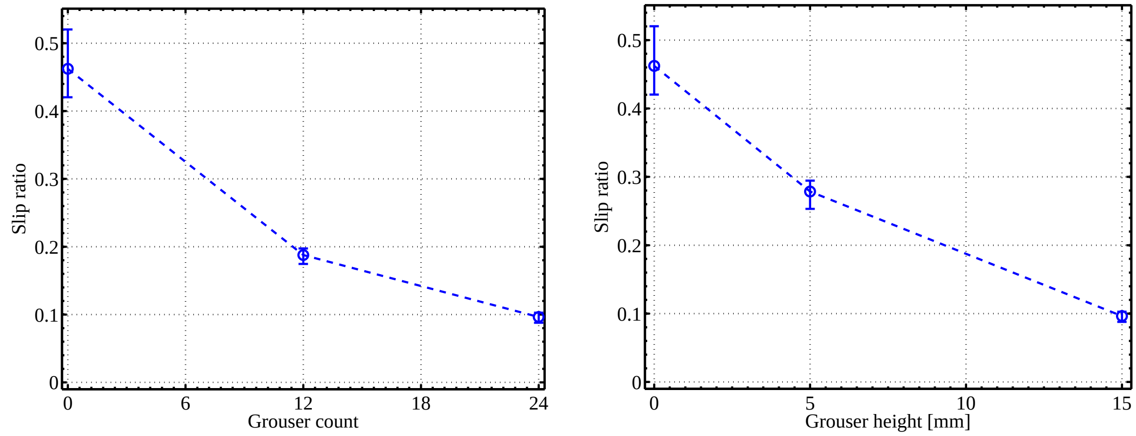

(a) Slip ratio vs grouser count

(b) Slip ratio vs grouser height

Figure B.12: Slip ratio during slope-traversing for different grouser configurations.

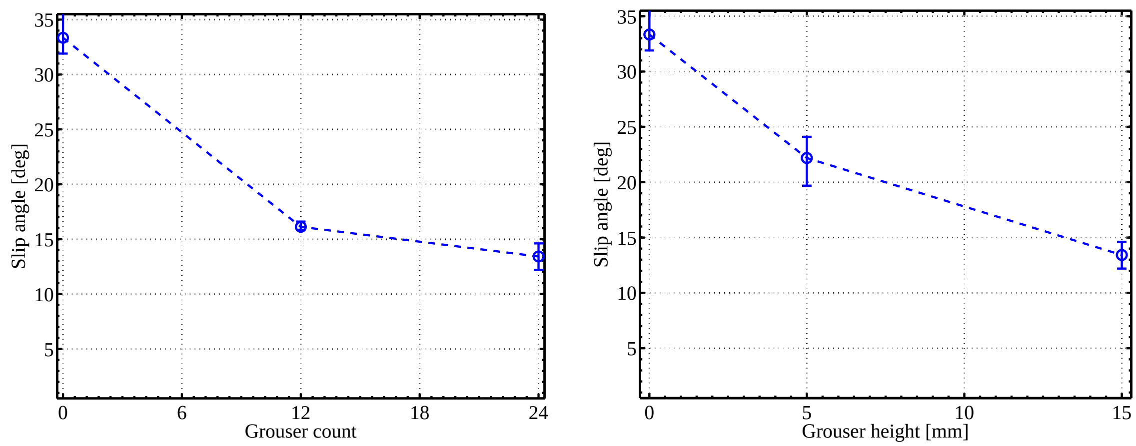

(a) Slip angle vs grouser count

(b) Slip angle vs grouser height

Figure B.13: Slip angle during slope-traversing for different grouser configurations.

2. Grouser count does not have significant influence once sufficient number of grousers are mounted.
3. Grouser height does have more influence on tractive performance than grouser count.

Therefore, tall grousers with sufficient grouser count is preferable to reduce both the longitudinal and lateral slip, and to improve the slope-ascent/traverse capability of a rover. However, the interaction between the grousers and the soil is quite complicated and the effects of grousers have not been reasonably modeled in terramechanics even for longitudinal linear motions. Further study on the grouser–soil interaction is needed to develop a comprehensive wheel design guideline for improving rover mobility on unconsolidated terrain.